JOURNAL OF THE AERONAUTICAL SCIENCES

VOLUME 16 OCTOBER, 1949 NUMBER 10

A Solution for the Lift and Drag of Airfoils with Air Inlets and Suction Slots

C. B. SMITH*

United Aircraft Corporation

SUMMARY

The general airfoil theory is extended to cover the case of airfoils having air inlets and suction slots. The analysis, employing formal potential theory, rests on the usual assumptions of an incompressible, nonviscous fluid satisfying the Kutta condition. Subject to these assumptions, it is found that the lift and drag of such an airfoil are given by

$$C_L = 2\pi(\alpha + \epsilon) + 2\sum_n C_{Q_n} \tan\left(\frac{\beta_n - \epsilon}{2}\right)$$

$$C_D = 2\sum_n C_{Q_n}$$

where the symbols are defined on Fig. 6.

These results have been confirmed by simple tests, the results of which are summarized in Fig. 8.

In general, it is indicated that an air inlet or suction slot on the upper surface, $+\beta$, increases the lift or, on the lower surface, $-\beta$, decreases the lift in a manner analogous to changing the camber of the airfoil. An air inlet near the nose, $\beta = 0$, is indicated to have no effect on the lift, while a suction slot on the upper surface, or the equivalent of a source on the lower surface near the trailing edge, is indicated to give large lift increments. The latter arrangements are considered to be of possible interest as a control or high lift device. All of these effects are hydrodynamic and independent of the effect of the inlet or slot on the boundary layer.

NOTATION

x, y, z = Cartesian coordinates
U_0 = free-stream velocity
u = component of velocity along x-axis
v = component of velocity along y-axis
w = component of velocity along z-axis
s = general displacement $s = \sqrt{x^2 + y^2 + z^2}$
q = general velocity $q = \sqrt{u^2 + v^2 + w^2}$
r, θ = polar coordinates (see Fig. 3)
R = radius of cylinder
c = chord of airfoil
β = polar angle of source-sink discontinuity (see Fig. 1)
ϵ = $\epsilon + \pi$ = polar angle of point transforming into trailing edge of airfoil
α = angle of attack
ϕ = velocity volential
ψ = stream function
Γ = circulation
z = complex coordinate (see Fig. 1)
z_0 = complex coordinate of poles of Eq. (10)
w = potential function
ζ = complex coordinate (see Fig. 1)
i = complex operator
li = coordinate of source in z-plane (see Fig. 1)
m = volume flow from source (cu.ft. per ft. per sec.)
C_Q = m/U_0c, flow coefficient (positive for sink)
p = absolute pressure
ρ = density
C_1, C_2 = contours of integration (see Fig. 2)
S_1, S_2, S_3, S_4 = surface of integration (see Fig. 2)
X = net aerodynamic force on airfoil in chordwise direction
Y = net aerodynamic force on airfoil normal to chord line
K_1 = constants defined by Eqs. (10) and (11)

(I) INTRODUCTION

IN 1912 JOUKOWSKY PUBLISHED a treatise[1] presenting for the first time a complete and practical solution

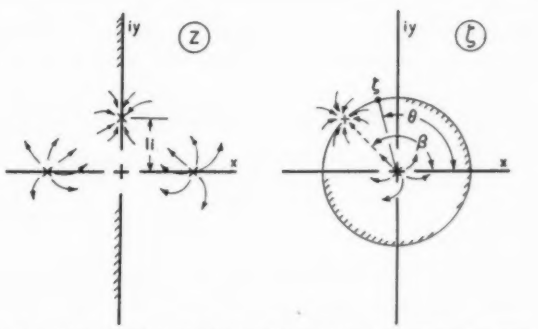

FIG. 1. Flow in ζ-plane obtained from flow in z-plane by conformal transformation defined by Eq. (1).

Received January 30, 1949.

* Aerodynamics Engineer, Analysis Section, Research Department.

for the lift and drag of an airfoil. This work, concluding a long quest for such a solution, was partly based on, and partly done concurrently with, that of Kutta and Lanchester. Although refinements and extensions have since been made (notably by Glauert,[2] Theodorsen,[3] and Allen[4]), the methods and assumptions presented in this original paper constitute the basis of airfoil theory as applied today.

This theory has long served as a rigorous framework around which specific experimental investigations could be organized and which, in recent years, has been successfully used as an analytical tool in the design of high-performance sections.

In the present paper the general theory is extended to cover the case of the airfoil having air inlets and suction slots on its boundary. This solution is obtained by representing the suction slot or air inlet by one or more sink discontinuities. The formal problem herein considered thus consists of solving for the lift and drag of an airfoil having one or more source-sink discontinuities on its boundary.

The reader is referred to references 2 and 5 for the necessary background for the development that follows.

(II) Formal Solution

(A) *Potential Function for Cylinder with Source-Sink Discontinuity on Boundary*

The transformation

$$\zeta = -iR[(z+1)/(z-1)] \tag{1}$$

takes the imaginary axis, iy, in the z-plane into a circle of radius R in the ζ-plane. (See Fig. 1.) In particular, the points $-i$, 0 and $+i$ are transformed into points at R, $+iR$, and $-R$. If, therefore, a simple flow can be built up in the z-plane in which iy is a streamline and in which there is a source-sink discontinuity located on iy, then transforming this flow with Eq. (1) will yield the flow about a cylinder with a source or sink on its boundary.

If a source-sink discontinuity is simply placed on the iy-axis, say at $+li$, iy will be a stream line which will, as desired, become a circular cylinder. However, if a single source or sink is located in the z-plane, a singularity of opposite sign is automatically placed at infinity (continuity requirement). Since the point at infinity in the z-plane transforms into a point *on* the cylinder in the ζ-plane, the transform of a single sink at $+li$ is a cylinder with a sink *and* a source on its boundary. To overcome this difficulty, assuming a sink at li, a source is placed at $+1$, and, in order to preserve iy as a stream line, a second image source is placed at -1. The strength of the sources at -1 and $+1$ are noted as m and that of the sink is, on this basis, $-2m$.* With this arrangement there is no singularity at infinity. Thus, in the ζ-plane, a cylinder is produced with a sink of strength $-2m$ on its boundary, a source at the origin (the transform of $z = -1$), and a source at infinity (transform of $z = +1$).

The potential function of the new flow could be found by substituting the inverse of the transformation function (1) into the potential function of the simple source-sink flow in the z-plane. In this case, however, the new flow is composed of point sources and sinks of known strength and location, and it is simpler to write down the potential function directly. Thus since the potential function of a source (+) or a sink (−) located at the origin and of strength m is

$$w = \pm(m/2\pi)\ln z \tag{2}$$

that of a sink of strength $-2m$ located at $Re^{i\beta}$ is

$$w = -2(m/2\pi)\ln(z - Re^{i\beta})$$

The total potential function for the flow in the ζ-plane is thus

$$w = -2\frac{m}{2\pi}\ln(\zeta - Re^{i\beta}) + \frac{m}{2\pi}\ln\zeta$$

A uniform flow of velocity U_0 from the right may be added by superimposing the potential function for uniform flow about a cylinder.[1] Since the cylinder stream line is common to both flows, this boundary is unaffected by the addition. The total potential function for uniform flow past a cylinder with a sink of strength $-2m$ in its boundary is

$$w = -\frac{m}{2\pi}[2\ln(\zeta - Re^{i\beta}) - \ln\zeta] - U_0\left(\zeta + \frac{R}{\zeta}\right) \tag{3}$$

This can be transformed into the flow about such a cylinder at angle of attack α by the transformation $z' = \zeta e^{i(-\alpha)}$, or the new potential function can be obtained by substituting the inverse, $\zeta = z'^{\,i\alpha}$ into Eq. (3). That is,

* Note, however, that the volume removed from the flow external to the cylinder is simply m.

$$w = -\frac{m}{2\pi}[2\ln(z'^{\,i\alpha} - Re^{i(\beta+\alpha)}) - \ln z'\,e^{i\alpha}] - U_0\left(z'^{\,i\alpha} + \frac{R^2}{z'^{\,i\alpha}}\right) \tag{4}$$

where the α is added to the $Re^{i(\beta+\alpha)}$ term in order to keep the sink at the same point on the cylinder, irrespective of the angle of attack α.

Finally, the effect of a circulation about the cylinder can be included by superimposing the potential function for a point vortex at the origin. Eq. (4) thus becomes

$$w = -\frac{m}{2\pi}\left[2 \ln (ze^{i\alpha} - Re^{i(\beta+\alpha)}) - \ln ze^{i\alpha}\right] - U_0\left(ze^{i\alpha} + \frac{R^2}{ze^{i\alpha}}\right) - i\frac{\Gamma}{2\pi} \ln ze^{i\alpha} \tag{5}$$

where the primes have now been dropped from the z's for simplicity.

Adding more source-sink discontinuities merely adds additional terms of the form of the first of Eq. (5). Therefore, for the general case,

$$w = +\sum_n \left\{-\frac{m_n}{2\pi}\left[2 \ln (ze^{i\alpha} - Re^{i(\beta_n+\alpha)}) - \ln ze^{i\alpha}\right] - U_0\left(ze^{i\alpha} + \frac{R^2}{ze^{i\alpha}}\right) - i\frac{\Gamma}{2\pi} \ln z^{i\alpha}\right\} \tag{6}$$

(B) *Lift and Drag of the Cylinder with One or More Source Sink Discontinuities on Its Boundary*

The pressure forces acting on any body whose surface is a stream line and for which the potential function for the flow is known can be computed directly by application of the Blasius formula,

$$X - iY = (1/2)\rho i \oint_c (dw/dz)^2 dz \tag{7}$$

In the present case, there being one or more source-sink discontinuities on the surface of the body, this boundary is not a stream line and Eq. (7) is not directly applicable. If, however, it be recalled that the sources and sinks are themselves being used to represent slots of finite width and if the momentum balance be written for this actual system, this difficulty can be overcome and a practical significance given to the solution of Eq. (7). Let the system be defined as that bounded by surfaces S_1, S_2, S_3, and S_4 (see Fig. 2), where S_1 is the exposed surface of the body *including the walls of the slot or slots*, S_2 is the exposed bounding surface, and S_3 and S_4 are the side forces of the bounding surface. The x- and y-components of force are then

$$-X - \oint_{c_2} p\, dy; \quad -iY + i\oint_{c_2} p\, dx$$

where X and Y are the pressure forces *on* the body surface S_1 *including those acting on the inside of the slot.* Since S_1 is now a stream line, the ratio of momentum transfers are

$$\oint_{c_2} (\rho u\, dy - u\rho v\, dx)$$

$$i\oint_{c_2} (v\rho u\, dy - v\rho v\, dx)$$

Equating the forces to the rates of momentum change and simplifying, one obtains

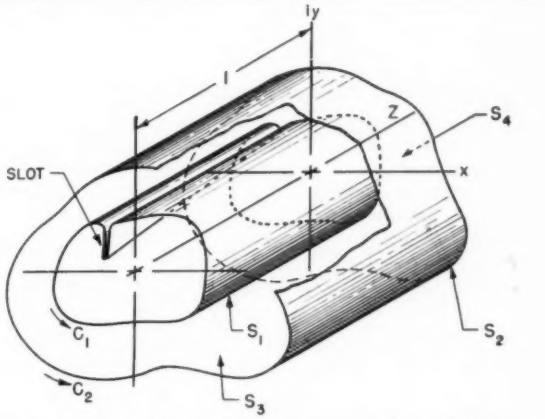

FIG. 2. System used in applying Blasius equation to body having source-sink discontinuity on boundary.

$$X - iY = (1/2)\rho i \oint_{c_2} (dw/dz)^2 dz$$

where X and Y are the pressure forces not only on the exposed surface of the body but also the walls of the slot and w is the potential function for the slot flow. The width of the slot (or slots) may, however, be reduced to the point where the potential function w for the slot flow is, along the boundary C_2, indistinguishable from the potential function (5) for the line sink. Thus Eq. (5) may be substituted into Eq. (7). In general, if a slot is represented by a line sink, the solution of the integral $(1/2)\rho i \oint_{c_2} (dw/dz)^2\, dz$ yields a quantity the real and imaginary parts of which are, respectively, the X- and Y-components of force on the body, including the internal forces required to divert the internal flow parallel to the spanwise axis.

Using the potential function defined by Eq. (5), Eq. (7) is evaluated as follows:

$$\frac{dw}{dz} = -\frac{m}{2\pi}\left(\frac{2}{z - Re^{i\beta}} - \frac{1}{z}\right) - U_0 e^{i\alpha}\left(1 - \frac{R^2}{z^2}\, e^{-2i\alpha}\right) - i\frac{\Gamma}{2\pi}\frac{1}{z} \tag{8}$$

$$\left(\frac{dw}{dz}\right)^2 = \left\{\left[-\frac{m}{2\pi}\left(\frac{2}{z - Re^{i\beta}} - \frac{1}{z}\right) - U_0 e^{i\alpha}\left(1 - \frac{R^2}{z^2}\, e^{-2i\alpha}\right)\right] - i\frac{\Gamma}{2\pi}\frac{1}{z}\right\}^2 \tag{9}$$

Expanding and rearranging,

$$\left(\frac{dw}{dz}\right)^2 = U_0^2e^{2i\alpha} + \left[-2\left(\frac{m}{2\pi}\right)U_0e^{i\alpha} + 2\frac{i\Gamma}{2\pi}U_0e^{i\alpha}\right]\frac{1}{z} + \left[\left(\frac{m}{2\pi}\right)^2 - 2U_0^2e^{2i\alpha}R^2 - 2\frac{i\Gamma}{2\pi}\left(\frac{m}{2\pi}\right) + \frac{i^2\Gamma^2}{4\pi^2}\right]\frac{1}{z^2} +$$

$$\left[2\left(\frac{m}{2\pi}\right)U_0e^{i\alpha}R^2 - 2\frac{i\Gamma}{2\pi}U_0e^{-i\alpha}R^2\right]\frac{1}{z^3} + (U_0^2e^{-2i\alpha}R^4)\frac{1}{z^4} + \left[4\left(\frac{m}{2\pi}\right)U_0e^{i\alpha}\right]\frac{1}{(z - Re^{i\beta})} +$$

$$\left[-4\left(\frac{m}{2\pi}\right) + 4\frac{i\Gamma}{2\pi}\left(\frac{m}{2\pi}\right)\right]\frac{1}{z(z - Re^{i\beta})} + \left[-4\left(\frac{m}{2\pi}\right)U_0e^{-i\alpha}R^2\right]\frac{1}{z^2(z - Re^{i\beta})} + 4\left(\frac{m}{2\pi}\right)^2\frac{1}{(z - Re^{i\beta})^2} \quad (10)$$

The integration of Eq. (10) according to Eq. (7) involves the termwise integration of the following functions of

$$\frac{K_1}{z}, \frac{K_2}{z^2}, \frac{K_3}{z^3}, \frac{K_4}{z^4}, \frac{K_5}{(z - z_0)}, \frac{K_6}{(z - z_0)^2}, \frac{K_7}{z(z - z_0)}, \frac{K_8}{z^2(z - z_0)} \quad (11)$$

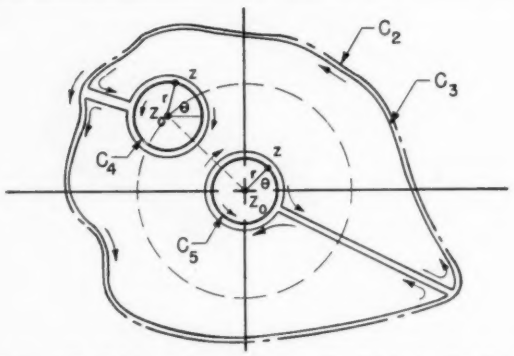

FIG. 3. $\oint_{C_2} f(z)dz = \oint_{C_3} f(z)dz + \oint_{C_4} f(z)dz + \oint_{C_5} f(z)dz$.

It is immediately apparent that all of these terms are of one of two general types

$$K/(z - z_0)^n \quad (12)$$

$$K/z^n(z - z_0) \quad (13)$$

Furthermore, breaking (13) up into rational fractions, one obtains

$$\frac{K}{z^n(z - z_0)} = \frac{K}{z_0^n}\left[\frac{1}{(z - z_0)} - \frac{1}{z} - \frac{z_0}{z^2} - \frac{z_0^2}{z^3} \cdots - \frac{z_0^{n-1}}{z^n}\right] \quad (14)$$

from which it is apparent that (13) is itself composed of a series of terms of the form of (12). Thus, all of the functions of z appearing in Eq. (10) are, or can be, written in the form $K/(z - z_0)^n$.

Eq. (7) requires that these terms be integrated around a path C_2 enclosing poles (divisions by zero) at $z = z_0 = 0$ and $z = z_0 = Re^{i\beta}$. Now the integral of each function around C_2 can be written as the integral around C_3 plus the integrals around C_4 and C_5, where C_4 and C_5 enclose the poles (see Fig. 3). The sum of these line integrals, $C_3 + C_4 + C_5$, equals that around C_2. But path C_3 is indented so as to enclose no poles and, hence, by Cauchy's integral theorem is zero. The integrals of (12) along paths C_4 and C_5 enclosing the poles at 0 and $Re^{i\beta}$ are obtained in each case as follows. Let $z - z_0 = re^{i\theta}$ (see Fig. 3.). Then for $n \neq 1$

$$K\oint\frac{dz}{(z - z_0)^n} = K\oint_0^{2\pi}\frac{re^{i\theta}id\theta}{r^ne^{in\theta}} = K\left[\frac{1}{r^{n-1}}\frac{e^{i(1-n)\theta}}{(1-n)}\right]_0^{2\pi} = 0 \quad (15)$$

and for $n = 1$

$$K\oint\frac{dz}{(z - z_0)} = K\oint_0^{2\pi} id\theta = K2\pi i \quad (16)$$

Thus, by Eq. (15) the integrals of all terms for which $n \neq 1$ around C_4 and C_5 are zero, and by Eq. (16) the integral of all terms for which $n = 1$ is equal to $K2\pi i$ about the path enclosing its pole—i.e., about C_4 or C_5. Since the integral around C_2 equals that around $C_3 + C_4 + C_5$ and since that around C_3 is always zero, it follows that the integral of all terms around C_2 for which $n \neq 1$ is zero—i.e.,

$$\oint_{C_2}[K\,dz/(z - z_0)^n = 0, n \neq 1 \quad (17)$$

and that of those for which $n = 1$ is $K2\pi i$—i.e.,

$$\oint_{C_2}[K\,dz/(z - z_0)] = K2\pi i \quad (18)$$

Substituting Eq. (18) into the integral of Eq. (14), it follows that

$$\oint_{C_3} \frac{K\,dz}{z^n(z-z_0)} = \frac{K}{{z_0}^n}(2\pi i - 2\pi i - 0 - 0 \ldots - 0) = 0, \text{ for } n \geqq 1 \tag{19}$$

Using Eqs. (17), (18), and (19) it follows that the integral around C_2 of all terms of Eq. (10) are zero except the second and sixth. Thus, the integration of Eq. (10) reduces to

$$\oint_{C_2} \left(\frac{dw}{dz}\right)^2 dz = \left[-2\left(\frac{m}{2\pi}\right)U_0e^{i\alpha} + 2\frac{i\Gamma}{2\pi}U_0e^{i\alpha}\right]\oint_{C_2}\frac{dz}{z} + \left[4\left(\frac{m}{2\pi}\right)U_0e^{i\alpha}\right]\oint_{C_2}\frac{dz}{(z-Re^{i\beta})}$$

or

$$\oint_{C_2} \left(\frac{dw}{dz}\right)^2 dz = \left[-2\left(\frac{m}{2\pi}\right)U_0e^{i\alpha} + 2\frac{i\Gamma}{2\pi}U_0e^{i\alpha}\right]2\pi i + \left[4\left(\frac{m}{2\pi}\right)U_0e^{i\alpha}\right]2\pi i = 2mU_0e^{i\alpha}i - 2\Gamma U_0e^{i\alpha}$$

and Eq. (7) reads

$$X - iY = (1/2)\rho i \oint \left(\frac{dw}{dz}\right)^2 dz = (1/2)\rho i(2mU_0e^{i\alpha}i - 2\Gamma U_0e^{i\alpha}) = -\rho mU_0e^{i\alpha} - \rho\Gamma U_0e^{i\alpha}i = -\rho U_0 m \times$$

$$(\cos\alpha + i\sin\alpha) - i\rho\Gamma U_0(\cos\alpha + i\sin\alpha) = (-\rho U_0 m\cos\alpha + \rho\Gamma U_0\sin\alpha) -$$

$$i(\rho U_0 m\sin\alpha + \rho\Gamma U_0\cos\alpha)$$

or

$$\left.\begin{aligned} X &= -\rho U_0 m\cos\alpha + \rho\Gamma U_0\sin\alpha \\ Y &= \rho U_0 m\sin\alpha + \rho\Gamma U_0\cos\alpha \end{aligned}\right\} \tag{20}$$

Eqs. (20) indicate that *for the cylinder the components of force normal and parallel to the free stream direction—i.e., the lift and drag are, respectively,* $\rho U_0\,\Gamma$ *and* $\rho U_0 m$. (See Fig. 4.)

Examining Eq. (8) in retrospect, it is apparent that in squaring dw/dz the only terms that do not produce zero forms are the products with $-U_0e^{i\alpha}$, and in squaring each of these occurs twice. Thus, Eq. (9) could be written

$$\left(\frac{dw}{dz}\right)^2 = -2U_0e^{i\alpha}\left[-\left(\frac{m}{2\pi}\frac{2}{z-Re^{i\beta}} - \frac{1}{z}\right) - i\frac{\Gamma}{2\pi}\frac{1}{z}\right] + (\text{terms which on integration} = \text{zero}) \tag{9a}$$

If now two or more source-sink discontinuities are located on the boundary, the potential function corresponding to Eq. (5) is as noted by Eq. (6). The derivative corresponding to Eq. (8) is

$$\frac{dw}{dz} = \sum_n\left[-\frac{m_n}{2\pi}\left(\frac{2}{z-Re^{i\beta_n}} - \frac{1}{z}\right)\right] - U_0e^{i\alpha}\left(1 - \frac{R^2}{z^2}e^{-2i\alpha}\right) - i\frac{\Gamma}{2\pi}\frac{1}{z} \tag{8a}$$

As in the case of Eq. (9a), the square of Eq. (8a) produces all zero forms except for the products with $-U_0e^{i\alpha}$,* which again each occur twice. Thus,

$$\left(\frac{dw}{dz}\right)^2 = -2U_0e^{i\alpha}\left[\sum_n\left(-\frac{m_n}{2\pi}\frac{2}{z-Re^{i\beta}} - \frac{1}{z}\right) - i\frac{\Gamma}{2\pi}\frac{1}{z}\right] + (\text{terms which on integration} = \text{zero}) \tag{9b}$$

* The only form not previously discussed which develops is in the cross products between the source-sink potential functions. Here one obtains products of the form $\oint [dz/(z-\alpha)(z-\beta)]$ ($\alpha + \beta$ inside c). By breaking this up into rational functions, however, one obtains the difference of two integrals of the form of (12). This form is therefore also zero.

---

which when substituted into Eq. (7) yields

$$X - iY = (1/2)\rho i(2U_0ie^{i\alpha}\sum_n m_n - 2\Gamma U_0e^{i\alpha})$$

or

$$\boxed{\begin{aligned} \text{Lift} &= \rho U_0\Gamma \\ \text{Drag} &= \rho U_0\sum_n m_n \end{aligned}} \tag{21}$$

From these results the following conclusions can be drawn: (1) the net forces on a body having one or more source-sink discontinuities on its boundary are inde-

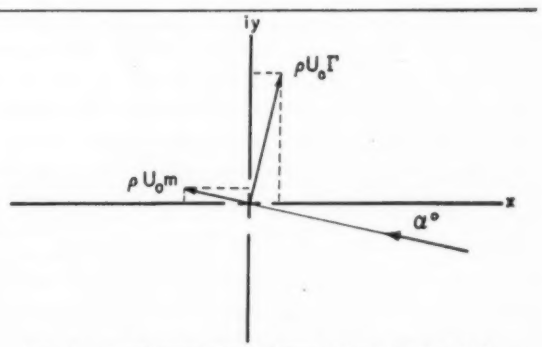

FIG. 4. Showing resultant forces defined by Eq. (20).

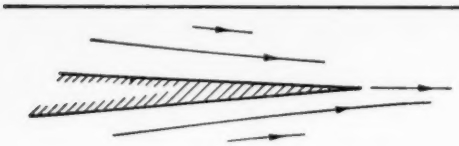

NORMAL
(a)

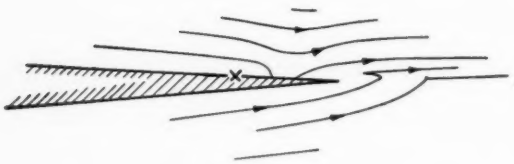

SUCTION JUST STARTED
(b)

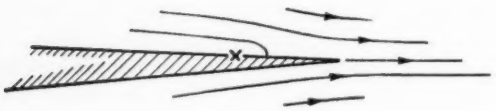

INCREASED CIRCULATION
(c)

FIG. 5. Showing how circulation is increased by suction slot.

terminate; but, if it be assumed that the fluid taken in or discharged from the body flows initially or finally along a spanwise path, then the external plus the internal forces are finite and given by Eq. (21). In particular, (2) the lift of a cylinder with one or more source-sink discontinuities on its boundary is, as in the case of a cylinder without such discontinuities, given by $L = \rho U_0 \Gamma$—i.e., the discontinuities themselves have no direct effect on lift, the external pressure changes being canceled by the internal pressure or inertia forces. (In Section (D) it will be shown, however, that for airfoils the Kutta condition couples the source strength to the circulation and thus indirectly results in a change in lift). (3) The drag of a cylinder with one or more source-sink discontinuities on its boundary is equal to the rate of change of momentum in the free stream. (It should be noted that this drag will be zero if the air taken in or discharged is subsequently discharged or previously taken in from the free stream.)

(C) *Applicability of Results to an Airfoil*

A circle may be transformed into any airfoil by means of a transformation function of the form

$$\zeta = z + \frac{a_1}{z^1} + \frac{a_2}{z^2} + \frac{a_3}{z^3} \cdots \frac{a_n}{z^n} \tag{22}$$

The best known systematic method for carrying out such a transformation is due to Theodorsen and is described in reference 3. Having the potential function w of the flow about a cylinder with a source-sink discontinuity on its boundary—i.e., Eq. (5)—one may determine the potential function for the flow about any airfoil, obtained by use of transformation (22), by substituting into Eq. (5) the inverse of the particular transformation used. The lift and drag of the airfoil may then be found using Eq. (7),

$$X - iY = (1/2)\rho i \oint_c (dw/d\zeta)^2 d\zeta \tag{23}$$

It is simpler, however, to obtain the required $(dw/d\zeta)$ directly by multiplying the first derivative of the potential function for the flow about the cylinder, (dw/dz) by the reciprocal of the derivative of the transformation function $(dz/d\zeta)$—i.e.,

$$(dw/d\zeta) = (dw/dz)(dz/d\zeta) \tag{24}$$

The lift and drag of the airfoil are then given by

$$X - iY = (1/2)\rho i \oint_{c_\zeta} \left(\frac{dw}{d\zeta}\right)^2 d\zeta =$$

$$(1/2)\rho i \oint_{c_z} \left(\frac{dw}{dz}\right)^2 \left(\frac{dz}{d\zeta}\right)^2 \left(\frac{d\zeta}{dz}\right) dz =$$

$$(1/2)\rho i \oint_{c_z} \left(\frac{dw}{dz}\right)^2 \left(\frac{dz}{d\zeta}\right) dz \tag{25}$$

Now from Eq. (22)

$$\frac{d\zeta}{dz} = 1 - \frac{a_1}{z^2} - \frac{2a_2}{z^3} - \frac{3a_3}{z^4} \cdots \frac{na_n}{z^{n+1}}$$

or

$$dz/d\zeta = 1 + (a_1/z^2)$$

Substituting into Eq. (25)

$$X - iY = (1/2)\rho i \oint_{c_z} \left(\frac{dw}{dz}\right)^2 \left(1 + \frac{a_1}{z^2} \ldots\right) dz \tag{26}$$

Substituting for $(dw/dz)^2$ from Eq. (9b), one finds that all integrals involving products with the a/z^n terms are zero, so that Eq. (26) reduces to

$$X - IY = (1/2)\rho i \oint_{c_z} (dw/dz)^2 dz$$

But the integral on the right is that carried out for the cylinder. *Thus, the forces acting on an airfoil are the same as those acting on a cylinder having the same circulation* Γ *and source strength* m. The conclusions, stated previously, of the effect of a suction slot on the forces on a cylinder are fully applicable to the airfoil—namely, *a source-sink discontinuity of itself produces no lift but, if, through some means it can be made to change the circulation about the airfoil, a change in lift will indirectly be produced.* The effect of the suction slot on the circulation is considered in the next section.

(D) *Effect of a Source-Sink Discontinuity on Circulation*

Flow around a sharp corner theoretically results in an infinite velocity. In the presence of a boundary layer through which pressure waves can propagate, an infinite velocity (and the associated pressure gradients) cannot be produced as a steady state. The only alternative condition that can be established is for a stagnation point to occur at the trailing edge. That the latter condition actually exists was first postulated by Kutta and has subsequently been experimentally demonstrated to correspond to reality. An airfoil develops lift as a result of the development of sufficient circulation to so place the stagnation point on the trailing edge. Therefore, to determine the lift on an air foil, one calculates the circulation required to place the stagnation point on the trailing edge and substitutes this value into the general solution $L = \rho U_0 \Gamma$ [see Eq. (21)].

Starting with Eq. (8), one may proceed to determine the circulation required to place the stagnation point at the trailing edge as follows:

$$\frac{dw}{dz} = -\frac{m}{2\pi}\left(\frac{2}{z - Re^{i\beta}} - \frac{1}{z}\right) - U_0 e^{i\alpha}\left(1 - \frac{R}{z^2}e^{-2i\alpha}\right) - \frac{i\Gamma}{2\pi}\frac{1}{z} \quad (8b)$$

This must be zero at the point on the cylinder which transforms into the trailing edge; or, it must be zero for

$$z = R^{i(\pi+\epsilon)} = -Re^{i\epsilon}$$

where $(\pi + \epsilon)$ is the value of θ for the particular point that transforms into the trailing edge. (ϵ is zero for symmetrical airfoils.)

Substituting into Eq. (8b)

$$\frac{dw}{dz} = -\frac{m}{2\pi}\left(\frac{2}{-Re^{i\epsilon} - Re^{i\beta}} + \frac{1}{Re^{i\epsilon}} - U_0 e^{i\alpha} \times \left(1 - \frac{R^2}{R^2 e^{2i\epsilon}}e^{-2i\alpha}\right) + \frac{i\Gamma}{2\pi}\frac{1}{Re^{i\epsilon}} = 0 \quad (27)$$

and solving for Γ, one obtains

$$\Gamma = -im\left(\frac{2e^{i\epsilon}}{-e^{i\epsilon} - e^{i\beta}} + 1\right) - i2\pi R U_0 e^{i(\alpha+\epsilon)} \times (1 - e^{-2i(\alpha+\epsilon)}) \quad (28)$$

Dividing top and bottom of the first term by $e^{i}[(\epsilon + \beta)/2]$ and the second by $2i$,

$$\Gamma = -m \tan\left(\frac{\epsilon - \beta}{2}\right) + 4\pi R U_0 \sin(\alpha + \epsilon) \quad (29)$$

Similarly, for an arbitrary number of discontinuities

$$\boxed{\Gamma = \sum_n -m_n \tan\left(\frac{\epsilon - \beta}{2}\right) + 4\pi R U_0 \sin(\alpha + \epsilon)} \quad (29a)$$

The second term in Eqs. (29) and (29a) may be recognized as the value of Γ for a normal airfoil having no discontinuities on its surface. It thus appears that, *if the circulation is determined by the Kutta condition, a source-sink discontinuity does change the value of the circulation*—i.e., the value of Γ, to place the stagnation point on the trailing edge—and as a result *does* indirectly change the lift.

The increment in circulation due to the discontinuities is given by

$$\boxed{\Delta\Gamma = -\sum_n \left(m_n \tan\frac{\epsilon - \beta_n}{2}\right)} \quad (30)$$

(E) *Net Effect of Discontinuities on Lift and Drag*

The lift and drag of an airfoil having source-sink discontinuities on its boundary are shown in sections (B) and (C) to be given by

$$\text{Lift} = \rho U_0 \Gamma$$

$$\text{Drag} = \rho U_0 \sum_n m_n$$

Substituting for Γ, Eq. (29a),

$$\left.\begin{aligned} L &= \rho U_0\left[4\pi R U_0 \sin(\alpha + \epsilon) - \sum_n m_n \tan\left(\frac{\epsilon - \beta_n}{2}\right)\right] \\ D &= \rho U_0 \sum_n m_n \end{aligned}\right\} \quad (31)$$

The chord of this airfoil will be very nearly $4R$. Thus,

$$\left.\begin{aligned} C_L &= 2\pi(\alpha + \epsilon) - 2\sum_n \frac{m_n}{U_0 c}\tan\left(\frac{\epsilon - \beta_n}{2}\right) \\ C_D &= 2\sum_n \frac{m_n}{U_0 c} \end{aligned}\right\} \quad (32)$$

where $m_n/U_0 c$ is the flow coefficient usually denoted C_Q.

Since, for a normal airfoil,

$$\left.\begin{aligned} C_L &= 2\pi(\alpha + \epsilon) \\ C_D &= 0 \end{aligned}\right\} \quad (33)$$

it is apparent that the increments in lift and drag due to the source-sink discontinuities are

$$\boxed{\begin{aligned} \Delta C_L &= +2\sum_n C_{Q_n}\tan\left(\frac{\beta_n - \epsilon}{2}\right) \\ \Delta C_D &= 2\sum_n C_{Q_n} \end{aligned}} \quad (34)$$

The lift increment given by Eqs. (34) is plotted in Fig. 6 vs. $(\beta_n - \epsilon)/180°$. $(\beta - \epsilon) = 0$ corresponds to a discontinuity at the nose, and $\beta = \pi + \epsilon$ corresponds to a discontinuity at the tail. Positive β's correspond to points on the upper surface and negative β's to points on the lower surface. The exact value of β_n corresponding to any given slot location on a specific airfoil is determined as in reference 3. β_n of the present

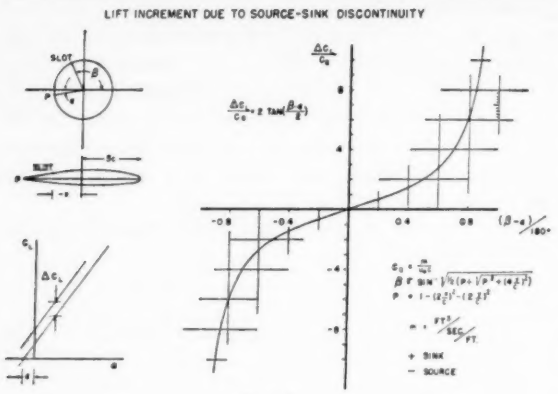

FIG. 6.

paper, in terms of the notation of reference 3, is given by

$$\beta_n = \varphi = \theta + \epsilon \tag{35}$$

where

$$\theta = \sin^{-1}\sqrt{(1/2)[P + \sqrt{P^2 + (4y/c)^2}]}$$

$$P = 1 - (2x/c)^2 - (2y/c)^2$$

(x and y are measured as shown in Fig. 6 of the present paper)

$$\epsilon = -\frac{1}{2\pi}\int_0^{2\pi} \psi(\varphi) \cot \frac{\varphi - \varphi'}{2}\, d\varphi$$

The ϵ of reference 3 will normally be small relative to θ, so that a good approximation for β_n is obtained by writing Eq. (35) as

$$\beta_n = \varphi \cong \theta \tag{36}$$

The following specific conclusions can be drawn from these results.

(1) A sink, or suction slot, on the upper surface of an airfoil increases the lift by an amount directly proportional to its strength. This increment is independent of angle of attack but is a function of the chordwise location of the discontinuity.

(2) A sink or suction slot on the lower surface has just the opposite effect.

(3) The drag increment is equal to the rate at which free-stream momentum is removed from the stream by the sink and is independent of angle of attack and position.

(4) A source or an equivalent pressure slot has in every respect the opposite effect from the sink.

(III) Comparison with Experiment

In order to confirm the practical validity of Eq. (34), a 16-012 airfoil with a single suction slot at 95 per cent c has been tested in the two-dimensional U.A.C. laminar flow tunnel. The results are summarized and compared with the theory in Fig. 8. It is apparent that the effectiveness of the slot is considerably greater than indicated by the theory until the boundary layer has been removed. From here on the purely hydrodynamic effect of the slot becomes dominant and the rate of increase in lift is as indicated by the theory. The potential solution is thus confirmed within the limitations of its assumptions.

(IV) Practical Applications of Solution

From a practical point of view the most interesting aspect of these results is the large lift increment associated with a suction slot located at or near the trailing edge. Such an effect has been experimentally observed by Regenscheit[6] and is confirmed by the U.A.C. tests. It is to be remembered that this effect differs basically from that usually associated with suction slots in that it is a purely hydrodynamic effect and has nothing to do with boundary-layer removal.

As is apparent from the solution presented in the previous sections, the physical explanation for this increase in lift lies in the effect of such a slot on the

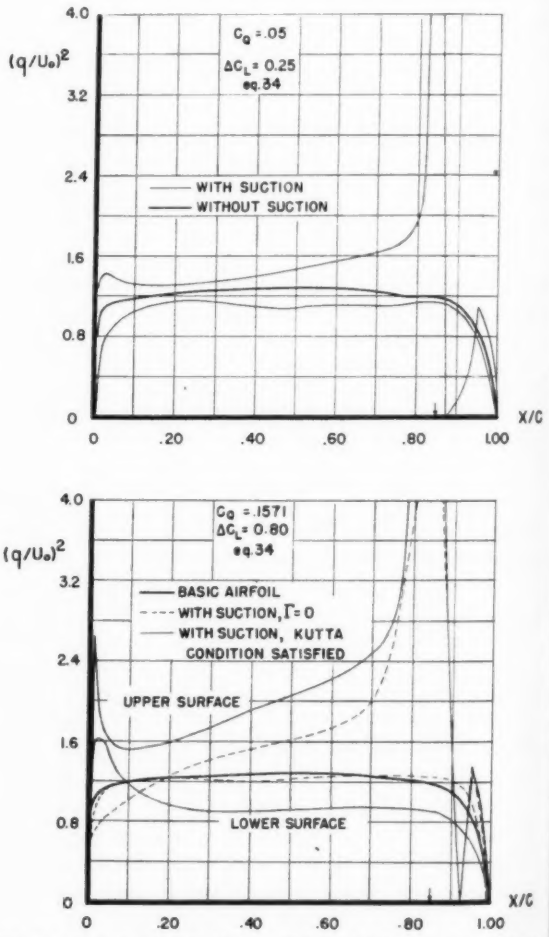

FIG. 7. Velocity distribution on 16-012 airfoil with and without suction. Slot located at 85 per cent chord. $\alpha = 0°$.

trailing-edge stagnation point. The explanation is briefly as follows: Normally the circulation about an airfoil is determined by, and is just sufficient to place, the stagnation on the trailing edge. (See Fig. 5a.)

When suction is applied on the upper surface and particularly when it is applied near the trailing edge, a forward increment of velocity is induced at all points behind the slot, including the region near the tail. As a result, the stagnation point occurs before the trailing edge is reached (see Fig. 5b). A condition analogous to the Kutta condition is thus established, the lower surface flow in attempting to flow around the sharp trailing edge separating. The upper surface flow accelerates in the face of the vacuum thus created and flows smoothly off the tail (Fig. 5c). The net effect is an increase in circulation, which, it can be said, is sufficient to place the stagnation point on the trailing edge. It is this increase in circulation which causes the increase in lift. The theory indicates that the equivalent of a source on the lower surface will produce the same effect.

In Fig. 7 the pressure distribution on a 16-012 airfoil at $\alpha = 0$ with a suction slot at 85 per cent is shown. The no-suction computation was made using the potential functions (3) and (5)* of the present report in combination with Theodorsen's method. The $\Gamma = 0$ curve in this figure is of considerable interest. It is apparent that there is considerable (though indeterminate) external lift due to the action of the slot alone. But the net lift including the internal forces as indicated by Eq. (21) is zero for this case. Thus the lift represented by this pressure distribution is equal to the internal momentum reaction. The difference between the $\Gamma = 0$ and Γ to satisfy the Kutta condition curves represents the net effective lift.

It is also significant that a favorable pressure gradient exists right up to the slot, so that such a slot would not only increase C_L by increasing circulation but would also tend to prevent separation and therefore increase $C_{L_{max.}}$.

From Fig. 7 it is apparent that, as C_Q is increased, the stagnation point following the slot moves back toward the trailing edge. When this stagnation point reaches the tail and subsequently moves on under to the lower surface, the Kutta function of the trailing edge is lost, and it is not clear what will happen. In any event, it is clear that the analysis presented in this paper is no longer applicable. Thus, although the C_L increment corresponding to a given C_Q increases as the slot is moved back toward the tail, from the preceding comments it is apparent that the maximum C_Q for which the analysis is applicable decreases. Thus, it does not necessarily follow that the maximum ΔC_L will occur with the slot as near as physically possible to the tail. Consideration of these points must await experimental observations.

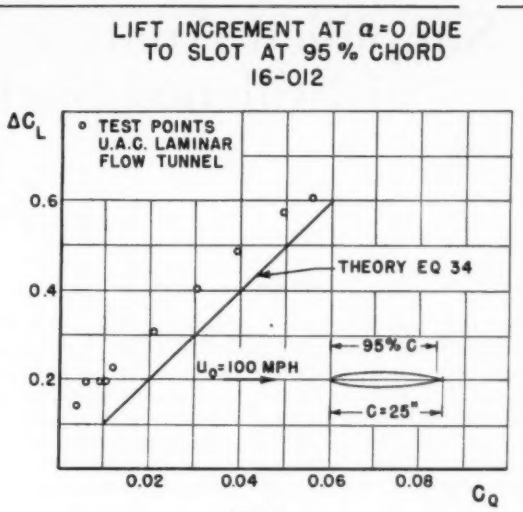

FIG. 8.

* Γ is assigned the Kutta value as given by Eq. (29a).

REFERENCES

[1] Joukowsky, *The Theoretical Basis of Aeronautics;* Moscow, 1912.

[2] Glauert, H., *The Elements of Aerofoil and Airscrew Theory;* The Macmillan Company, New York, 1943.

[3] Theodorsen, T., *The Theory of Wing Sections of Arbitrary Shape,* N.A.C.A. T.R. No. 411, 1931.

[4] Allen, J., *General Theory of Airfoil Sections Having Arbitrary Shape or Pressure Distribution,* N.A.C.A. T.R. No. 833, 1945.

[5] Franklin, P., *Methods of Advanced Calculus;* McGraw-Hill Book Company, Inc., New York, 1944.

[6] Regenscheit, *Investigation of a Wing with Trailing Edge Suction,* Goettingen report 41-4-14, May, 1942 (translation available through U.A.C. Library).

Simplified Analysis of General Instability of Stiffened Shells in Pure Bending

F. R. SHANLEY*

The RAND Corporation

SUMMARY

Although much work[1-3] has been done to develop a theory for the failure of shells by general instability, there is at present no simple method by which the size of the frames may be determined for any given diameter, bending moment, and frame spacing. Such a method is needed in determining the optimum design for stiffened shells, to be used as a basis for weight analysis of fuselages, and other shell structures. In an extension of the work done for The RAND Corporation,[4] a simple coefficient has been determined for this purpose. Since it appears that this method may also be useful in design calculations, a brief description is presented below.

DESCRIPTION OF THE METHOD

THE ORIGINAL PROBLEM that caused the C.A.A. to inaugurate the investigations that have been under way for over 10 years was to determine whether the frames were strong enough to ensure failure of the sheet-stringer panels between frames—i.e., *to prevent general instability*. That is still the primary concern of the designer; we have much less need for a theory that will predict the ultimate bending moment of a shell in which the frames are not stiff enough to do this.

For shells that are designed to fail through panel instability, it is possible to make use of the fact that a column loses its resistance to bending as its critical (buckling) load is approached.

As the sheet-stringer elements near the most highly loaded point on the shell approach their critical load as columns, they tend to behave like hinged bars, with spring supports furnished by the frames.[5] From the photographs of general instability failures,[2] it appears that the proper model for a single element would be two bars hinged midway between two frames and at adjacent frames, as shown in Fig. 1. The two middle frames would be replaced by springs, for which the spring constant required to prevent buckling can be computed from the geometry of the slightly deflected bars.

The equation for the required spring constant, α, may be written

$$\alpha = P_1 K/L \tag{1}$$

where P is the axial load and L is the frame spacing.

For the assumed model, $K_1 = 3/2$. For two bars, each of length L, supported by one spring, the constant equals 2.0. Since the value of the constant will not be used directly, the type of model assumed is not important. The only assumption that need be made is that the mode of failure remains the same.

If the sheet-stringer elements are considered to be uniformly distributed around a shell of circular cross section, the maximum axial load per unit of circumference equals the bending moment divided by the enclosed area [see Eq. (39), reference 4]:

$$q_{max.} = 4M/\pi D^2 \tag{2}$$

where M is the bending moment and D is the mean diameter of shell.

If this maximum value of q is considered to apply over some constant fraction of the shell circumference,[4] Eq. (2) may be written

$$P_{eq.} = K_2 M/D \tag{3}$$

This value may be substituted in Eq. (1) to obtain the required spring constant for the frame. The effective spring constant for a circular frame under diametrically opposed loads may be written in the form[6]

$$\alpha = K_3 (EI)_f/D^3 \tag{4}$$

where $(EI)_f$ is the effective frame stiffness in bending.

The value of K_3 may be considered to remain constant for a given distribution of the loading forces. (Nonlinear effects are assumed to be small and are also included indirectly in the final evaluation of the coefficient.)

Eqs. (1), (3), and (4) may be combined to give an expression for the required frame stiffness:

$$(EI)_f = C_f M D^2/L \tag{5}$$

If it could be shown that the coefficient C_f is nearly constant for any given cross-sectional shape, Eq. (5) could be used for the design of the frames. At the present time, the best approach seems to be to deter-

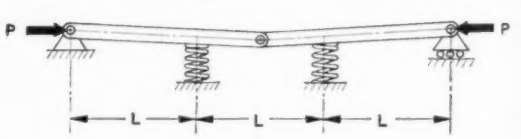

FIG. 1

Received May 20, 1949.

* Consultant. Also Lecturer at the University of California at Los Angeles.

TABLE 1

Test Data from N.A.C.A. Technical Note No. 909

(Pure Bending, Aluminum-Alloy Material, E assumed = 10×10^6 Lbs. per Sq.In., P = Panel Failure, G = General Instability, P/G = Combination, D = Diameter, L = Frame Spacing, I_f = Moment of Inertia of Frame)

Test No.	D, In.	L, In.	I_f, In.^{4} $\times 10^5$	$M_{ult.}$, In.Lb. (See Note 1)	C_f $[= L(EI)_f/MD^2]$ $\times 10^5$	Type of Failure
25	31.84	8	1.537	219 000	0.554	G
26	31.84	4	1.537	270 000	0.225	G
27	31.84	2	1.537	340 000	0.089	G
28	31.84	16	1.537	168 500	1.438	P/G
29	31.84	16	1.537	123 000	1.972	P
30	31.84	8	1.537	107 500	1.128	G
31	31.84	4	1.537	137 500	0.441	G
32	31.84	2	1.537	185 000	0.164	G
34	31.84	16	1.537	45 000	5.376	P/G
35	31.84	8	1.537	58 500	2.074	G
36	31.84	4	1.537	75 000	0.808	G
37	31.84	2	1.537	100 000	0.303	G
38	31.84	1	1.537	209 000	0.072	G
39	31.84	1	1.537	397 000	0.038	G
40	31.84	16	1.537	222 300	1.091	P
41	31.84	8	1.537	283 600	0.428	G
42	31.84	4	1.537	336 500	0.180	G
43	31.84	2	1.537	380 000	0.080	G
44	31.84	16	1.537	108 000	2.247	P
45	31.84	8	1.537	163 000	0.744	G
46	31.84	4	1.537	186 000	0.326	G
47	31.84	2	1.537	263 000	0.115	G
48	31.84	16	1.537	59 000	4.115	P
49	31.84	8	1.537	82 000	1.479	G
50	31.84	4	1.537	97 500	0.622	G
51	31.84	2	1.537	153 000	0.198	G
52	32.00	16	31.194	165 000	29.411	P
53	32.00	8	31.194	290 000	8.403	P
54	32.00	4	31.194	434 000	2.808	G
55	32.00	2	31.194	460 000	1.324	G
56	32.00	16	31.194	75 000	66.667	P
57	32.00	8	31.194	134 000	18.181	P
58	32.00	4	31.194	220 000	5.524	G
59	32.00	2	31.194	284 000	2.145	G
60	32.00	8	27.400	169 000	12.658	P
61	32.00	4	27.400	256 000	4.184	G
63	32.00	4	27.400	436 000	2.457	G
64	32.00	2	27.400	500 000	1.070	G
65	20.00	4	1.537	110 000	1.396	G
66	20.00	2	1.537	140 000	0.549	G
67	20.00	4	1.537	66 500	2.309	G
68	20.00	2	1.537	79 000	0.973	G
73	20.00	4	1.537	117 000	1.314	G
74	20.00	2	1.537	150 000	0.512	G

NOTE 1: These values are not given in the original report but were obtained from California Institute of Technology through Dr. E. E. Sechler.

TABLE 2

Test Data from N.A.C.A. Technical Note No. 1499

(Pure Bending, Aluminum-Alloy Material, E assumed = 10×10^6 Lbs. per Sq.In., P = Panel Failure, G = General Instability, P/G = Combination, D = Diameter, L = Frame Spacing, I_f = Moment of Inertia of Frame)

Test No.	D, In.	L, In.	I_f, In.^{4} $\times 10^5$	$M_{ult.}$ In.Lb.	C_f $[= L(EI)_f/MD^2]$ $\times 10^5$	Type of Failure
44	20	7.07	6.10	273 000	3.96	G
45	20	7.07	8.15	280 000	5.15	G
47	20	7.07	41.30	380 500	19.22	P/G
48	20	7.07	16.30	337 500	8.55	G
49	20	7.07	65.00	403 500	28.60	P
50	20	5.79	8.15	251 500	4.70	G
51	20	6.43	8.15	246 500	5.32	G
52	20	5.79	8.15	486 500	2.43	G
53	20	9.00	6.10	508 500	2.70	G
54	20	6.43	6.10	553 500	1.77	G
55	20	5.79	8.15	553 300	2.14	G
58	20	9.00	12.20	460 600	5.95	P/G
59	20	9.00	8.15	451 000	4.07	P/G
60	20	9.00	27.50	451 000	13.70	P
61	20	9.00	6.10	403 000	3.40	G

mine a value of C_f from test data, such that the probability of general instability would be reduced to an acceptable minimum.

To do this, the test data from references 1 and 2 have been analyzed (ultimate bending moments for the tests of reference 1 were obtained from Dr. E. E. Sechler, of California Institute of Technology). (See Tables 1 and 2.) The coefficient was calculated from Eq. (5):

$$C_f = (EI)_f L/MD^2 \tag{6}$$

On Fig. 2, the test points have been plotted against C_f so as to show the number of general instability and panel failures within each increment of C_f. There is a fairly large range within which both types of failure occur. The probability of either type of failure at any given value of C_f is more clearly indicated by the summation curves. The top curve, for example, gives the number of general instability failures that occurred *above* a given value of C_f. On this basis it appears that a value of $C_f = 6.25 \times 10^{-5}$ $(= 1/16{,}000)$ represents a safe figure for the shells tested.

The wide range of overlap does not necessarily indicate that the theory from which C_f was derived is correspondingly inaccurate. In reference 2, for example, a wide range was given for the parameter Λ to describe the transition zone within which either type of failure may occur. A certain amount of such overlap will be caused by imperfections. In any structure designed on an optimum basis, the probability of a reduction in load capacity is increased by the fact that either of two types of imperfections may be expected. This also widens the range in which either type of failure may be expected to occur.

Incidentally, it can be shown that C_f can be converted into the form K/Λ (where K is a constant and Λ is the parameter used in reference 2) by assuming that the critical load per stringer is given by the Euler formula. One great advantage of the coefficient C_f is that it does not contain any of the properties of the sheet-stringer combination. This permits the frame problem to be handled independently of all the usual complications of the panel problem, such as inelastic effects, effective width, interrivet buckling, etc. The coefficient C_f brings the bending moment directly into the calculation of frame stiffness, while the parameter Λ does so indirectly through the effective EI of the sheet-stringer

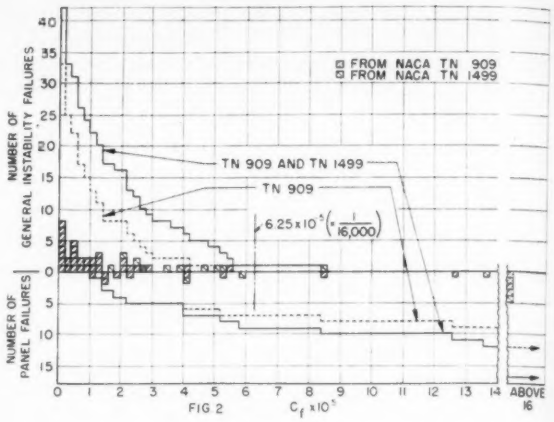

FIG 2

combination. It might also be possible that the critical conditions for general instability occur first over a fairly small area, in which case the present analysis would perhaps represent the conditions better than a theory based on the appearance of the structure *after* buckling.

Fig. 2 shows the need for more tests in the transition region. It is to be hoped that future research will be directed toward determining how to prevent general instability rather than how to predict it. There is an urgent need, also, for tests of shells that more closely resemble the type of construction actually used, with more efficient frames located on the inside of the shell.

Finally, the effective EI of various types of frames should be investigated, including the effects of the shell thickness.

References

[1] Dunn, Louis G., *Some Investigations of the General Instability of Stiffened Metal Cylinders*, Part IX, N.A.C.A. T.N. No. 1198, November, 1947.

[2] Hoff, N. J., Boley, Bruno A., and Hardo, S. V., *The Inward Bulge Type Buckling of Monocoque Cylinders Subjected to Pure Bending*, N.A.C.A. T N. No. 1499, September, 1948.

[3] Hoff, N. J., *Thin-Walled Monocoques*, First International Conference, R.Ae.S.-I.A.S., London, September, 1947.

[4] Shanley, F. R., *Principles of Structural Design for Minimum Weight*, Journal of the Aeronautical Sciences, Vol. 16, No. 3, p. 133, March, 1949.

[5] Timoshenko, S., *Theory of Elastic Stability*, p. 106; McGraw-Hill Book Company, Inc., New York, 1936.

[6] Timoshenko, S., *Strength of Materials*, Vol. II, p. 82; D. Van Nostrand Company, New York, 1941.

A New High-Performance Engine Indicator of the Strain-Gage Type

C. S. DRAPER* AND Y. T. LI†
Massachusetts Institute of Technology

ABSTRACT

Pressure changes in the working fluid largely determine the performance of heat engines. For this reason, accurate pressure indications are of primary importance for studies of engine operation. Pressure indicators have been in use for many years, but performance defects have restricted their value even for laboratory and test-stand work. The operating limitations have been due to the fact that available pressure receivers have been sensitive not only to pressure but also to temperature, to mechanical strains due to mounting effects, and to mechanical vibrations in the walls of the pressure chamber. It is the purpose of this paper to describe the features of a new pressure receiver using a high-flexibility catenary-type diaphragm and a temperature-compensating wire-wound strain gage to give satisfactory pressure-measuring characteristics with greatly reduced response to temperature and extraneous mechanical effects.

(I) PERFORMANCE REQUIREMENTS FOR ENGINE PRESSURE INDICATORS

ENGINE-PRESSURE INDICATORS receive pressure variations in the working fluid and produce indications or records of these fluctuations. Records of two general types are in common use: (1) average pressure records and (2) continuous pressure records.

Average pressure records are possible only from equipment that operates with repetitive cycles, such as reciprocating piston engines. Continuous pressure records may be taken from all kinds of engines and turbine-type power plants and from research chambers using nonrepetitive explosions.

To be generally satisfactory, continuous pressure indicators[1–25, 29, 31] must be able to withstand engine operating conditions for reasonable periods and give satisfactorily accurate records for both low- and high-frequency pressure variations. The low-frequency variations to be measured are directly associated with the power generation phase of engine operation; the high-frequency variations involved may be associated with detonation, shock waves inside a closed chamber, or air pulsations within an induction system. In addition to these primary operating characteristics, the pressure datum line and the calibration of a satisfactory indicator must be unaffected by environmental effects such as temperature and extraneous strains. Unless this condition is fulfilled, pressure measurements of high accuracy are difficult to realize, because a calibration based on a constant environmental temperature will not be valid for an actual indicator installation subjected to the fluctuating temperatures accompanying power-plant operation.

In addition to the calibration-changing effects of temperature and installation strains, pressure indicators are subject to dynamic errors due to inertia reaction forces acting on mechanical parts. These forces produce distortions in the records of rapidly changing pressures and, in addition, cause an indicator to respond to vibrations of the wall to which it is attached. The reduction of inertia reaction effects to tolerable levels is one of the primary objectives of pressure-indicator design.

Averaging indicators[26–29] are designed to overcome the inaccuracy-producing effects usually present in continuous pressure indicators by removing the calibrated parts of the system from the influence of engine temperature and vibration. This is achieved by designing the system so that only a *pressure equality sensitive* unit is exposed to the working fluid pressure. In the indicator, a slowly varying pressure is applied to a calibrated pressure recording unit, and each engine cycle places a single point on paper carried by a rotating drum connected to the engine shaft, when the working fluid pressure becomes equal to the external pressure. This system satisfactorily avoids inaccuracies due to temperature and dynamic effects but can be applied only to engines giving repetitive cycles and, in any case, is unable to record high-frequency pressure oscillations.

The discussion that follows describes a *continuous pressure indicator* that is substantially free from the common defects of previously existing indicators. Design features are described, and the performance

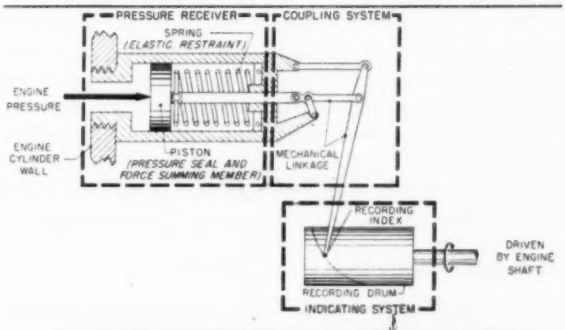

FIG. 1. SCHEMATIC DIAGRAM OF PISTON AND SPRING TYPE PRESSURE INDICATOR.

Presented at the Instruments Session, Seventeenth Annual Meeting, I.A.S., New York, January 24–27, 1949.

* Professor of Aeronautical Engineering and Director of Instrumentation Laboratory.

† Research Associate in Aeronautical Engineering.

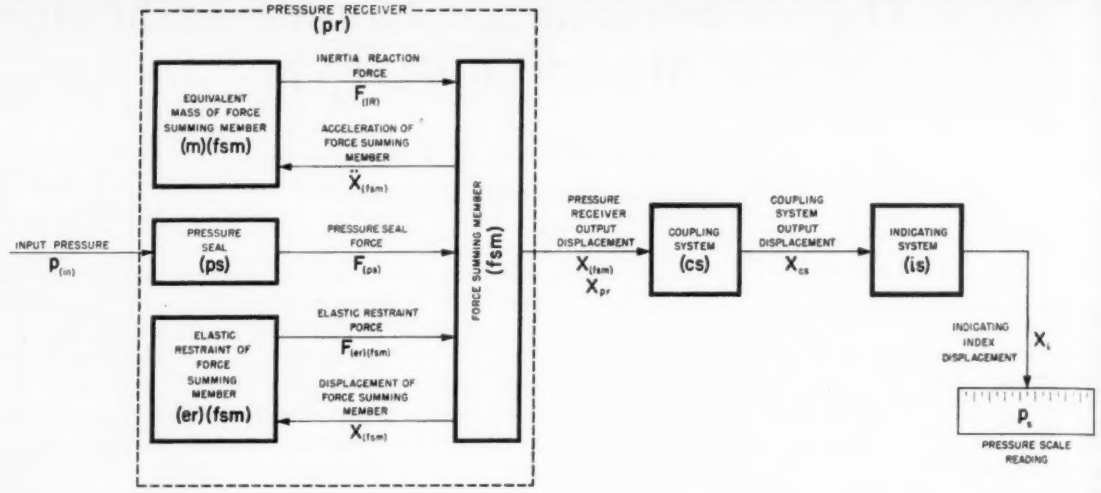

FIG. 2 FUNCTIONAL DIAGRAM FOR PRESSURE INDICATOR USING A PRESSURE RECEIVER WITH MECHANICAL DISPLACEMENT OUTPUT.

characteristics realized are reported from data taken in laboratory and engine tests.

(II) General Features of Engine Indicators

Piston and Spring Engine Indicator[30]

Engine pressure records were first made by means of the piston and spring arrangement introduced by James Watt and commonly called the *steam engine indicator*. A schematic diagram of this arrangement is shown in Fig. 1 and a corresponding functional diagram is given in Fig. 2. In this type of indicator, the part of the piston exposed to the pressure to be measured supplies the *pressure seal*, which receives pressure as the *actuating input* and applies a corresponding force to the piston, which acts as the *force summing member*. A coil spring placed between the body of the indicator and the piston is the *elastic restraint*, which reacts on the force summing member with a force proportional to the linear displacement of this member with respect to the cylinder. A mechanical linkage serves as the *coupling system* by transferring the pressure receiver output deflection to the *indicating system*, which consists of the *recording index* and a rotating drum driven by the engine shaft.

The usefulness of the steam engine indicator is limited by the relatively large mass of its moving parts and the amount of gas flow required to change the pressure acting on the piston. These characteristics make it impossible for conventional piston and spring indicators to give satisfactory records of the high-frequency oscillations associated with detonation, or even the rapid pressure fluctuations of high-speed engine operations.

Averaging Pressure Engine Indicator[26–29]

The schematic diagram of Fig. 3 illustrates the principle used by designers of balanced pressure diaphragm indicators to retain the simplicity and reliability of the piston and spring system for converting pressure levels into indicator record deflections and, at the same time, to remove calibrated parts from the severe temperature and vibration conditions of engine operations. As shown in this figure, an external source of high pressure is applied to the piston and to the outer side of a diaphragm exposed to the engine pressure on its inner surface. A contact that is effective in the primary circuit of an induction coil causes a spark to pass from the recording index electrode through recording paper when the pressure moves the diaphragm against or away from the contact to give a make or break of the circuit.* The recording paper is carried by a rotating drum driven from the engine shaft. An indicator card is made by slowly varying the external pressure until the

* In practice, an electronic circuit is often used between the pressure equality indicating diaphragm and the induction coil. With this arrangement, the current broken by the contacts is greatly reduced from the current that would be required if the full primary current passed through the contacts.

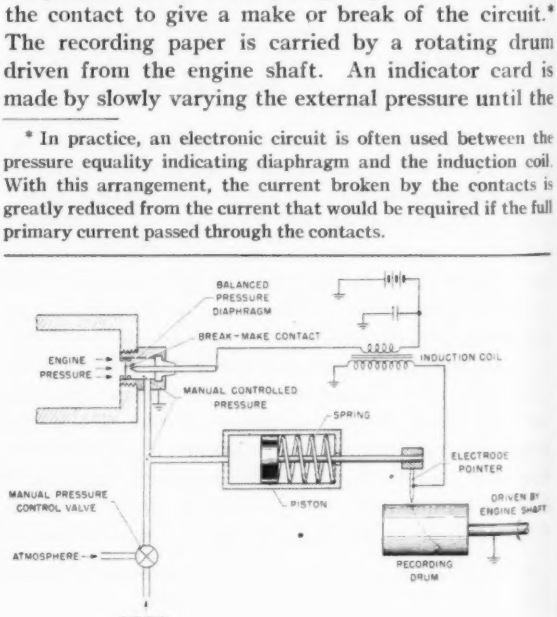

FIG. 3. SCHEMATIC DIAGRAM OF BALANCED DIAPHRAGM TYPE AVERAGING PRESSURE INDICATOR

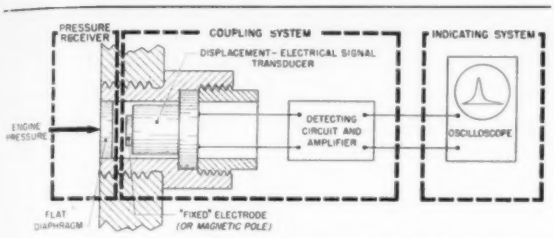

FIG. 4. FLAT DIAPHRAGM TYPE ENGINE PRESSURE INDICATOR WITH ELECTRICAL COUPLING SYSTEM AND OSCILLOSCOPE INDICATING SYSTEM.

single points, or pair of points, made on the record for each power cycle of the engine combine to produce a complete average pressure crank angle record.

In addition to the system of Fig. 3, average-pressure records may be made up from a piston, spring, and drum arrangement like that shown in the figure but including a sampling valve[29] to replace the balanced pressure diaphragm. The sampling valve, which is mounted in the pressure vessel wall, is arranged to open for a short time at a controllable crank position angle corresponding to the recording drum position. This causes the pressure acting on the indicating piston and spring to build up to a level substantially equal to the engine-cycle pressure for the crank angle setting used. By making settings for the proper number of crank angles, a complete indicated pressure cycle record may be taken.

It is obvious from the description of the preceding paragraph that averaging indicators are not suitable for making pressure records of rapidly fluctuating pressures that are not exactly repeated a large number of times. Because of this defect, averaging indicators cannot be used for recording nonrepetitive pressure changes or high-frequency oscillations.

Flat-Diaphragm Type Engine Indicator[1, 2, 5, 6, 8–11, 13, 31]

The need for continuous pressure records in all fundamental investigations of engine performance has produced many attempts to construct equipment without the operating deficiencies of the piston and spring indicator. In this direction, one of the fundamental modifications to the system of Fig. 1 has been to reduce the ratio of the mass to the elastic restraint of the moving parts of the pressure receiver in order to improve its response to rapid pressure changes. In many designs, this has been achieved by replacing the piston and spring system with a flat diaphragm, as indicated in the schematic diagram of Fig. 4. In this diagram, the flat diaphragm combines within itself all the functions of the pressure receiver of Fig. 2 in the sense that it acts as the pressure seal, the elastic restraint, and the force summing member. At the same time, it determines the equivalent mass of the moving system and supplies the pressure receiver output as the effective displacement of its central area.

The output displacements of a flat diaphragm pressure receiver are generally so small that the coupling and indicating systems used must be based on either optical[13, 31] or electrical[1] principles. Because of their fragility and bulk, optical systems are more useful for special laboratory investigations than for general engine work. When, as in Fig. 4, the diaphragm output displacement is used to vary an air gap, the electrical coupling system can be designed to operate on the resulting change in either the electromagnetic reluctance[1] or the electrostatic capacity.[2, 11] In an indicator of this kind, an electronic amplifier completes the coupling system and supplies electrical signals to some type of recording oscillograph.

At the present time, amplifiers and oscillographs are so well developed that the electrical components required for high-performance coupling and indicating systems are easily available. There are many designs possible for systems of this type which will operate without imposing functional limitations of any kind on the pressure-indicating equipment in which they are used, for which reason the performance possible from a pressure indicator is usually determined mainly by the characteristics of the pressure receiver.

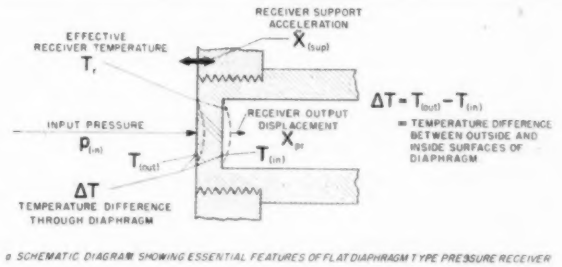

a SCHEMATIC DIAGRAM SHOWING ESSENTIAL FEATURES OF FLAT DIAPHRAGM TYPE PRESSURE RECEIVER

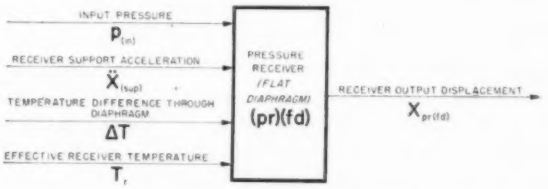

b FUNCTIONAL DIAGRAM OF FLAT DIAPHRAGM TYPE PRESSURE RECEIVER

$$S_{pr(p,X)(fd)} = \frac{\partial X_{pr(fd)}}{\partial p_{(in)}}$$ = PRESSURE INPUT - DISPLACEMENT OUTPUT SENSITIVITY OF PRESSURE RECEIVER.

$$S_{pr(\ddot{X},X)(fd)} = \frac{\partial X_{pr}}{\partial \ddot{X}_{(sup)}}$$ = ACCELERATION INPUT - DISPLACEMENT OUTPUT SENSITIVITY OF PRESSURE RECEIVER.

$$S_{pr(\Delta T,X)(fd)} = \frac{\partial X_{pr}}{\partial \Delta T}$$ = TEMPERATURE DIFFERENCE INPUT - DISPLACEMENT OUTPUT SENSITIVITY OF PRESSURE RECEIVER.

$$(SR)_{pr(\ddot{X},p)(fd)} = \frac{S_{pr(\ddot{X},X)}}{S_{pr(p,X)}}$$ = PRESSURE INPUT - ACCELERATION INPUT SENSITIVITY RATIO OF PRESSURE RECEIVER.

$$(SR)_{pr(\Delta T,p)(fd)} = \frac{S_{pr(\Delta T,X)}}{S_{pr(p,X)}}$$ = PRESSURE INPUT - TEMPERATURE DIFFERENCE INPUT SENSITIVITY RATIO OF PRESSURE RECEIVER.

c STATIC PERFORMANCE CHARACTERISTICS OF FLAT DIAPHRAGM TYPE PRESSURE RECEIVER

FIG. 5. SCHEMATIC DIAGRAM, FUNCTIONAL DIAGRAM, AND STATIC PERFORMANCE CHARACTERISTICS OF FLAT DIAPHRAGM TYPE RECEIVER.

(III) Performance Limiting Characteristics of Flat-Diaphragm Pressure Receivers

General Characteristics of Flat-Diaphragm Pressure Receivers[1-4]

Engine indicators intended for use with high-speed engines have usually been designed with pressure receivers that are either flat diaphragms or have the flat-diaphragm shape nearly enough for the elastic theory associated with this shape to be valid within reasonable limits. For this reason, it is possible to discuss the general problems of pressure-receiver design in terms of the elastic theory of flat diaphragms.[3, 4]

The schematic diagram and the corresponding functional diagram, shown in Fig. 5, represent the essential operating characteristics of a flat-diaphragm pressure receiver under static conditions. By definition, static conditions exist when both the essential input and the corresponding output are constant. The static characteristics can be expressed in terms of *sensitivities*, where a particular sensitivity is determined as the ratio of a small output change to the corresponding small input change when all the other essential quantities are held constant. For example, the pressure-displacement sensitivity of a flat diaphragm pressure receiver is equal to the ratio of the displacement of the diaphragm center to the pressure applied to the diaphragm.

Metallic diaphragms applied as pressure receivers are affected by four input quantities:

(1) Pressure applied to the outer surface of the diaphragm.

(2) Linear acceleration of the diaphragm support in the direction at right angles to the diaphragm surface.

(3) Temperature gradient in the material of the diaphragm between its inner and outer surfaces.

(4) Average temperature of the diaphragm material.

Pressure, the first of these quantities, is the desired actuating input for a pressure receiver. Linear acceleration of the diaphragm support and temperature gradient in the diaphragm material cause undesired deflections that are not distinguishable from pressure effects. Changes in the average temperature of the diaphragm do not of themselves cause output deflections but act as a modifying input by affecting the elastic constants (modulus of elasticity and Poisson's ratio) of the diaphragm material and so altering the sensitivities of the diaphragm for other inputs.[3, 4]

In addition to its static performance, as measured by the sensitivities of Fig. 5, the dynamic characteristics of a pressure receiver are important. By definition,[3, 4] dynamic conditions exist when the relationship between an output quantity and the corresponding input quantity depends upon the rates at which these quantities are changing. For an operating component like the flat diaphragm, which has relatively low damping, the essential factor in determining the dynamic characteristics of the component is its undamped natural frequency. Fig. 6 gives a plot of the undamped natural frequency for a $^1/_2$-in. diameter flat steel diaphragm as a function of the diaphragm thickness.[3, 4] It appears from this plot that the undamped natural frequency of this flat steel diaphragm is a linear function of the diaphragm thickness, with a thickness of 0.064-in. giving a natural frequency of about 100,000 cycles per sec. In general, for a given frequency of the input pressure, the undesirable effects of dynamic conditions are reduced as the natural frequency of the diaphragm is increased. The second curve of Fig. 6 shows the considerable cost, in terms of reduced pressure-deflection sensitivity, of increasing the diaphragm thickness to improve the dynamic response characteristics.

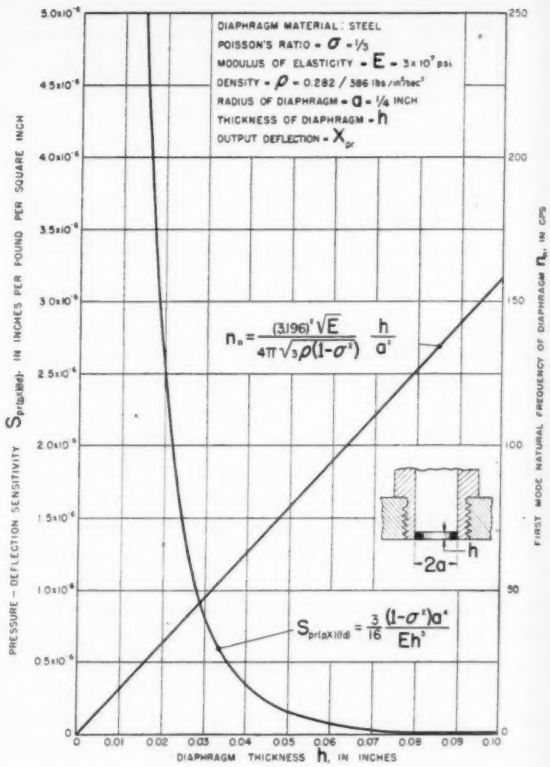

FIG. 6 PRESSURE-DEFLECTION SENSITIVITY AND UNDAMPED NATURAL FREQUENCY OF FLAT DIAPHRAGM TYPE PRESSURE RECEIVER AS FUNCTIONS OF DIAPHRAGM THICKNESS.

In practice, the coupling system-indicating system combination of a pressure indicator receives the output deflection of the pressure receiver and produces a deflection of the recording index. The input deflection is received without consideration of the extent to which the effects of linear acceleration and temperature gradient may have entered into the resultant. Because the indicating system record is interpreted in terms of pressure, it is important to have information available for estimating the effects of linear acceleration and temperature gradient in terms of the pressure acting on the pressure receiver. This information is supplied by the sensitivity ratios defined in Fig. 5. The acceleration-

pressure sensitivity ratio is the ratio of the acceleration - deflection sensitivity to the pressure - deflection sensitivity. It has the dimensions of pressure divided by acceleration and represents the amount of pressure that would be required to produce the same diaphragm output deflection as a unit acceleration of the support. In a similar way, the pressure - temperature gradient sensitivity ratio represents the pressure that would be required to produce the same output deflection as a unit temperature gradient through the diaphragm.

Effect of Linear Acceleration of the Support on a Flat-Diaphragm Pressure Indicator

The curves of Fig. 7 show the way that the acceleration - pressure sensitivity ratio varies as a function of the ratio of the diaphragm support forcing frequency to the undamped natural frequency of the diaphragm for various diaphragm thicknesses. In an ideal pressure receiver, acceleration of the support would have no effect on the output displacement; the corresponding curve in Fig. 7 would be a straight line along the frequency ratio axis. The actual curves of Fig. 7 show that the sensitivity ratio value of a flat-diaphragm pressure receiver increases as the diaphragm thickness (and, consequently, the diaphragm natural frequency) is made larger and changes toward higher sensitivity ratio values with increasing slope as the frequency ratio increases.

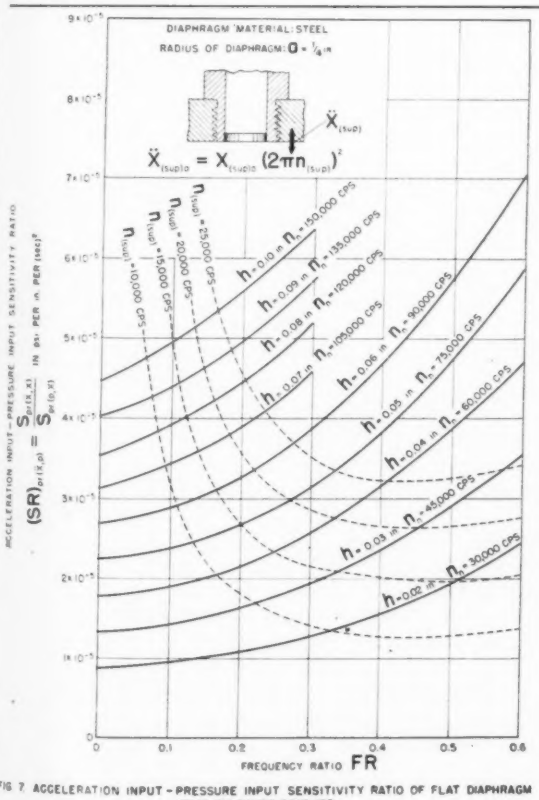
DIAPHRAGM MATERIAL: STEEL
RADIUS OF DIAPHRAGM: a = 1/4 in
$\ddot{X}_{(sup)} = X_{(sup)}(2\pi n_{(sup)})^2$
$\ddot{X}_{(sup)}$
$n_{(sup)}$ = 50,000 CPS
$n_{(sup)}$ = 100,000 CPS
$n_{(sup)}$ = 150,000 CPS
$n_{(sup)}$ = 200,000 CPS
$n_{(sup)}$ = 250,000 CPS
h = 0.10 in n_n = 150,000 CPS
h = 0.09 in n_n = 135,000 CPS
h = 0.08 in n_n = 120,000 CPS
h = 0.07 in n_n = 105,000 CPS
h = 0.06 in n_n = 90,000 CPS
h = 0.05 in n_n = 75,000 CPS
h = 0.04 in n_n = 60,000 CPS
h = 0.03 in n_n = 45,000 CPS
h = 0.02 in n_n = 30,000 CPS
ACCELERATION INPUT - PRESSURE INPUT SENSITIVITY RATIO
$(SR)_{pr(\ddot{x},p)} = \frac{S_{pr(\ddot{x},x)}}{S_{pr(p,x)}}$ IN psi PER in PER (sec)^2
FREQUENCY RATIO FR

FIG. 7. ACCELERATION INPUT - PRESSURE INPUT SENSITIVITY RATIO OF FLAT DIAPHRAGM TYPE PRESSURE RECEIVER.

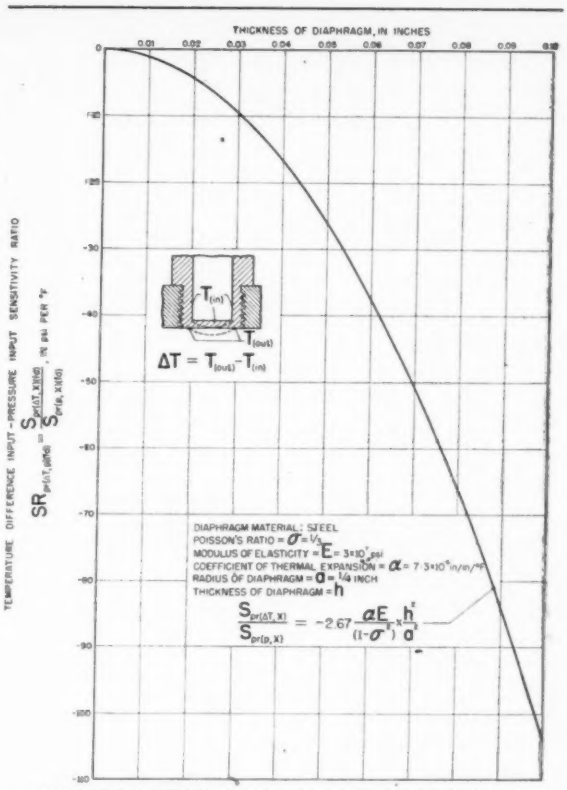
THICKNESS OF DIAPHRAGM, IN INCHES
TEMPERATURE DIFFERENCE INPUT - PRESSURE INPUT SENSITIVITY RATIO
$SR_{pr(\Delta T,p)} = S_{pr(\Delta T,X)}/S_{pr(p,X)}$, IN psi PER °F
$T_{(in)}$
$T_{(out)}$
$\Delta T = T_{(out)} - T_{(in)}$
DIAPHRAGM MATERIAL: STEEL
POISSON'S RATIO = $\sigma = 1/3$
MODULUS OF ELASTICITY = $E = 3\times10^7$ psi
COEFFICIENT OF THERMAL EXPANSION = $\alpha = 7.3\times10^{-6}$ in/in/°F
RADIUS OF DIAPHRAGM = a = 1/4 INCH
THICKNESS OF DIAPHRAGM = h
$\frac{S_{pr(\Delta T,X)}}{S_{pr(p,X)}} = -2.67\frac{\alpha E}{(1-\sigma^2)}\times\frac{h^2}{a^2}$

FIG. 8. TEMPERATURE DIFFERENCE INPUT - PRESSURE INPUT SENSITIVITY RATIO OF FLAT DIAPHRAGM TYPE PRESSURE RECEIVER AS A FUNCTION OF DIAPHRAGM THICKNESS

A requirement of the usual pressure-indicator design problem is that the undamped natural frequency of the pressure receiver must be as great as, or greater than, some lower limit depending upon a specified inaccuracy tolerance for the highest pressure oscillation frequency to be recorded. The curve family of Fig. 7 shows that a flat-diaphragm pressure receiver has the characteristic of a greater response to acceleration, in terms of pressure, as the diaphragm thickness is increased. It follows that, once a flat diaphragm has been made sufficiently thick to withstand the rigors of operating conditions and to have the minimum required undamped natural frequency, the undesirable effects of support acceleration will always be made worse with respect to the effective pressure-controlled output by increasing the diaphragm thickness. This means that the flat-diaphragm pressure receiver has a limitation so far as concerns the accurate recording of pressure fluctuations that have the same frequency as the imposed support vibration. When detonation occurs in an engine cylinder, the walls of the cylinder usually have vibratory acceleration frequencies equal to the existing detonation frequencies, so that records from a pressure indicator, using the flat diaphragm as its pressure receiver, will be subject to inaccuracies that are difficult to eliminate by compensation and practically impossible to remove effectively by corrections to the actual records.

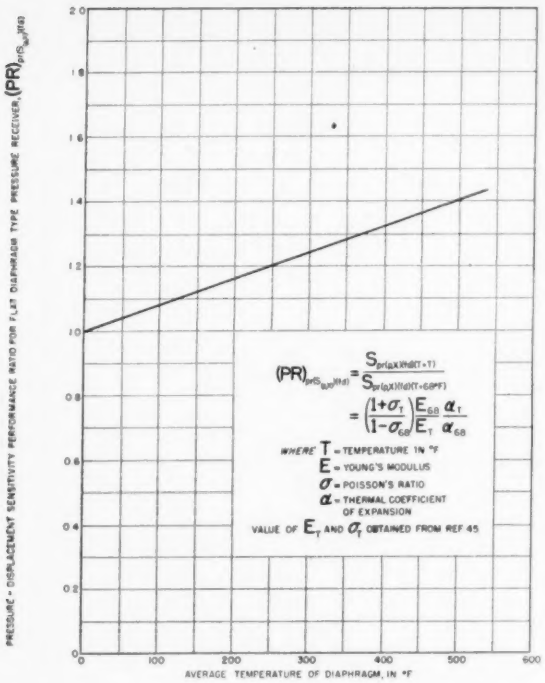

FIG. 9. EFFECT OF AVERAGE TEMPERATURE ON PRESSURE-DISPLACEMENT SENSITIVITY OF FLAT DIAPHRAGM TYPE PRESSURE RECEIVER.

Effect of Temperature Gradient in the Material of a Flat-Diaphragm Pressure Receiver

The theoretical curve of Fig. 8 is practically equivalent to a curve of temperature difference - pressure sensitivity ratio for a flat - diaphragm pressure receiver as a function of the diaphragm thickness. For convenience in presentation, the reference quantity is taken as the temperature difference between the outer and inner surfaces of the diaphragm, instead of the temperature gradient itself. The curve shows that the temperature difference - pressure sensitivity ratio is generally negative. This means that a positive temperature difference (the outer-surface temperature being taken as the reference temperature) produces the same effect as a reduction of the input pressure. Physically, the action is caused by the greater thermal expansion of diaphragm layers near the hotter surface—that is, when the outer surface is hotter than the inner surface, the diaphragm tends to bow outward and produces the same effect as a reduction in the applied pressure. This effect is considerable, as illustrated by the fact that, with a diaphragm of 0.030-in. thickness, a 1°F. temperature difference produces the same effect as a pressure change of about 10 lbs. per sq.in. In practice, the temperature gradient in a pressure receiver exposed to the operating pressures of an engine cylinder will change considerably as engine conditions are changed. As a consequence, the effective zero reference level on the record from a flat - diaphragm type pressure receiver varies in a way that usually introduces inaccuracies of considerable size in the corresponding engine pressure records.

In addition to the temperature gradient effect due to a change in engine conditions, there is a more serious effect caused by the change in temperature that occurs within a single cycle. Because the cyclic temperature effect and the pressure input are of the same fundamental frequency, there is no way to distinguish one from the other in the output signal of the pressure receiver.

Effect of Average Temperature on the Performance of Flat-Diaphragm Pressure Receivers

Fig. 9 gives a plot of the *pressure - displacement sensitivity performance ratio* for a flat diaphragm pressure receiver as a function of the average diaphragm temperature. The performance ratio plot shows that the pressure - displacement sensitivity increases as the average diaphragm temperature becomes greater. This change corresponds to the physical action that causes a weakening of the diaphragm material as its average temperature increases. The effect represented in Fig. 9 does not cause a change in the zero reference level of a pressure receiver, but, on the other hand, it introduces an inaccuracy in the interpretation of pressure records if the average diaphragm temperature is either at a constant unknown level or fluctuates in an unknown way. In engine installations, the average diaphragm temperature has been known to vary several hundred degrees Fahrenheit;[3] this effect can introduce inaccuracies of several per cent in engine-pressure records.

Performance Defects of a Flat-Diaphragm Pressure Receiver[1-4]

Specifications for the operating components of any measuring system can be written only after acceptable inaccuracy tolerances have been established for indications from the system. In the case of pressure indicators, it appears reasonable to establish an inaccuracy tolerance equal to 1 per cent of the designed maximum pressure indication. Even though no inaccuracy component is allowed for the coupling and indicating systems, the preceding discussion of the flat diaphragm shows that pressure receivers of this type have performance characteristics that may produce inaccuracy components larger than the specified tolerance. For example, when a steel diaphragm of $^1/_2$-in. diameter and 0.050-in. thickness is assumed for the pressure receiver of an indi-

TABLE 1

Tolerance on Environmental Effects Equivalent to Pressure Effects of 10 Lbs. per Sq. In. on Flat Steel Diaphragm 0.050 In. Thick and 0.500 In. in Diameter

Support Vibration Amplitude at 10,000 Cycles per Sec.; (Based on Curve of Fig. 7) (In.)	Temperature Difference Through Diaphragm; (Based on Curve of Fig. 8) (°F.)	Difference in Average Temperature When Applied Pressure is 500 Lbs. per Sq. In. (Based on Curve of Fig. 9) (°F.)
1.04×10^{-4}	0.37	25

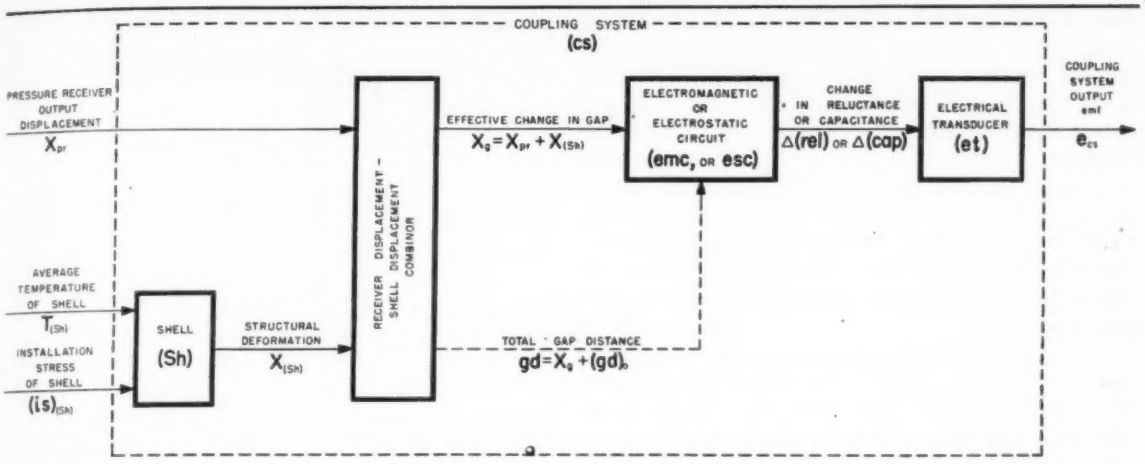

FIG. 10. FUNCTIONAL DIAGRAM OF DISPLACEMENT RECEIVER FOR ELECTRICAL COUPLING SYSTEM.

cator designed to measure a maximum pressure of 1,000 lbs. per sq. in., Table 1 gives the allowable levels of vibratory acceleration, temperature difference across the diaphragm, and average temperature change to produce an output deflection change equivalent to a pressure variation of 10 lbs. per sq.in. (i.e., 1 per cent of 1,000 lbs. per sq.in.).

Available data on cylinder head vibration[4] show that amplitudes of 0.0002–0.0005 in. occur at frequencies above 10,000 cycles per sec. This means that the flat steel diaphragm does not have a sufficiently low acceleration - pressure sensitivity ratio to serve as the pressure receiver of a satisfactory engine indicator.

Accurate information is not available on the temperature differences through steel diaphragms exposed to engine pressure, but it is reasonable to expect differences up to 100°F. under operation conditions.[3] Reference to Table 1 shows that the effect of a temperature difference through the diaphragm can cause a pressure inaccuracy that exceeds by a considerable margin, the allowable limit of 10 lbs. per sq.in.

The average temperature of a flat steel diaphragm may change from about 70° to about 300°F. with different operating conditions. The corresponding variation in the output deflection of a flat diaphragm pressure receiver for an applied pressure of 500 lbs. per sq.in. exceeds the specified tolerance limit of Table 1 by ten times.

Performance Limiting Characteristics of a Flat Diaphragm Pressure Receiver Electrical Displacement Detecting Coupling System

The combination of a flat diaphragm pressure receiver and an electrical deflection detecting coupling system, as shown in Fig. 4, is most commonly adopted in indicator design because of the simplicity and ruggedness of the system and the good performance in low-frequency applications.[2, 5, 6] However, performance limiting characteristics, in addition to those already described for the flat diaphragm as a pressure receiver, are introduced by the use of the electrical displacement detecting coupling system in which the flat diaphragm serves also as an element of the electrical system.

An electrical displacement detecting coupling system of either the electromagnetic or the electrostatic type receives as the input signal the diaphragm displacement, which controls the reluctance or capacitance across an air gap between the diaphragm and a "fixed" pole or electrode, and thereby produces an electrical signal that is amplified as the output signal of the coupling system. As shown in Fig. 4, the flat diaphragm pressure receiver and the fixed pole or electrode are linked together by the outer shell of the indicator, and a diaphragm deflection is realized as an effective change in gap only through the bridging of the structure of the shell. The functional diagram of the essential operating characteristics of the deflection detecting coupling system is shown in Fig. 10. Under static conditions, the effective change in gap between the two electrodes (one of which is the flat diaphragm) are affected by three input quantities: (1) deflection of the diaphragm as a pressure receiver; (2) deformation of the shell caused by temperature change; and (3) deformation of the shell caused by externally applied stresses due to mounting effects.

The second and third of the foregoing inputs are undesired; their existence produces a shift in the datum line of the pressure record. In actual test of a typical design, the zero pressure datum line shift of the pressure record due to each of the two effects may, under ordinary operating conditions, exceed the record reading corresponding to the maximum allowable pressure of the diaphragm.

In Fig. 10, the effective change in gap is shown as the controlling input of an electromagnetic or an electrostatic circuit, the output of which is a change in induct-

ance or capacitance. Under ideal conditions, the *gap change input - reluctance (or capacitance) change output sensitivity* of the circuit should be a constant. However, as an inherent characteristic of the circuit, the *gap change input - reluctance (or capacitance) change output sensitivity* is modified by the absolute value of the total gap. Consequently, the diaphragm deflection will not only provide an input signal to the electromagnetic (or electrostatic) circuit but will also impose a modification upon the sensitivity of the circuit through the change in the total gap. A nonlinear sensitivity is therefore an inevitable result.

By a similar reasoning, the temperature and installation-strain effects applied to the shell of the indicator will not only produce a shift of the zero pressure datum line in the record but will also cause the *gap change input - reluctance change output sensitivity* to undergo a substantial alteration. Actual tests of a *flat diaphragm - electrical displacement detecting type indicator* show a deviation from unity of as much as 10 per cent in the sensitivity ratio because of temperature and installation strain effects.

The foregoing discussion shows that the flat diaphragm does not have characteristics that permit it to be satisfactory as the receiver of a pressure indicator. When flat-diaphragm performance is used as the standard of comparison, it appears that a suitable pressure receiver must have a reduced sensitivity to acceleration and temperature, in addition to having a *pressure - displacement sensitivity* that is less affected by average temperature. The essential features of a pressure receiver substantially free from the performance defects of the flat diaphragm are described in the following section.

(IV) The Catenary Diaphragm-Strain Generating Tube Combination Performance Characteristics for Pressure Receivers

Desired Features of a Satisfactory Pressure Receiver

The problem of producing a pressure receiver with sufficient mechanical strength and temperature resistance to reliably withstand engine operating conditions can be solved by separating the pressure seal from the member that is designed to provide elastic reaction to balance the force output of the pressure seal. This feature makes it possible to design the pressure seal to be so weak as an elastic member and so small in effective mass that temperature and acceleration effects do not appreciably change the resultant output of the pressure receiver. The member required to complement the elastically weak pressure seal must be strong from the standpoint of elastic deformations and must have a high natural frequency even when loaded by the mass of the pressure seal. In addition, it is desirable for the quantity chosen as the pressure receiver output to be generated in a way that will make it possible to incorporate acceleration- and temperature-compensating features in the design for the system.

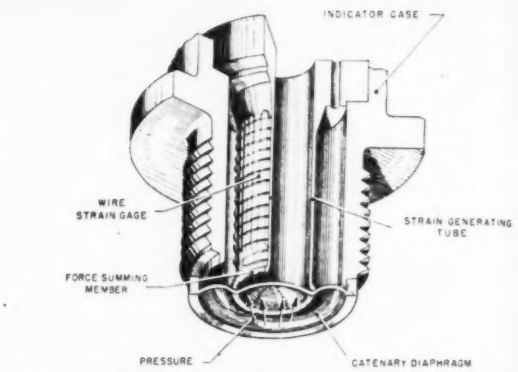

FIG. 11. PICTORIAL SCHEMATIC DIAGRAM OF CATENARY DIAPHRAGM - STRAIN GENERATING TUBE COMBINATION PRESSURE RECEIVER WITH WIRE STRAIN GAGE WINDING AS RECEIVER FOR ELECTRICAL COUPLING SYSTEM.

The desired condition of a weak pressure seal is partially fulfilled in the design of the carbon-resistor-type indicator[6] or a piezoelastic-type indicator.[5,9] In each, a relatively thin flat diaphragm is used as the pressure seal, and the major elastic restraint of the indicator is supplied by a member not in direct contact with the hot gas. Indicators of this type may have better performance than those which have unsupported flat diaphragms. However, with the pressure seal diaphragm only partially supported, temperature and mounting strain still have important effects on the performance of the indicator.

Essential Features of a Catenary-Type Diaphragm

Fig. 11 is a pictorial schematic diagram showing the essential features of a pressure receiver made up of a catenary-type diaphragm, which bears lightly against a force summing member that has the form of a rounded circular ring on the unsupported end of a thin tube rigidly attached to the case of the unit. The catenary diaphragm is designed to be strong enough, as a pressure seal, to support the input pressure and, at the same time, to be so weak flexurally that any deflection occurring in practice will not cause an elastic force of appreciable magnitude to be applied to the force summing member. Under static conditions, the pressure seal transforms the input pressure into a force, applied to the force summing member, which is substantially balanced by a reaction force generated by strains in the strain generating tube.

Structurally, a three-dimensional *catenary diaphragm and strain generating tube system* is closely analogous to a (two-dimensional) suspension bridge with catenary-shaped cables. A similar analogy links a flat diaphragm to a solid beam. A suspension bridge is known to be structurally more efficient than a solid beam bridge;

similarly, a catenary diaphragm - strain generating tube combination is more efficient in its structural design than a flat diaphragm. To its credit, a smaller effective mass is added to the catenary diaphragm - strain generating tube system than is added in a flat diaphragm of equal elastic properties. As a consequence, the inertia force experienced by the moving parts of the pressure receiver during a dynamic response is less with a catenary diaphragm - strain generating tube system than with a flat diaphragm.

Fig. 12 gives a line schematic diagram, a functional diagram, and a summary of static performance characteristics for the catenary diaphragm - strain generating tube pressure receiver of Fig. 11. The essential output of the pressure receiver is the resultant surface strain of the strain generating tube. Sensitivities for which pressure, acceleration, and temperature gradient through the catenary diaphragm are the respective actuating inputs and resultant surface strain of the strain generating tube is the output are summarized in Fig. 12.

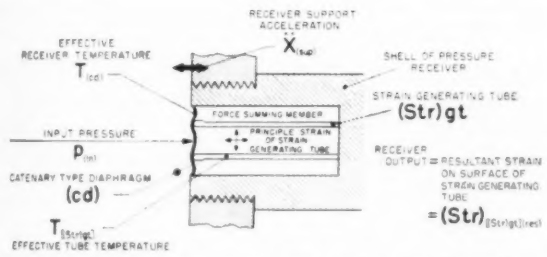

a SCHEMATIC DIAGRAM SHOWING ESSENTIAL FEATURES OF CATENARY DIAPHRAGM - STRAIN GENERATING TUBE TYPE PRESSURE RECEIVER

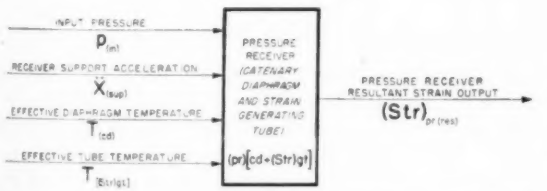

b FUNCTIONAL DIAGRAM OF CATENARY DIAPHRAGM - STRAIN GENERATING TUBE TYPE PRESSURE RECEIVER

$S_{pr(p,Str)[cd+(Str)gt]} = \frac{\partial (Str)_{(pr)}}{\partial p_{(in)}}$ = PRESSURE - STRAIN SENSITIVITY OF PRESSURE RECEIVER

$S_{pr(\ddot{X},Str)[cd+(Str)gt]} = \frac{\partial (Str)_{(pr)}}{\partial \ddot{X}_{(sup)}}$ = ACCELERATION - STRAIN SENSITIVITY OF PRESSURE RECEIVER

$S_{pr(T_{[(Str)gt]},Str)[cd+(Str)gt]} = \frac{\partial (Str)_{(pr)}}{\partial T_{(Str)}}$ = TEMPERATURE OF TUBE - STRAIN SENSITIVITY OF PRESSURE RECEIVER

$(SR)_{pr(\ddot{X},p)[cd+(Str)gt]} = \frac{S_{pr(\ddot{X},Str)}}{S_{pr(p,Str)}}$ = ACCELERATION INPUT - PRESSURE INPUT SENSITIVITY RATIO OF PRESSURE RECEIVER

$(SR)_{pr(T_{[(Str)gt]},p)[cd+(Str)gt]} = \frac{S_{pr(T_{(cd)},Str)}}{S_{pr(p,Str)}}$ = TEMPERATURE INPUT - PRESSURE INPUT SENSITIVITY RATIO OF PRESSURE RECEIVER

c STATIC PERFORMANCE CHARACTERISTICS OF CATENARY DIAPHRAGM - STRAIN GENERATING TUBE TYPE PRESSURE RECEIVER.

FIG 12. SCHEMATIC DIAGRAM, FUNCTIONAL DIAGRAM AND STATIC PERFORMANCE CHARACTERISTICS OF CATENARY DIAPHRAGM - STRAIN GENERATING TUBE TYPE PRESSURE RECEIVER.

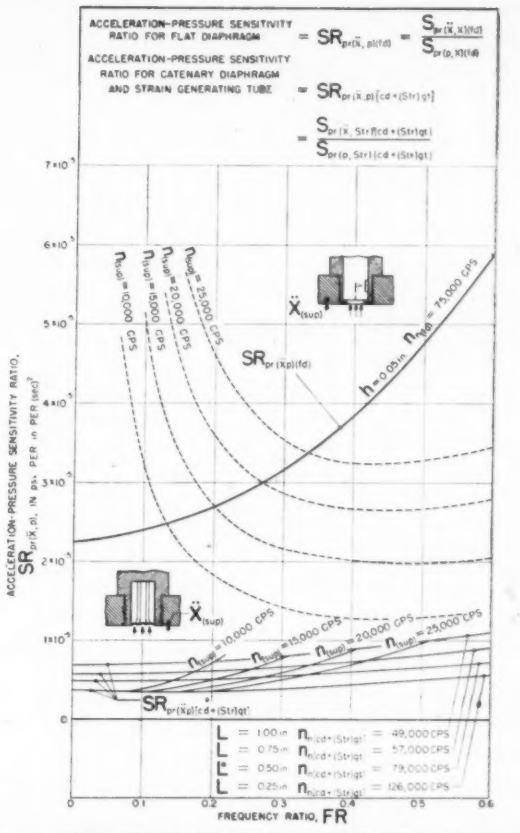
ACCELERATION-PRESSURE SENSITIVITY RATIO FOR FLAT DIAPHRAGM
$= SR_{pr(\ddot{X},p)(fd)} = \frac{S_{pr(\ddot{X},X)(fd)}}{S_{pr(p,X)(fd)}}$
ACCELERATION-PRESSURE SENSITIVITY RATIO FOR CATENARY DIAPHRAGM AND STRAIN GENERATING TUBE
$= SR_{pr(\ddot{X},p)[cd+(Str)gt]}$
$= \frac{S_{pr(\ddot{X},Str)[cd+(Str)gt]}}{S_{pr(p,Str)[cd+(Str)gt]}}$
ACCELERATION-PRESSURE SENSITIVITY RATIO, $SR_{pr(\ddot{X},p)}$, IN psi PER in PER (sec)^2
$n_{(sup)} = 10,000$ CPS
$n_{(sup)} = 15,000$ CPS
$n_{(sup)} = 20,000$ CPS
$n_{(sup)} = 25,000$ CPS
$n_{fd} = 75,000$ CPS
$SR_{pr(\ddot{X}p)(fd)}$
$h = 0.05$ in
$\ddot{X}_{(sup)}$
$SR_{pr(\ddot{X}p)[cd+(Str)gt]}$
L = 1.00 in $n_{n[cd+(Str)gt]} = 49,000$ CPS
L = 0.75 in $n_{n[cd+(Str)gt]} = 57,000$ CPS
L = 0.50 in $n_{n[cd+(Str)gt]} = 73,000$ CPS
L = 0.25 in $n_{n[cd+(Str)gt]} = 126,000$ CPS
FREQUENCY RATIO, FR

FIG 13. ACCELERATION-PRESSURE SENSITIVITY RATIO OF FLAT DIAPHRAGM TYPE PRESSURE RECEIVER COMPARED WITH SENSITIVITY RATIO OF CATENARY DIAPHRAGM AND STRAIN TUBE TYPE PRESSURE RECEIVER.

Improvement in Acceleration - Pressure Sensitivity Ratio

The improvement in reduced sensitivity to the support acceleration, which is realized by using the catenary diaphragm - strain generating tube combination instead of the flat diaphragm to carry out the functions of a pressure receiver, is shown by the curve family of Fig. 13. These curves, which are drawn for various lengths of the strain generating tube, are similar to the curves of Fig. 7 for the flat-diaphragm pressure receiver. Typical flat-diaphragm curves from Fig. 7 are included in Fig. 13 for comparison purposes. It appears that the acceleration - pressure sensitivity ratio for a catenary diaphragm - strain generating tube combination is considerably smaller than the acceleration - pressure sensitivity ratio for the flat diaphragm. For a given thickness of a flat diaphragm and a given length of a strain generating tube to give comparable natural frequencies (for example, 0.050-in. thickness and 0.500-in. tube length), the relative reduction in acceleration response becomes greater as the frequency ratio (i.e., the forced frequency of the support vibration) increases. A second advantage of the catenary diaphragm - strain generating tube combination is that the acceleration - pressure sensitivity ratio for a given forcing frequency decreases as the natural frequency of the combination is increased. The

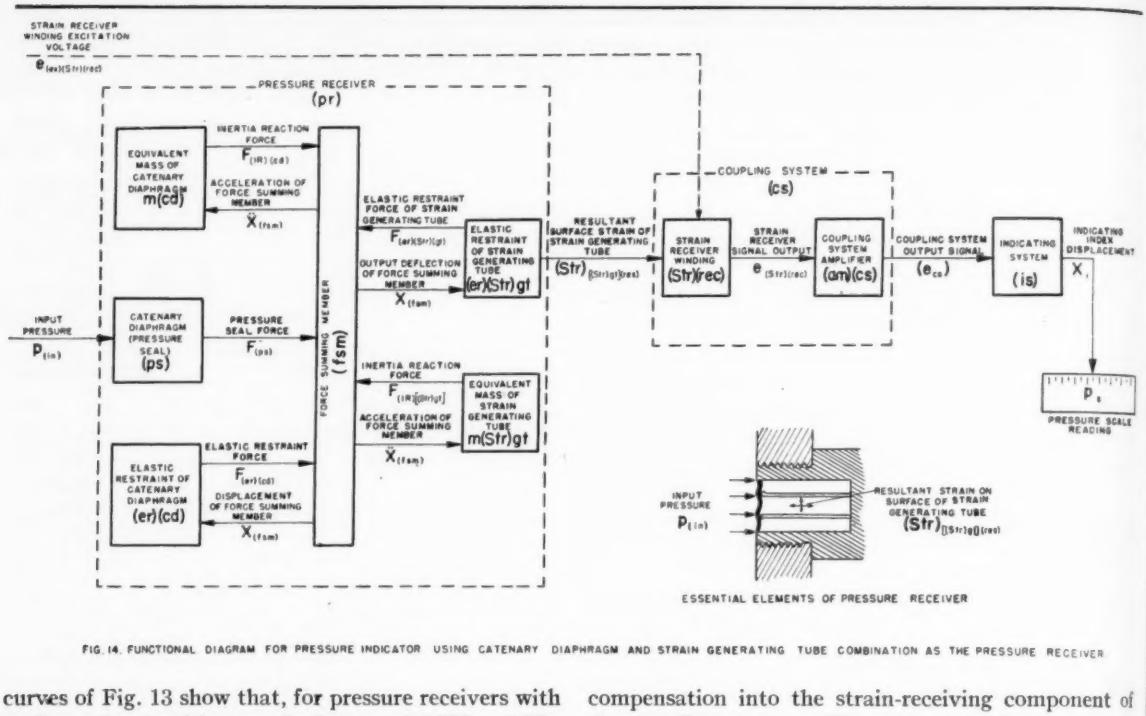
STRAIN RECEIVER WINDING EXCITATION VOLTAGE
PRESSURE RECEIVER (pr)
EQUIVALENT MASS OF CATENARY DIAPHRAGM m(cd)
INERTIA REACTION FORCE
ACCELERATION OF FORCE SUMMING MEMBER
INPUT PRESSURE
CATENARY DIAPHRAGM (PRESSURE SEAL) (ps)
PRESSURE SEAL FORCE
FORCE SUMMING MEMBER (fsm)
ELASTIC RESTRAINT OF CATENARY DIAPHRAGM (er)(cd)
ELASTIC RESTRAINT FORCE
DISPLACEMENT OF FORCE SUMMING MEMBER
ELASTIC RESTRAINT FORCE OF STRAIN GENERATING TUBE
OUTPUT DEFLECTION OF FORCE SUMMING MEMBER
ELASTIC RESTRAINT OF STRAIN GENERATING TUBE (er)(Str)gt
INERTIA REACTION FORCE
ACCELERATION OF FORCE SUMMING MEMBER
EQUIVALENT MASS OF STRAIN GENERATING TUBE m(Str)gt
RESULTANT SURFACE STRAIN OF STRAIN GENERATING TUBE
COUPLING SYSTEM (cs)
STRAIN RECEIVER WINDING (Str)(rec)
STRAIN RECEIVER SIGNAL OUTPUT
COUPLING SYSTEM AMPLIFIER (am)(cs)
COUPLING SYSTEM OUTPUT SIGNAL
INDICATING SYSTEM (is)
INDICATING INDEX DISPLACEMENT
PRESSURE SCALE READING
INPUT PRESSURE
RESULTANT STRAIN ON SURFACE OF STRAIN GENERATING TUBE
ESSENTIAL ELEMENTS OF PRESSURE RECEIVER

FIG. 14. FUNCTIONAL DIAGRAM FOR PRESSURE INDICATOR USING CATENARY DIAPHRAGM AND STRAIN GENERATING TUBE COMBINATION AS THE PRESSURE RECEIVER

curves of Fig. 13 show that, for pressure receivers with undamped natural frequencies between 75,000 and 80,000 cycles per sec. that are subjected to forcing frequencies near 10,000 cycles per sec. (this is in the frequency range of cylinder wall vibration of practical engines), the equal support acceleration amplitudes will produce from the catenary diaphragm unit an output strain component of only about one-fifth of the pressure equivalent output that would be caused by the same vibratory acceleration applied to a flat-diaphragm unit.

Improvement in Effect of Temperature on Pressure-Strain Sensitivity

From the standpoint of theory, temperature gradients in a sufficiently flexible catenary diaphragm will cause forces of negligible magnitudes on the force summing member in comparison with the force output of the pressure seal. Any catenary diaphragm - strain generating tube combination for which this is true will show no change in its pressure - strain sensitivity as the average diaphragm temperature is changed, because a variation in an already negligible quantity (the flexural stiffness of the diaphragm) cannot have an appreciable effect on the output. Similarly, a deformation in the outer shell of the indicator produced by a change in its temperature or by a change in the mounting stress will have a negligible effect upon the axial loading of the strain-generating tube, because the catenary diaphragm is substantially flexible. For these reasons, a properly designed catenary diaphragm - strain generating tube combination pressure receiver is theoretically free from temperature and installation strain effects. The realization of this ideal performance in an actual pressure receiver depends upon the design of proper temperature compensation into the strain-receiving component of the coupling system. The strain-receiving means actually used and its performance as a component of a complete pressure indicating system are discussed in the remaining sections.

(V) Complete Pressure Indicator Using Catenary Diaphragm - Strain Generating Tube Combination Pressure Receiver

Functional Description of Complete Pressure Indicator

Fig. 14 gives the functional diagram for a complete pressure indicator that is based on the catenary diaphragm pressure receiver. The features of the pressure receiver have already been discussed. In effect, this operating component receives the input pressure and produces surface strain of the strain generating tube as its output. The strain receiver for the coupling system is a temperature-compensating wire strain gage winding.[7,32–34] The output of this strain gage is received by the coupling system amplifier, which produces the coupling system signal as its output. The indicating system receives the coupling system output signal as its input and produces the indicating system index deflection as its output. The pressure scale, which may be attached to the indicating system or may be applied separately to individual records, has the function of showing the correspondence between indicating index displacement and measured pressure levels.

Coupling System

The function of the coupling system is to receive the strain signal output of the pressure receiver and to pro-

duce as its output an electrical signal suitable for use as an input by the indicating system. To be satisfactory, the coupling system output must be a linear function of the strain input without being affected by pressure receiver temperature or accelerations. This result is accomplished by using an electrical winding, with two arms of equal resistance, attached in a lattice form to the outside of the strain generating tube by a special temperature-resisting cement. As shown in the diagram of Fig. 15, one section of the twin-arm winding is applied with the wire cemented parallel to the longitudinal axis of the strain generating tube and running from end to end of the tube in loops equally spaced around its circumference. The other winding section is applied as a double spiral around the circumference of the tube in a bifilar arrangement to minimize the inductance effect.

In an electrical circuit these two windings are connected in series, with a known voltage applied across them. The potential change at the common lead of the two windings is used as the output signal of the strain receiver. When an axial load is applied to the strain generating tube, the longitudinal winding is subjected to a reduction in electrical resistance because of compressive strain; at the same time, the cross-wound coil experiences an increase in resistance because of tensile strain. These effects are additive and cause a change in potential at the center tap of the series winding which establishes an output signal corresponding to the input pressure applied to the diaphragm.

Because both windings of the strain receiver are intimately bound to the strain generating tube, they closely follow temperature changes in the tube and receive similar resistance changes due to a change in the temperature of the tube and wire. As a result, no potential change will occur at the output terminal (i.e., the common lead of the two strain receiver windings) because of temperature effect.

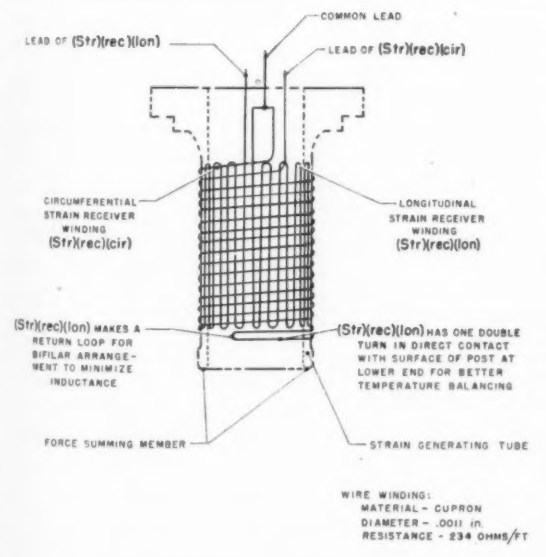
COMMON LEAD
LEAD OF (Str)(rec)(lon)
LEAD OF (Str)(rec)(cir)
CIRCUMFERENTIAL STRAIN RECEIVER WINDING (Str)(rec)(cir)
LONGITUDINAL STRAIN RECEIVER WINDING (Str)(rec)(lon)
(Str)(rec)(lon) MAKES A RETURN LOOP FOR BIFILAR ARRANGEMENT TO MINIMIZE INDUCTANCE
(Str)(rec)(lon) HAS ONE DOUBLE TURN IN DIRECT CONTACT WITH SURFACE OF POST AT LOWER END FOR BETTER TEMPERATURE BALANCING
FORCE SUMMING MEMBER
STRAIN GENERATING TUBE
WIRE WINDING:
MATERIAL - CUPRON
DIAMETER - .0011 in.
RESISTANCE - 234 OHMS/FT

FIG. 15 DIAGRAM SHOWING THE ARRANGEMENT OF WIRE WINDING FOR STRAIN RECEIVER OF COUPLING SYSTEM.

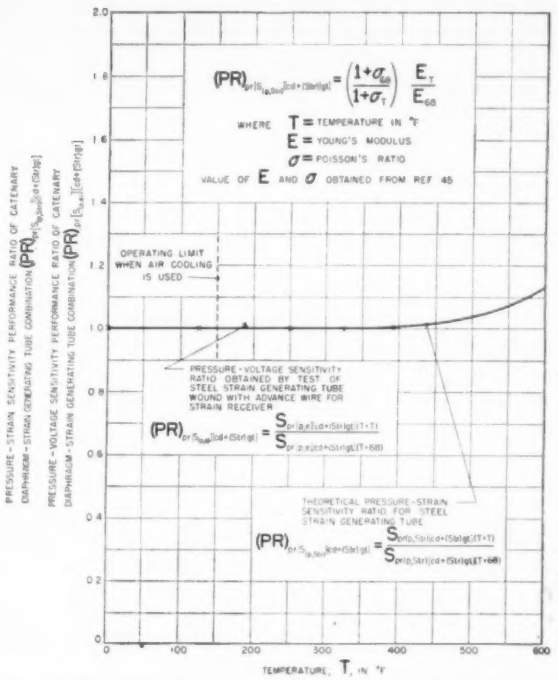
WHERE T = TEMPERATURE IN °F
E = YOUNG'S MODULUS
σ = POISSON'S RATIO
VALUE OF E AND σ OBTAINED FROM REF 45
OPERATING LIMIT WHEN AIR COOLING IS USED
PRESSURE-VOLTAGE SENSITIVITY RATIO OBTAINED BY TEST OF STEEL STRAIN GENERATING TUBE WOUND WITH ADVANCE WIRE FOR STRAIN RECEIVER
THEORETICAL PRESSURE-STRAIN SENSITIVITY RATIO FOR STEEL STRAIN GENERATING TUBE
PRESSURE-STRAIN SENSITIVITY PERFORMANCE RATIO OF CATENARY DIAPHRAGM-STRAIN GENERATING TUBE COMBINATION
PRESSURE-VOLTAGE SENSITIVITY PERFORMANCE RATIO OF CATENARY DIAPHRAGM-STRAIN GENERATING TUBE COMBINATION
TEMPERATURE, T, IN °F

FIG 16. EFFECT OF TEMPERATURE ON PRESSURE-VOLTAGE SENSITIVITY PERFORMANCE RATIO OF CATENARY DIAPHRAGM PRESSURE RECEIVER

In addition to this, the *pressure input-resultant strain output sensitivity* holds a constant value, despite changes in the temperature of the strain generating tube, because of the compensation effect between the change in the modulus of elasticity and the change in Poisson's ratio of the strain generating tube. With only the longitudinal strain as the output signal, the pressure-strain sensitivity value at higher temperature would be larger than at lower temperature because of a change in the modulus of elasticity. However, the circumferential strain experiences an opposite effect because of the change in Poisson's ratio. The two effects just about balance each other, and, as a result, the sensitivity performance ratio is nearly independent of temperature, as shown in Fig. 16.

Fig. 17 shows the internal electrical connections of the coupling system that receives resistance changes from the strain receiver and produces electrical signals suitable for operating the indicating system. The electrical system consists of a voltage supply applied across the longitudinal and circumferential strain receiver windings connected in series. The electrical output of the strain receiver system, taken from the common lead of the receiver, is applied as the input to the coupling system amplifier. The output from this amplifier is the coupling system output that acts as the input signal to the indicating system.

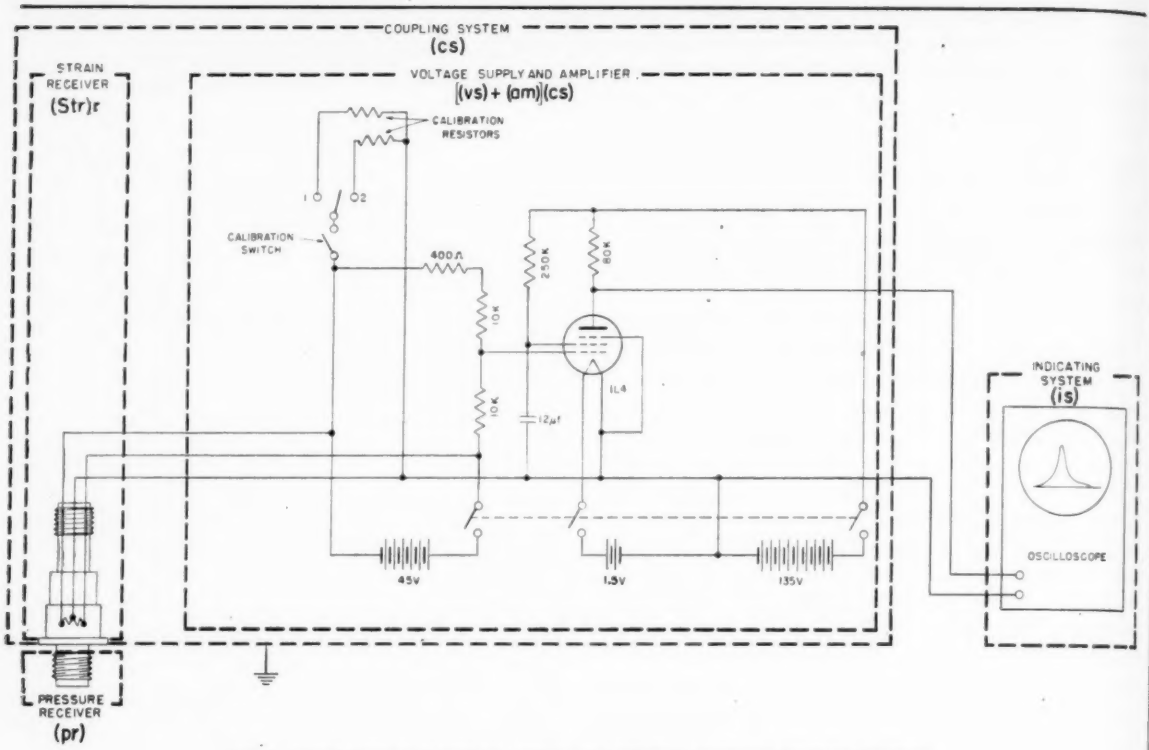

FIG. 17. CIRCUIT DIAGRAM OF COUPLING SYSTEM FOR CATENARY DIAPHRAGM PRESSURE RECEIVER

FIG. 18. PHOTOGRAPH SHOWING PARTS OF COUPLING SYSTEM EXTERNAL TO PRESSURE RECEIVER UNIT AND CATHODE RAY OSCILLOSCOPE AS INDICATING SYSTEM

Fig. 18 is a photograph showing a cathode-ray oscilloscope, which is used as the indicating system, and the box containing coupling system parts that are outside the pressure receiver unit.

Mechanical Features of Pressure Receiver Unit

The upper part of the photograph of Fig. 19 shows the external appearance of a complete catenary diaphragm-strain generating tube pressure receiver unit; the lower part shows the four component parts of the pressure receiver unit. Figs. 20 and 21 give cross-sectional diagrams showing the operating relationships among internal parts of the pressure receiver unit. Corresponding parts are given the same labels in Figs. 19, 20, and 21. The catenary diaphragm is formed as a separate unit and is attached to the shell by means of a forcing fit on a silver solder joint. The shell carries an outside thread to fit into an 18-mm. spark plug hole, a locating shoulder to locate the cooling air guide tube, and an internal thread to receive the connector sleeve that serves to hold the component parts of the unit together. The cooling-air guide tube has a flange that fits against the locating shoulder. When the assembly is complete, the cooling-air guide tube forces air, supplied under pressure, through the connector sleeve to flow partly along the length of the strain generating tube and partly outward across the catenary diaphragm through cooling-air passage holes in the strain generating tube before leaving to the atmosphere through the cooling-air

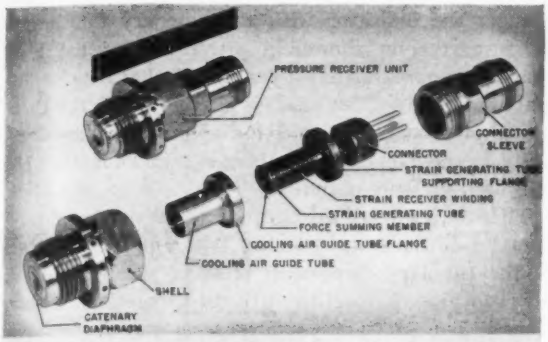

FIG. 19 PHOTOGRAPH SHOWING COMPLETE CATENARY DIAPHRAGM PRESSURE RECEIVER UNIT AND COMPONENT PARTS.

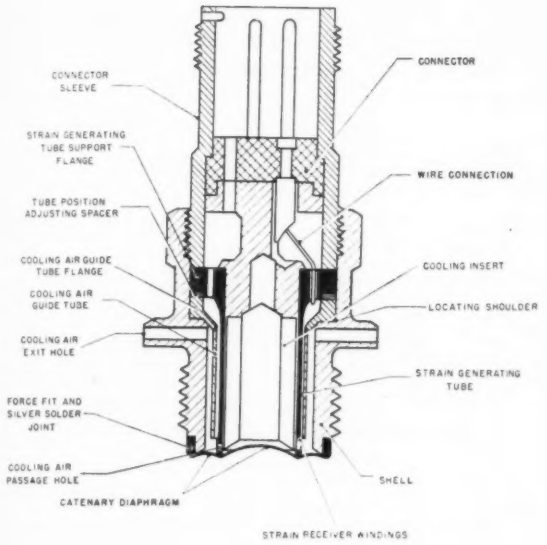

FIG. 20. CROSS SECTION OF CATENARY DIAPHRAGM PRESSURE RECEIVER UNIT.

exit holes in the shell. The path of this air circulation is shown in Fig. 21. The strain generating tube support fits into the shell on top of the cooling-air guide tube flange. A tube position adjusting spacer is used to locate the strain generating tube support flange so that the rounded end of the strain generating tube, which acts as the force summing member, is brought into proper contact with the catenary diaphragm. In practice, the tube is located so that the diaphragm is deflected from its equilibrium position by approximately 0.002 in. The strain receiver winding is cemented to the outside of the strain generating tube with the arrangement shown in Fig. 15. Wire connections attach the ends and the midpoint of the strain receiver winding to a three-prong connector, which is held in place by a shoulder in the connector sleeve when this sleeve is screwed into the shell. The complete pressure receiver unit is approximately 2 in. long and will fit into holes designed for 18-mm. spark plugs.

(VI) Performance Realized by an Indicator with Catenary Diaphragm Pressure Receiver Unit

Sensitivity of the Pressure Receiver Unit

An indicator of the type described in Figs. 19 and 20 can be operated to receive pressure as its actuating input and constant voltage as its modifying input and to produce voltage as its essential output. Calibration data taken on a number of catenary diaphragm indicators designed to operate under 1,000 lbs. per sq.in. have shown that the realized *modified voltage input, pressure input - voltage output sensitivity* is about 0.001 millivolt per lb. per sq.in. Over the designed operating range of 10 lbs. per sq.in. below atmospheric pressure to 1,000 lbs. per sq.in. above atmospheric pressure, the deviation of this sensitivity from its specified value is always less than 1 per cent.

Comparison of Catenary Diaphragm Unit with Flat-Diaphragm Unit

The operating characteristics achieved by the use of the pressure receiver design features described in Figs. 19 and 20, as compared with the results from a flat-diaphragm pressure receiver, were measured by taking records from units of the two types under identical conditions. The flat-diaphragm unit used for comparison purposes was a capacitance-type indicator developed by General Motors Research Corporation.[2] This unit, which represents the best available equipment of its type, is referred to as the flat-diaphragm pressure receiver in the figures that follow.

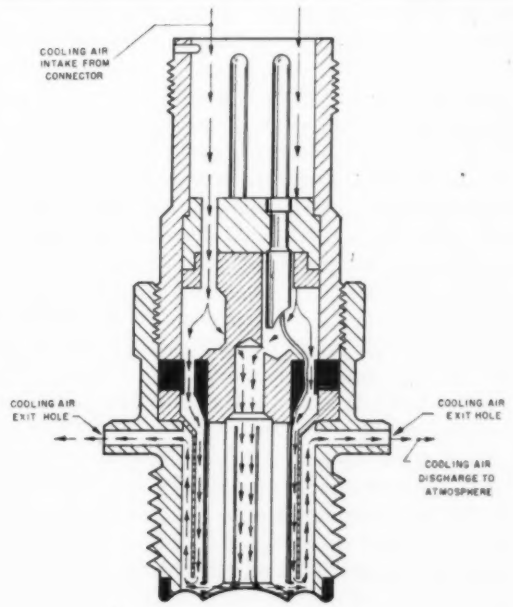

FIG. 21 CROSS SECTION OF CATENARY DIAPHRAGM PRESSURE RECEIVER UNIT SHOWING PATH OF COOLING AIR.

C. VIBRATION RESPONSE OF PRESSURE INDICATOR WITH FLAT DIAPHRAGM PRESSURE RECEIVER.

D. VIBRATION RESPONSE OF PRESSURE INDICATOR WITH CATENARY DIAPHRAGM PRESSURE RECEIVER.

FIG. 22 COMPARISON OF VIBRATION RESPONSE OF CATENARY DIAPHRAGM PRESSURE RECEIVER WITH VIBRATION RESPONSE OF FLAT DIAPHRAGM PRESSURE RECEIVER.

Acceleration sensitivity effects were tested by subjecting the support carrying the comparison pressure receiver units to shocks produced by hammer blows. Oscillograph records from the comparison units, obtained with shocks of this kind, are shown in Fig. 22. The upper record in the figure is from the indicator using the flat-diaphragm indicator; the lower record is from the catenary diaphragm unit indicator. These records show that the response of the catenary diaphragm unit is about one-fifth as much as the response of the flat diaphragm unit. This result is in accord with theoretical predictions based on the sensitivity ratio curves of Fig. 13.

The effect of temperature gradient through the diaphragm material was demonstrated by subjecting the pressure receivers of the comparison indicators to the same fluctuation in temperature by repeatedly covering and uncovering a gas flame playing on the pressure seals. The curves of Fig. 23 show that the effect of a rapidly changing temperature on the catenary diaphragm is less than one-twentieth as much as the effect of the same temperature change on the flat diaphragm. This performance improvement is substantial but is less than that predicted from theory for a perfectly flexible pressure seal diaphragm. The difference is due to the deviation of the actual catenary diaphragm and strain generating tube system from an ideal system.

The effect of average temperature gradient in changing the zero reference level in terms of indicated pressure is shown in the curves of Fig. 24. It appears from these curves that, for the indicator with the flat diaphragm pressure receiver (with water cooling), the zero reference point for the pressure indications shifted by an amount almost equal to the full-scale reading when the temperature of the support was changed approximately 200°F. On the other hand, under the same temperature change, the indicator with the catenary diaphragm pressure receiver showed a pressure reference level change of approximately 1 per cent of that for the flat-diaphragm unit. This result is in accord with the theoretical prediction that, with a diaphragm of high flexibility, average temperature changes would not affect the indicated pressure output.

The test results of the effect of average support temperature on the *pressure input - voltage output sensitivity* of the catenary diaphragm pressure receiver unit is given in Fig. 16, together with the theoretical calculations. The *pressure - voltage sensitivity performance ratio*, which is the ratio of the actual sensitivity to the sensitivity for the unit at a temperature of 68°F., shows a deviation of less than 1 per cent from unity for temperatures between 68° and 400°F. With air cooling, the operating temperature of a catenary diaphragm pressure receiver never exceeds about 150°F.; therefore, the system sensitivities of indicators using catenary diaphragm pressure receiving units will be free from

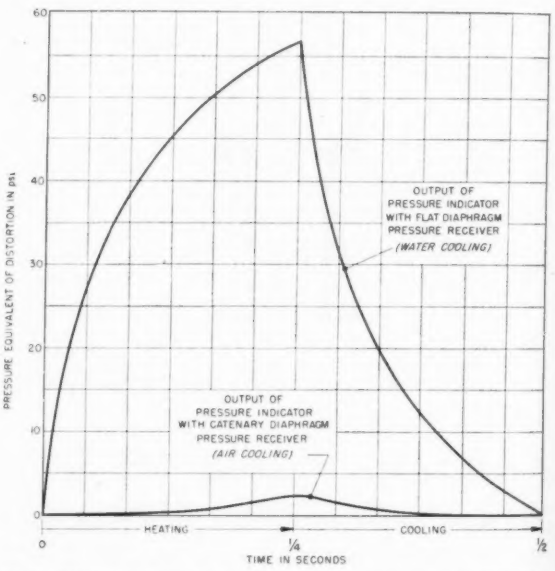

FIG. 23 RESPONSE OF PRESSURE INDICATORS TO PERIODICALLY VARYING TEMPERATURE.

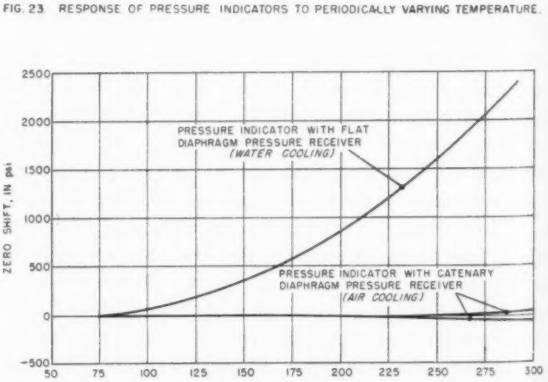

FIG. 24 EFFECT OF SUPPORT TEMPERATURE ON ZERO REFERENCE OF PRESSURE INDICATORS WITH 1000 psi MAXIMUM SCALE READING.

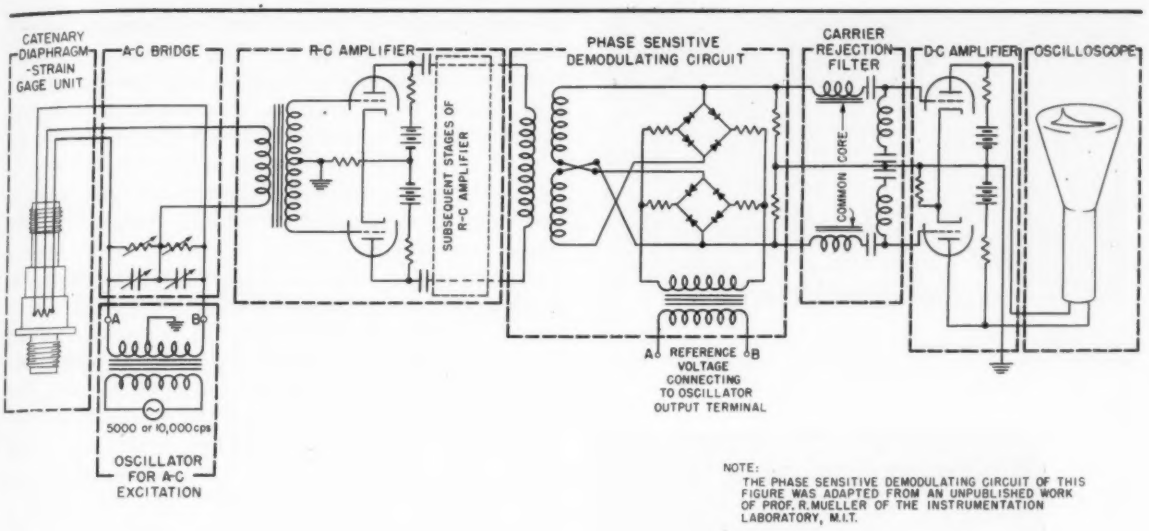
CATENARY DIAPHRAGM -STRAIN GAGE UNIT
A-C BRIDGE
R-C AMPLIFIER
SUBSEQUENT STAGES OF R-C AMPLIFIER
PHASE SENSITIVE DEMODULATING CIRCUIT
CARRIER REJECTION FILTER
COMMON CORE
D-C AMPLIFIER
OSCILLOSCOPE
A
B
5000 or 10,000 cps
OSCILLATOR FOR A-C EXCITATION
REFERENCE VOLTAGE CONNECTING TO OSCILLATOR OUTPUT TERMINAL
NOTE:
THE PHASE SENSITIVE DEMODULATING CIRCUIT OF THIS FIGURE WAS ADAPTED FROM AN UNPUBLISHED WORK OF PROF. R. MUELLER OF THE INSTRUMENTATION LABORATORY, M.I.T.

FIG. 25 CIRCUIT DIAGRAM OF A-C CARRIER SIGNAL GENERATING SYSTEM FOR CATENARY DIAPHRAGM PRESSURE INDICATOR.

temperature effects under all ordinary operating conditions.

Life tests of 100-hours engine operation have shown no essential deterioration of the units.

(VII) Typical Records of Engine Pressure Variations Taken by Indicators Using the Catenary Diaphragm Pressure Receiver

Pressure - Time Records

Pressure records from operating engines may be taken by applying to the receiver winding of a catenary diaphragm pressure receiver either a constant voltage, as shown in the wiring diagram of Fig. 17, or an a.c. voltage, as shown in the wiring diagram of Fig. 25. A typical pressure-time record is produced when constant voltage excitation is used and when the sweep frequency of a conventional cathode-ray oscilloscope, acting as the time axis, is properly synchronized with the cycle frequency. A record of this kind is visible on the face of the cathode-ray tube pictured in Fig. 18. In taking permanent photographic records, it is more accurate to provide the time axis by means of a constant speed film rather than by using the sweeping circuit of the oscilloscope. The overall accuracy of single-cycle pressure records taken by photographing the cathode-ray trace can be checked by comparing points taken from these records with corresponding points on an average pressure record taken at the same time as the continuous pressure records. Fig. 26 shows points from a typical single-cycle pressure record, taken by an indicator using the catenary diaphragm pressure receiver with constant voltage excitation, superimposed on the corresponding average pressure record from an M.I.T. Balanced Pressure Diaphragm Indicator.[26] This figure shows that all the points from the single-cycle record fall within the spread of averaging indicator points produced by the inherent variations between successive engine cycles.

This agreement has been consistently repeated for variations of engine conditions. In general, it appears that the continuous pressure records for an indicator using the catenary diaphragm pressure receiver will have inaccuracy components no greater than the inaccuracies of high-performance averaging indicators.

Constant voltage excitation for the strain receiver winding is easily obtained in practice by using conventional "B" batteries. If the frequency of the engine power cycles were faster than 4 cycles per sec., the characteristics of amplifiers usually included in commercial cathode-ray oscilloscopes would give satisfactory pressure records. However, at engine speeds corresponding to less than 4 power cycles per sec., a satisfactory system requires amplifier performance not usually built

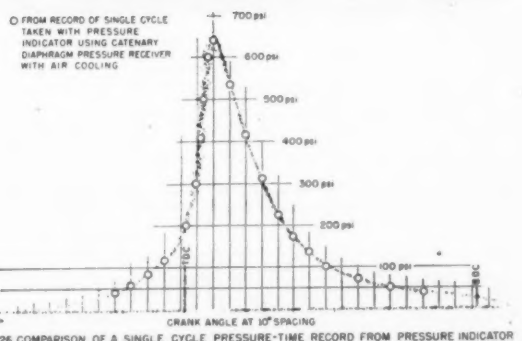
O FROM RECORD OF SINGLE CYCLE TAKEN WITH PRESSURE INDICATOR USING CATENARY DIAPHRAGM PRESSURE RECEIVER WITH AIR COOLING
700 psi
600 psi
500 psi
400 psi
300 psi
200 psi
100 psi
CRANK ANGLE AT 10° SPACING

FIG 26 COMPARISON OF A SINGLE CYCLE PRESSURE-TIME RECORD FROM PRESSURE INDICATOR USING CATENARY DIAPHRAGM PRESSURE RECEIVER WITH AVERAGING INDICATOR RECORD TAKEN UNDER SAME ENGINE OPERATING CONDITIONS.

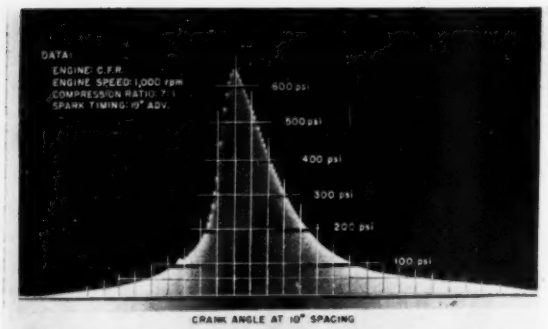

FIG. 27 ENGINE PRESSURE - TIME RECORD FROM INDICATOR USING CATENARY DIAPHRAGM PRESSURE RECEIVER UNIT WITH ALTERNATING CURRENT EXCITATION AT 5000 CYCLES PER SECOND.

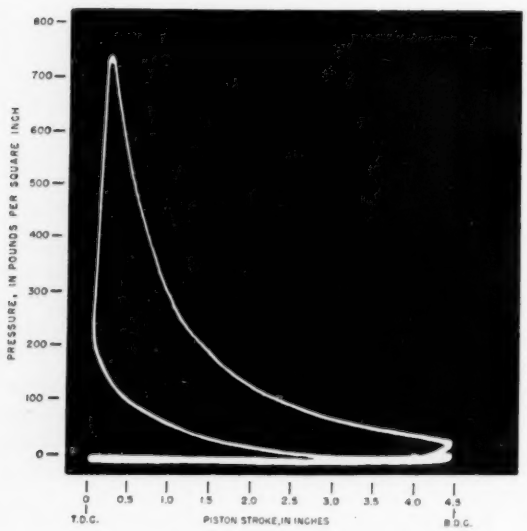

FIG. 28 ENGINE PRESSURE - VOLUME RECORD FROM PRESSURE INDICATOR WITH CATENARY DIAPHRAGM PRESSURE RECEIVER AND SPIRAL SPRING - STRAIN GAGE CRANK ANGLE - PISTON POSITION SIGNAL GENERATOR.

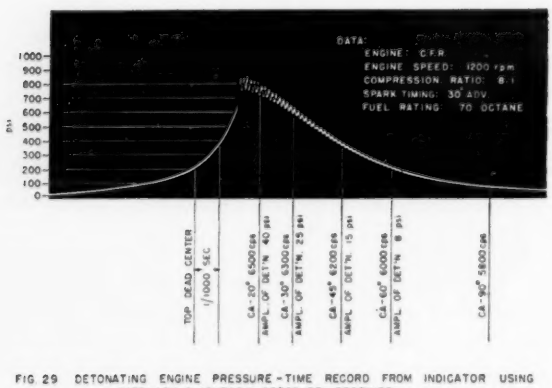

FIG. 29 DETONATING ENGINE PRESSURE - TIME RECORD FROM INDICATOR USING CATENARY DIAPHRAGM PRESSURE RECEIVER.

into standard equipment. The practical result of this defect in indicating system performance is that the pattern on the cathode-ray tube is considerably distorted, with insufficient screen indication during lower rate of pressure change. This effect may be eliminated by using a relatively high-frequency (5,000 cycles per sec. or higher) a.c. voltage for exciting the strain receiver winding. When a carrier frequency of this kind is used, the pressure modulated output of the pressure receiver unit can be transmitted by commercial resistance-capacitance coupled amplifiers, without causing the indicated pressure pattern to shift its zero when changes occur in engine-operating conditions. By incorporating a demodulating circuit in the electrical components of the coupling system or the indicating system, as shown in Fig. 25, the pressure indications will appear as a simple trace on the face of the cathode-ray tube. It is also possible to apply the modulated signal output from the strain receiver winding directly to the input terminals of a cathode-ray oscilloscope indicating system. Because of the lower linear velocity of the cathode-ray spot near the peak of its travel, the envelope of the pattern is outlined by bright points, corresponding to longer times for the electron beam to excite the fluorescent screen. Fig. 27 is a photograph showing the pressure-time record produced by alternating-current excitation of the strain receiver winding without use of demodulation. Records of this kind can be generated by a comparatively simple electrical coupling system, with a commercial cathode-ray oscilloscope for the indicating system.

Pressure - Volume Records

Pressure-volume records can be obtained from a pressure indicator system like that of Fig. 18 by making the horizontal motion of the cathode-ray spot follow the piston motion instead of being a linear function of time. A simple converter from crank angle into signal of piston position can be made by using a *model crank and connecting rod combination*, with relative proportions identical with those of the actual engine, to stretch a spiral spring in proportion to piston displacement. If the crank of the model is made to rotate with the crank of the engine, the electrical signal output from the strain of the stretching spring will be proportional to the engine piston position. A pressure-volume record like that of Fig. 28 is produced when this piston position signal is applied to the horizontal deflection plates of the cathode-ray oscilloscope, whose vertical deflection plates receive the signals from the pressure receiver.

Detonation Records

The sample records of Figs. 26, 27, and 28 illustrate the ability of indicators using the catenary diaphragm pressure receiver to measure the pressure variations associated with the power-generating functions of an engine. Any generally satisfactory continuous pressure indicator must not only record average cycle variations but must also accurately measure the relatively high-frequency fluctuations associated with detonation. Fig. 29 shows a pressure - time record taken from an engine operating with severe detonation. The time scale is ex-

panded longer than that for power analysis in order to show more clearly the fine structure of the high-frequency pressure changes. Amplitudes and frequencies of the pressure variations associated with detonation are marked in Fig. 29 as functions of crank angle.

A curve showing detonation frequency as a function of crank angle, obtained from the record of Fig. 29, is given in Fig. 30. Also plotted in Fig. 30 are curves of detonation frequency as a function of crank angle, based on theoretical computations[35] and on data taken from records made with the same engine type and operating conditions from an indicator using a flat-diaphragm pressure receiver.[3]

The detonation frequency curve, based on data from the indicator using the catenary diaphragm, matches the computed results and also matches the measurement made by an indicator differing greatly in design from the catenary diaphragm unit. In addition to the agreement in frequency, the detonation pressure amplitudes of Fig. 29 have magnitudes that are approximately equal to estimated amplitudes derived from measurements of rates of change of pressure.[35] For example, these measurements showed that, under detonating conditions similar to those used in making the record of Fig. 29, the detonation pressure amplitude at 20° after top dead center was about 40 lbs. per sq.in. Reference to Fig. 29 shows that this amplitude is substantially equal to the directly measured amplitude for the same crank angle.

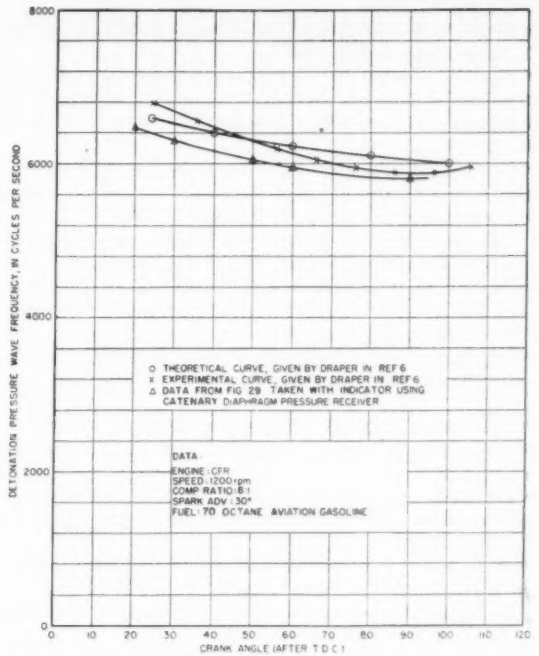
8000
6000
4000
2000
0
DETONATION PRESSURE WAVE FREQUENCY, IN CYCLES PER SECOND
0 THEORETICAL CURVE, GIVEN BY DRAPER IN REF 6
x EXPERIMENTAL CURVE, GIVEN BY DRAPER IN REF 6
Δ DATA FROM FIG 29 TAKEN WITH INDICATOR USING CATENARY DIAPHRAGM PRESSURE RECEIVER
DATA:
ENGINE: CFR
SPEED: 1200 rpm
COMP RATIO: 8:1
SPARK ADV: 30°
FUEL: 70 OCTANE AVIATION GASOLINE
0 10 20 30 40 50 60 70 80 90 100 110 120
CRANK ANGLE (AFTER T.D.C.)

FIG 30 COMPARISON OF DETONATION FREQUENCY MEASUREMENTS FROM INDICATOR USING CATENARY DIAPHRAGM PRESSURE RECEIVER WITH THEORETICAL FREQUENCY DATA AND EXPERIMENTAL MEASUREMENTS TAKEN WITH INDICATORS USING FLAT DIAPHRAGM TYPE PRESSURE RECEIVER

Summary

It has been brought out in this paper that continuous pressure indicators available up to this time have performance defects that make them unsuitable for obtaining satisfactory pressure records from modern engines. These difficulties have been largely due to undesirable characteristics inherent in the flat-diaphragm type of pressure receiver used with the indicators. The discussion of this paper summarizes the problem to show that excessive sensitivity to temperature, mechanical strain resulting from mounting stresses, and mechanical vibrations in the walls of the pressure chamber are the principal sources of trouble. A semiquantitative discussion leads to the conclusion that the flat-diaphragm type pressure receiver will always be subject to intolerable inaccuracies under the operating conditions of modern engines.

A new pressure receiver with greatly improved performance is described. This instrument is practically free from temperature and installation-strain effects and has a greatly reduced sensitivity to vibration as compared with the flat-diaphragm type pressure receivers. This unit is made up of a catenary diaphragm and a strain generating tube, wound with a wire strain gage. Typical results from laboratory tests and engine runs are included to show that, on the basis of an inaccuracy tolerance of 1 per cent, indicators using the new receiver will be satisfactory under engine operating conditions.

References

[1] Draper, C. S., Lancor, J. H., Davis, L., *The Application of an Electromagnetic Indicator to Internal Combustion Engine Problems*, Journal of the Aeronautical Sciences, Vol. 8, No. 1, pp. 7–16, October, 1940.

[2] Grinstead, C. E., Frawley, R. N., Chapman, F. W., Schultz, H. F., *An Improved Indicator for Measuring Static and Dynamic Pressures*. SAE Transactions, Vol. 52, No. 11, pp. 534–555, November, 1944.

[3] Draper, C. S., *The Physical Processes Accompanying Detonation in the Internal Combustion Engine*, M.I.T. D.Sc. Thesis, May, 1938.

[4] Draper, C. S., *The Physical Effects of Detonation in a Closed Cylindrical Chamber*, N.A.C.A. T.R. No. 493, 1934.

[5] Fowler, R. C., and Lamphere, R., *A Piezo-Electric Indicator*, M.I.T. S.B. Thesis, 1947.

[6] Martin, E. J., and Caris, P. F., *An Electrical Engine Indicator*, The Electric Journal, Vol. 27, pp. 87–91, February, 1930; Vol. 27, pp. 168–172, March, 1930.

[7] Hildebrandt, A. P., and Randolph, T. F., *Application of Wire Strain Gage to High Speed Engine Indicators*, M.I.T. S.B. Thesis, October, 1944.

[8] Roess, L. C., *Condenser Type High-Speed Engine Indicator*, Review of Scientific Instruments, Vol. II, pp. 183–195, June, 1940.

[9] Watson, H. G. I., and Keys, D. A., *Piezo-Electric Method of Measuring Pressure Variations in Internal-Combustion Engines*, Canadian Journal of Research, Vol. 5, pp. 322–331, March, 1932.

[10] Beale, E. S. L., and Stansfield, R., *High Speed Engine Indicators*, Engineer, Vol. 163, pp. 240–241, February 26, 1937; pp. 270–273, March 5, 1937.

[11] Crossley, Alfred, *The Pressure Graph*, Proceedings of the National Electronics Conference, Vol. 2 1946.

[12] Dejuhasz, K. J., *Use of Electrical Pressure Indicators Limited in Automotive Tests*, Automotive Industries, Vol. 60, No. 17, pp. 662–664, April 27, 1929.

[13] Tozier, R. E., *The NACA Optical Engine Indicator*. N.A.C.A. T.N. No. 634, January, 1938.

[14] *An Electro-Optical Engine Indicator*, Laboratory Equipment for Testing and Research Work on Diesel Engines, Bulletin No. 3, Diesel Engine Manufacturers Association, Chicago, March 15, 1948.

[15] Smith, F. D., *Basic Principles in the Design of Cathode-Ray Engine Indicators*, Institution of Mechanical Engineers, Journal and Proceedings, Vol. 143, pp. 48–56, April 1, 1940.

[16] Robertson, A. F., *An Electro-Optic Engine Indicator*, Review of Scientific Instruments, Vol. 12, pp. 142–148, March, 1941.

[17] Heldt, P. M., *Photo-Electric Cell Used with Mirror Diaphragm in New Labarthe Indicator*, Automotive Industries, Vol. 70, No. 6, pp. 160–163, February 10, 1934.

[18] Schweitzer, P. H., *Cathode-Ray Engine Indicators Have Advantages*, Automotive Industries, Vol. 80, pp. 612–613, 621, May 15, 1939.

[19] Lichtenberger, Fritz, *Valuation and Tests of Electrical Engine-Indicators*, Automotive Industries, Vol. 82, pp. 368–375, April 15, 1940.

[20] Mayes, F. M., and Linderman, M. A., *New Pressure Indicator Design*, Automotive and Aviation Industries, Vol. 96, pp. 38–39, 78, May 1, 1947.

[21] Head, J. W., *Electronic Engine-Pressure Indicator*, Electronics, Vol. 18, pp. 132–135, January, 1945.

[22] Heldt, P. M., *Engines on the Spot*, Automotive Industries, Vol. 74, pp. 398–402, March 14, 1936.

[23] Jacklin, H. M., *Some Uses of the High-Speed Multi-Cylinder Indicator*, Mechanical Engineering, Vol. 49, pp. 543–546, May, 1927. Discussion: *High Speed Indicators for Gas and Oil Engines*, Mechanical Engineering, Vol. 49, pp. 1312–1314, December, 1927.

[24] Martin, E. J., and Caris, D. F. *Rapidly Fluctuating Pressures Measured Electrically by Indicator Combined with Spark Plug*, Automotive Industries, Vol. 62, No. 7, pp. 230–237, February 15, 1930.

[25] Martin, E. J., and Caris, D. F., *A New Type of Electrical Engine-Indicator*, SAE Journal, Vol. 22, pp. 620, 689, July, 1928.

[26] Taylor, E. S., and Draper, C. S., *A New High-Speed Engine Indicator*, Mechanical Engineering, Vol. 55, pp. 169–171, March, 1933.

[27] Dickinson, H. C., and Newell, F. B., *A High-Speed Engine Pressure Indicator of the Balanced Diaphragm Type*, N.A.C.A. T.R. No. 107, 1920.

[28] Collins, John H., Jr., *Alteration and Test of the Farhboro Engine Indicator*, N.A.C.A. T.N. No. 348, 1930.

[29] *The Burgess-Manning Sampling-Valve Manometer*, Laboratory Equipment for Testing and Research Work on Diesel Engines, Bulletin No. 4, Diesel Engine Manufacturers Association, Chicago, May 3, 1948.

[30] DeJuhasz, K. J., *The Engine Indicator;* New York Instrument Publishing Company, 1934.

[31] Heldt, P. M., *Japanese Scientists Develop Simple Optical Indicator*, Automotive Industries, Vol. 71, pp. 813–814, June 30, 1934.

[32] *The S.R.-4 Bonded Resistance Wire Strain Gage*, Bulletin No. 179, Baldwin Locomotive Works, Baldwin-Southwark Division, Philadelphia, 1945.

[33] deForest, A. V., *Characteristics and Aircraft Applications of Wire Resistance Strain Gages*, Instruments, Vol. 15, pp. 112–115, April, 1942.

[34] Ruge, Arthur C., *The Bonded Wire Gage Torquemeter*, Proceedings of the Society for Experimental Stress Analysis, Vol. 1, No. 2, pp. 68–72, 1944.

[35] Draper, C. S., *Pressure Waves Accompanying Detonation in the Internal Combustion Engine*, Journal of the Aeronautical Sciences, Vol. 6, pp. 219–226, April, 1938.

[36] Draper, C. S., Taylor, E. S., Lancor, J. H., and Coffey, R. T., *Development of a Detonation Detector Suitable for Use in Flight*, N.A.C.A. T.N. No. 977, 1944.

[37] Meier, J. H., *Development of an Electrical Strain Gage and its Application to the Stress Problem in Elevated Water Tanks*, M.I.T. D.Sc. Thesis, 1939.

[38] Dodds, E. M., *Development and Application of the Cathode-Ray Engine Indicator*, SAE Transactions, Vol. 31, pp. 487–495, December, 1936.

[39] Martin, E. J., Grinstead, C. E., and Frawley, R. N., *An Electrical Engine Indicator for Measuring Static and Dynamic Pressure*, A.I.E.E. Transactions, Vol. 60, pp. 513–523, March, 1941.

[40] Davis, L. I., *The Development of an Electromagnetic Indicator for Use With High Speed Internal Combustion Engines*, M.I.T. S.M. Thesis, 1941.

[41] King, H. F., *A Piezo-Electric Method of Measuring Periodic Pressure Variations*, M.I.T. Sc.D. Thesis, 1934.

[42] Baumberger, R., and Hines, F., *Practical Reduction Formulas for Use on Bonded Wire Strain Gages in Two-dimensional Stress Fields*, Proceedings of the Society for Experimental Stress Analysis, Vol. II, No. 1, pp. 113–127, 1944.

[43] Taylor, C. F., Draper, C. S., Taylor, E. S., and Williams, G. L., *A New Instrument Devised for the Study of Combustion*, SAE Transactions, Vol. 29, pp. 59–62, February, 1934.

[44] Manson, S. S., Kemp, R. H., and Morgan, W. C., *High-Temperature Strain Gages and Their Application to Measurement of Vibratory Stresses in Turbo Supercharger Buckets*, Proceedings of the Society for Experimental Stress Analysis, Vol. V, No. 1, pp. 90–100, 1947.

[45] Kemp, R. H., Morgan, W. C., and Manson, S. S., *The Application of High-Temperature Strain Gages to the Measurement of Vibratory Stresses in Gas-Turbine Buckets*, N.A.C.A. T.N. No. 1174, 1946.

[46] Ball, L. M., *Strain Gage Technique*, Proceedings of the Society for Experimental Stress Analysis, Vol. III, No. 1, pp. 1–22, 1945.

[47] Rayleigh, John W. S., Baron. *The Theory of Sound*, Two volumes, Ed. 2 Revised and Enlarged; MacMillan and Company, London, 1894–1896.

[48] Timoshenko, Stephen, *Theory of Plates and Shells;* McGraw-Hill Book Company, Inc., New York, 1940.

[49] Obata, Juichi, Kuse, Rigakuh, and Yosida, Yahei, *An Electrical Indicator for High-Speed Internal-Combustion Engines*, Report of the Aeronautical Research Institute, Tokyo Imperial University, No. 28, December, 1927.

[50] Beale, E. S. L., and Stansfield, R., *The Standard-Sunbury Engine Indicator*, The Engineer, Vol. CLX, No. 4170, pp. 617–619, December 13, 1935; No. 4171, pp. 642–644, December 20, 1935; No. 4172, pp. 667–669, December 27, 1935.

[51] Fiene, M. E., *Electrical Method of Obtaining Indicator Card of a Compressor*, Refrigerating Engineering, Vol. 15, pp. 77–80, March, 1928.

[52] Philippsen, B. E., *Pressure Indicators in Engine Fuel Research*, Electronic Industries and Electronic Instrumentation, Vol. 1, pp. 2–3, February, 1947.

[53] Heldt, P. M., *The M.I.T. Indicator*, Automotive Industries, Vol. 72, pp. 110–113, July 28, 1934.

[54] Taylor, C. F., and Taylor, E. S., *The Internal Combustion Engine;* International Textbook Company, Scranton, Pa., Revised, 1948.

[55] Brookes-Smith, C. H. W., and Colls, J. A., *The Measurement of Pressure, Movement, Acceleration and Other Mechanical Quantities by Electrostatic Systems*, Journal of Scientific Instruments, Vol. 14, pp. 361–366, December, 1939.

[56] DeJuhasz, Kalman J., *The DeJuhasz High-Speed Engine Indicator*, Paper presented at S.A.E. Meeting, January 15–18, 1929.

[57] Sisco, F. T., *The Alloys of Iron and Carbon*, Vol. II; McGraw-Hill Book Company, Inc., New York, 1937.

[58] Bachle, C. F., *Combined Spark Plug and Indicator Valve Developed for Use With Farnboro Instrument*, Automotive Industries, Vol. 71, No. 22, pp. 686–688, December 1, 1934.

Some Aspects of Convertible Aircraft Design

ROBERT L. LICHTEN*
Bell Aircraft Corporation

SUMMARY

This paper is a contribution toward a quantitative engineering treatment of convertible aircraft design. A brief discussion of design requirements and proposed configurations is given. The analysis covers the following:

(1) *Conversion from Helicopter Rotor to Propeller Operation.*—A semigraphical process for computing rotor characteristics during the conversion process when blade-section inflow angles can no longer be considered small is presented. Calculations for a typical case indicate that no unusual or undesirable rotor behavior occurs, blade flapping decreasing progressively from the magnitude existing in helicopter operation. The rotor is shown to operate efficiently throughout, indicating that aircraft performance is not impaired during the conversion interval.

(2) *Rotor Aerodynamic Characteristics in Propeller Operation.*—It is shown that satisfactory propulsive efficiency can be obtained with isolated rotors having relatively low solidity and blade twist compared to conventional propellers. In order to obtain good efficiency at high-forward speeds, it is necessary to operate the rotor at high pitch and power coefficient. In practice, this means that when a helicopter rotor is converted to propeller operation its tip speed must be reduced considerably. Model propeller test data are compared with calculations based on modified vortex theory, and it is shown that the calculation method yields reasonably accurate results for the somewhat unusual operating conditions of the rotor-propeller.

(3) *Effect of Gravity on a Lag-Hinged Rotor in Propeller Operation.*—The undamped in-plane motion due to gravity excitation of a lag-hinged rotor blade is analyzed for operation with rotor axis horizontal. In the case of a three-bladed rotor, it is shown that the resulting hub vibratory loads are negligible. In the case of a two-bladed rotor, the amplitude of the vibratory force applied to the rotor hub is considerably greater than total blade weight, and therefore a two-bladed convertible rotor probably must be of the semirigid or rigid type to avoid this condition.

INTRODUCTION

CONVERTIBLE AIRCRAFT, which combine the ability of the helicopter to take off vertically and hover with the ability of the airplane to fly at high speed over long distances, have been proposed in various forms for many years. Design requirements for moderately high-speed flight have been generally known for some time; however, it was not until the more pressing problems associated with the development of practical helicopters were solved and corresponding design knowledge for the low-speed part of the flight spectrum became available that such proposals could be given serious consideration.

In the writer's opinion, the primary requirements for a successful convertible aircraft are that low- and high-speed performance be essentially as good as the performance of comparable helicopters and airplanes in their respective flight régimes and that the excellent controllability and maneuverability of present-day helicopters at zero and low air speeds be retained. As an airplane, the convertible aircraft must be able to fulfill an economic function. At low speed, it must be able to execute rapid and precise changes in air speed and air position, must be able to make safe landings after power failure in ground areas as small and restricted as those normally used for power-on operation, and must be relatively undisturbed by gusty air. Failure to meet these requirements would result in a degree of safety and utility too low to justify the cost of development.

DISCUSSION OF TYPES

A brief discussion of the more prominent proposed types of convertible aircraft is given here to indicate the reasons for the direction taken in the analysis. It should be emphasized that all statements made are matters of opinion at this time.

Two basic classes of direct-lift aircraft may be defined: (A) aircraft in which direct lift is obtained by imparting a relatively large downward acceleration to a relatively small mass flow of gases, as by use of rocket or turbojet engines; (B) aircraft in which direct lift is obtained by imparting a relatively small downward acceleration to a relatively large mass flow of atmospheric air, as by use of helicopter or cyclogyro rotor systems.

Class (A) fails to meet the previously stated requirements for convertible aircraft in that power failure during direct-lift operation would be disastrous, and therefore is not considered further. Class (B) will be limited to use of helicopter-type rotor systems for this discussion, and convertible aircraft in this class may be subclassified into two main groups, each having two subgroups, as follows:

(1) Aircraft having one or more helicopter-type rotors as the principal source of lift in low-speed flight; for high-speed flight, rotor rotation is stopped. (a) Longitudinal fuselage axis is approximately vertical at take-off and approximately horizontal at high speed; (b) longitudinal fuselage axis is approximately horizontal throughout the entire flight range.

(2) Aircraft having one or more helicopter-type rotors with axes approximately vertical as the principal source of lift in low-speed flight; for high-speed flight, rotor axes are tilted to an approximately horizontal attitude in which the rotors act as propellers.

Received October 30, 1948. Revised and received May 9, 1949.

* Project Engineer.

(a) Longitudinal fuselage axis is approximately vertical at take-off and approximately horizontal at high speed, and rotor axes are fixed with respect to fuselage; (b) Longitudinal fuselage axis is approximately horizontal throughout the entire flight range, and rotor axes tilt with respect to fuselage.

Types (1a) and (2a) represent entirely possible solutions. Type (1a) has been embodied in proposed aircraft having ram-jet or pulse-jet engines mounted at the tips of relatively rigid blades to drive the rotor for helicopter operation; for high-speed flight the blades are feathered and act as wings, while the jet engines provide direct propulsion. Type (2a) has been embodied in many designs, such as those proposed by Zimmerman, Young, Leonard, and Robins. In both these types, conversion from helicopter to airplane flight and return may be expected to require either a discontinuous maneuver, such as a dive or zoom, or a continuous maneuver in which control and excess power available are likely to be marginal for an appreciable time interval. The required 90° range of fuselage attitude would probably make such an aircraft unsuitable for carrying more than one or two persons. Autorotational descent in the event of power failure, with sufficient forward speed to minimize sinking speed and to provide a choice of landing sites, would be a difficult and awkward maneuver at best. For type (2a), the coaxial rotor arrangement, with two superimposed oppositely rotating rotors, is most often used, leading to solidity values that are objectionably high for propeller operation, as will be shown later.

An early example of type (1b) was the Herrick Convertaplane demonstrated with partial success in 1937. Other designs of this type have been proposed by Wilford and Gazda. Such aircraft generally require separate power transmission systems for driving the rotor in helicopter flight and for propelling the aircraft after stopping the rotor. Simplification in this respect might be effected by use of some form of jet drive for both configurations. A one-bladed rotor offers advantages for this type; however, such a rotor presents many new problems even for use on conventional helicopters. Mechanical requirements for stopping and starting large rotors in flight are likely to be severe.

Type (2b) embodies, in general, the most conventional configurations as suggested by Blount, LePage, Stuart, DuMonge, and others. This type appears to be the most suitable for large cargo and personnel transport aircraft but has the disadvantage of a relatively heavy structure and power transmission system. However, it introduces the least new design problems, permits adequate provision for safe operation after power failure, and seems most promising for immediate development. Therefore the analysis presented in the following sections is directed primarily toward this type, although it is applicable in many respects to other types discussed above.

Additional discussion is given in reference 9.

Notation

The plane of the rotor disc is a plane perpendicular to the rotor shaft axis passing through the rotor hub.

a = slope of blade section lift coefficient curve, per rad.
a_m = coefficient of $\cos m\psi$ term in expression for β
A_m = coefficient of $\cos m\psi$ term in expression for γ
b = number of blades per rotor
b_m = coefficient of $\sin m\psi$ term in expression for β
B = tip-loss factor
B_m = coefficient of $\sin m\psi$ term in expression for γ
c = chord of constant-chord blade, ft.
c_{d_0} = blade section profile drag coefficient
c_l = blade section lift coefficient
C_P = rotor shaft power coefficient $= P/[(1/2)\rho(\omega R)^3\pi R^2]$
C_T = rotor thrust coefficient $= T/[(1/2)\rho(\omega R)^2\pi R^2]$
D = rotor diameter, ft.
e_2R = distance from rotor shaft axis to lag hinge, ft.
F = Goldstein propeller theory factor (κ in reference 2)
F_c = centrifugal force on one blade, lbs.
F_y = force on rotor hub in positive y direction, lbs.
F_z = force on rotor hub in positive z direction, lbs.
I_2 = moment of inertia of blade about lag hinge, slug-ft.^{2}
k = $\tan^{-1}(c_{d_0}/c_l)$
K_1 = $I_2 - \dfrac{W_bR^2}{g}e_2L_2\dfrac{e_2+I_1}{e_2+L_2}$
K_2 = $W_bL_1R/2\omega^2$
L_1R = distance from lag hinge to blade center of gravity, ft.
L_2R = distance from lag hinge to point of application of resultant F_c, ft.
n = rotor rotational speed, revolutions per sec.
P = rotor shaft power, ft.lbs. per sec.
$p\omega$ = pitching angular velocity of rotor shaft axis, positive nose up, rad. per sec.
r = radius to a blade element, ft.
R = radius to blade tip, ft.
T = rotor thrust, vector coincident with rotor shaft axis, lbs.
$u_p\omega R$ = component of resultant velocity at a blade element, parallel to rotor shaft axis, ft. per sec.
$u_t\omega R$ = component of resultant velocity at a blade element, normal to blade span axis and parallel to rotor disc plane, ft. per sec.
v = average induced velocity at rotor disc, normal to rotor disc plane, ft. per sec.
V = true air speed along flight path, ft. per sec.
w = total induced velocity at a blade element (profile drag neglected), ft. per sec.
W_0 = resultant of V and ωr at a blade element, ft. per sec.
W = resultant of W_0 and w at a blade element, ft. per sec.
W_b = weight of one blade, lbs.
x = r/R
y = fixed horizontal coordinate in plane of rotor disc, propeller operation, ft.
z = fixed vertical coordinate in plane of rotor disc, propeller operation, ft.
α = angle between flight path and rotor disc plane, positive when leading edge of disc is raised, rad.
α_b = blade element angle of attack relative to zero-lift chord line, rad.
β = flapping angle between blade span axis and rotor disc plane, positive upward, rad.
γ = lag angle between projections in rotor disc plane of blade span axis and line connecting rotor shaft axis and lag hinge, rad.
ϵ = $\tan^{-1}(w/W)$, rad.
η = propulsive efficiency, propeller operation, $= TV/P$
η_0 = rotor profile efficiency $= T[v - V\sin(\alpha + a_1)]/P$

θ = pitch angle between blade section zero-lift chord line and rotor disc plane = $\theta_0 + \theta_1 x$, rad.
λ = inflow ratio = $(V \sin \alpha - v)/\omega R$
μ = advance ratio = $(V \cos \alpha)/\omega R$
ρ = air density, slugs per cu.ft.
σ = rotor solidity = $bc/\pi R$
ϕ_0 = $\tan^{-1}(V/\omega R)$, rad.
ϕ = $\phi_0 + \epsilon$, rad.
ψ = blade azimuth angle measured from downwind or top position, rad.
ω = rotor rotational speed = $d\psi/dt$, rad. per sec.

Conversion from Lifting Rotor to Propeller Operation

Introduction

In converting from lifting rotor to propeller operation in flight, it is highly desirable that the transition be made without requiring unusual piloting technique, penalizing performance appreciably, or causing erratic rotor behavior. The type of maneuver envisioned for the conversion process is as follows: The aircraft attains maximum forward speed as a helicopter. The pilot then actuates the conversion mechanism, causing the rotor axis to swing from an approximately vertical to an approximately horizontal attitude parallel to the flight path. This process occupies a time interval of the order of 15 sec., at the end of which the rotor is operating as a propeller and the aircraft weight load is carried by fixed wings. Conversion from propeller to lifting rotor operation is the reverse of the process described above.

Experimental Data

Flight tests of a convertible aircraft model are reported in reference 7. Using the classifications given previously, this model was of type (2a). It had a 39-in. diameter, two-bladed rotor, and gimbal mounted to permit flapping and feathering and was driven by an electric drill motor. A 48-in. span by 8-in. chord wing was mounted below the rotor with chord line parallel to rotor shaft axis. The model was mounted at the end of a dural "fish pole" 18 ft. long and was flown in a circular path around the operator. The model was free to pivot about the pole axis, and the operator had longitudinal cyclic feathering control, collective pitch control, and motor torque control. Thus, the operator controlled the model about the pitch axis by means of rotor thrust vector inclination, but the model was restrained from yawing and rolling.

In flight, the transition from hovering to high-speed flight with rotor axis horizontal could be made rapidly or slowly and was smooth and continuous. The model could be flown steadily with the rotor shaft axis in a range of attitudes from vertical to horizontal. It was also possible to perform loops and vertical figure eights. Rotor behavior was normal throughout all maneuvers.

Approximate measurements of power input gave evidence of a sharp increase in power required in the vicinity of $\alpha = -60°$ over that required in hovering and in forward flight at smaller values of α. This is attributed to operation of the wing in a stalled attitude at the relatively high forward speed corresponding to this axis inclination. As axis inclination is further increased, the wing would be expected to unstall with a consequent drop in power required, followed by a rise as maximum forward speed is attained with $\alpha \cong -90°$. Such a trend is exhibited by the test data. A curve showing the approximate variation of power required with rotor axis inclination at one rotational speed is given in Fig. 1. This curve was cross-plotted from faired curves based on the reference 7 data. No airspeed data were recorded.

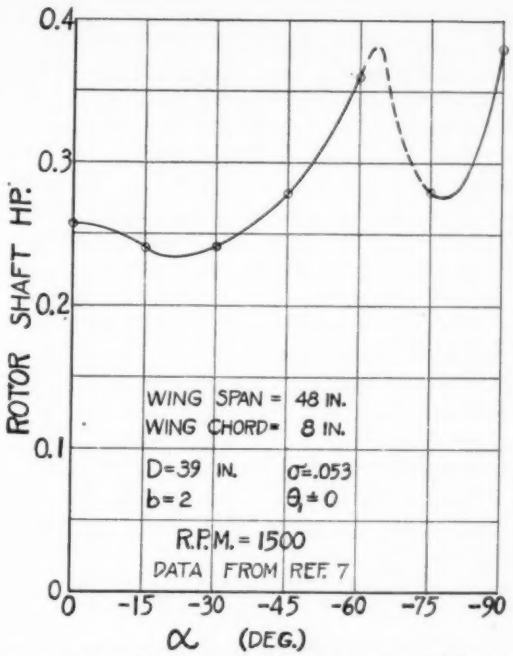

FIG. 1. Power required variation with rotor axis inclination from model flight-test data. Model wing chord line fixed parallel to rotor axis.

Analysis

During the conversion process, the principal conditions of operation which might be expected to lead to unusual rotor behavior because of differences from steady-state lifting rotor or propeller operating conditions are: (a) airflow interference caused by nonrotor parts of the aircraft; (b) the pitching angular motion of the rotor hub as the rotor axis is converted from an approximately vertical to an approximately horizontal attitude; (c) the large inflow angles, together with continuous variation of inflow angle around the blade path, which are experienced by the blade sections.

Interference effects depend on the particular configuration of the subject aircraft. They may be considered as superimposing on the airflow pattern, surrounding an isolated rotor in a given operating condi-

tion, a velocity and static pressure variation at each point in the pattern caused by the influence of other parts of the aircraft. Good design will minimize such effects; however, there are instances of difficulties encountered with propeller installations in conventional aircraft due to interference. In the present case, rotor behavior difficulties due to interference are not expected to appear, since such a rotor is already designed to accommodate the large variations with blade azimuth position and forward speed of section angle of attack and relative airflow velocity experienced in helicopter operation. Therefore interference effects are not herein considered further, although they may have a considerable effect on stability and control in particular cases.

It may be shown, exactly in the case of a flapping- or teetering-type lifting rotor at zero air speed and approximately for such a rotor in forward flight, that a steady pitching angular velocity of the hub will produce lateral flapping

$$b_1 = -p\omega/\omega = -p$$

due to aerodynamic damping of the pitching motion and will produce longitudinal flapping due to blade mass whose magnitude is dependent on the ratio of blade moment of inertia about the flapping hinge to air density and which, for typical rotor blades, is approximately

$$a_1 = -2.5p$$

These values should still be good approximations for flapping due to hub pitching velocity during the conversion process. For an angular motion of 90° in 15 sec., about 0.10 rad. per sec., and a typical rotor speed $\omega = 25$ rad. per sec., the resultant flapping amplitude would be

$$\sqrt{a_1^2 + b_1^2} = 2.7p = 0.011 \text{ rad.} = 0.6°$$

This may be considered negligible so far as any significant effect on rotor behavior is concerned, and this conclusion is supported by the fact that present small helicopters can obtain rates of roll or pitch in excess of 1 rad. per sec. in maneuvers without experiencing abnormal rotor behavior. Therefore it has been considered permissible to neglect the effect of hub pitching velocity in analyzing rotor behavior during conversion, which permits a quasi-static treatment in that steady-state operation at rotor angles of attack intermediate between lifting rotor and propeller conditions may be assumed.

The aerodynamic analysis of rotor operation in this intermediate range is complicated because the inflow angle cannot be considered a small angle as in lifting rotor analysis, while conditions at any blade station do not remain constant with respect to blade azimuth as in propeller analysis. This leads to a strip analysis with graphical integration for rotor characteristics.

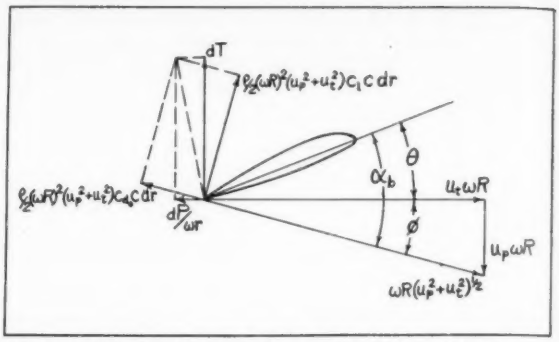

FIG. 2. Schematic diagram of a typical blade section for conversion analysis.

In addition to the assumptions that interference effects and hub pitching velocity may be neglected, the analysis is based on the following: (a) Only the component of induced velocity normal to the rotor disc plane need be considered. For this component a mean value over the disc as given by momentum theory may be used. (b) only the constant and first harmonic components of the blade flapping motion need be considered. (c) Eq. (2) of reference 8,

$$\tan \alpha = \lambda/\mu + C_T/4B^2\mu\,(\lambda^2 + \mu^2)^{1/2} \qquad (1)$$

remains valid during conversion. This equation includes an approximation for lifting rotor induced flow, based on simple momentum theory and analogy with finite airfoil theory.

The above assumptions are equivalent to those used in standard blade-element analysis of lifting rotors. Accordingly,

$$u_t = x + \mu \sin \psi \qquad (2)$$

$$u_p = \lambda - x(a_1 \sin \psi - b_1 \cos \psi) - \mu \cos \psi\,(a_0 - a_1 \cos \psi - b_1 \sin \psi) \qquad (3)$$

Referring to Fig. 2,

$$\alpha_b = \theta_0 + \theta_1 x + \tan^{-1}(u_p/u_t)$$

$$\frac{1}{\sigma}\frac{dC_T}{dx} = (u_t^2 + u_p^2)\,(c_l \cos \phi + c_{d_0} \sin \phi) \qquad (4)$$

$$\frac{1}{\sigma}\frac{dC_P}{dx} = x(u_t^2 + u_p^2)\,(c_{d_0} \cos \phi - c_l \sin \phi) \qquad (5)$$

In applying these expressions, blade airfoil section characteristics are taken from a plot that covers a large range of α_b extending well into the negative stall region.

No further details of the analysis will be given except for the following outline of the procedure followed:

(a) For a given rotor, choose a forward speed and value of α for analysis. A value of μ is derived.

(b) Select a range of values of λ and θ_0 appropriate to the chosen α.

(c) Assuming zero blade flapping, calculate C_T for each possible combination of λ and θ_0 by evaluating Eq. (4) over a range of values of x at intervals of ψ.

around the blade path (every 30° is recommended). The resulting values of dC_T/dx at each value of x are averaged with respect to ψ, and C_T is obtained by graphical integration. The tentative assumption is made that thus-obtained values of C_T are little affected by introduction of actual blade flapping.

(d) Sets of λ, μ, and C_T values from (c) are substituted in Eq. (1), yielding values of α which are plotted versus the assumed λ and θ_0 values and the calculated C_T values. Intersections at the originally assumed α value determine possible operating conditions (satisfying both momentum and blade-element conditions).

(e) For each of the possible conditions, a substitute effective value of λ is determined by substituting the corresponding C_T and θ_0 in Eq. (14) of reference 8. This is then used to compute flapping coefficients a_0, a_1, and b_1 from Eqs. (11) to (13) of reference 8.

(f) Using these flapping coefficients, values of C_T and C_P are computed following the procedure outlined in (c) for the range of possible operating conditions. Using the dC_T/dx values obtained during this computation, values of $x(dC_T/dx)$ are computed and integrated over the blade radius for each blade azimuth position. This quantity is proportional to the aerodynamic thrust moment about the flapping or teetering hinge, and a harmonic analysis of its variation with ψ is performed. A corresponding procedure is followed for the zero-flapping cases. The correct values of a_1 and b_1 are determined by interpolation between the two sets of first harmonics obtained from the

$$\int_0^B x(dC_T/dx)dx$$

variation with ψ. It may be assumed that the sine component varies linearly with a_1 and the cosine component linearly with b_1; for a hinged rotor, a_1 and b_1 are such that the first harmonic components are reduced to zero. In the actual calculations made, it was found that the flapping coefficients obtained in step (e) produced this result directly within the limits of accuracy of the method so that interpolation was unnecessary. This is indicated by the example shown in Fig. 3. In all cases the final flapping values should be sufficiently close to those calculated in step (e) that the C_T values obtained in step (f) do not require recalculation. This conclusion is supported by the small changes between values for zero and for calculated flapping shown in Table 1 for the example case. It has been assumed that similar reasoning may be applied to C_P.

TABLE 1

$\alpha = -60°$, $\mu = 0.15$, $\theta_1 = -20°$

θ_0 (rad.)	0.600	0.630	0.660
λ	−0.2600	−0.2613	−0.2627
C_T/σ (zero flapping)	−0.0125	0.0328	0.0822
C_T/σ (calculated flapping)	−0.0161	0.0334	0.0827

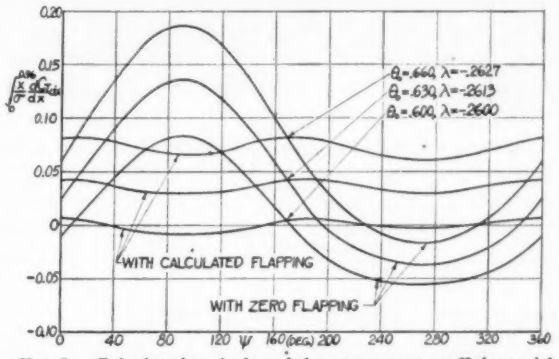

FIG. 3. Calculated variation of thrust moment coefficient with azimuth angle for example rotor. $\alpha = -60°$; $\mu = 0.15$; $\theta_1 = -20°$; $\sigma = 0.04$.

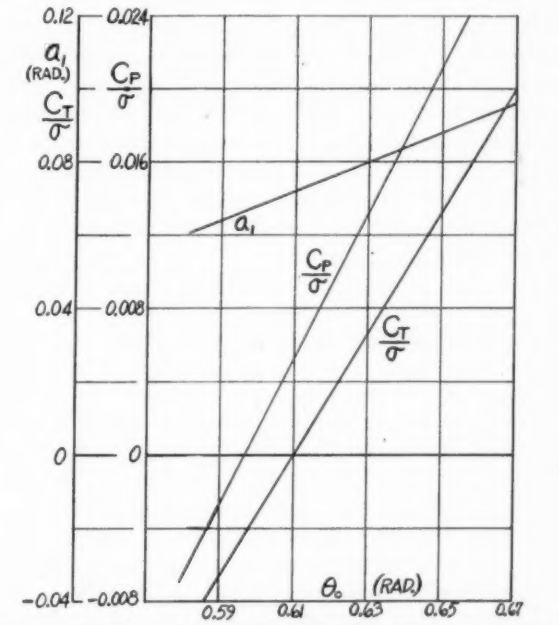

FIG. 4. Variation of longitudinal flapping, thrust, and power coefficients with blade pitch for example rotor. $\alpha = -60°$; $\mu = 0.15$; $\sigma = 0.04$; $\theta_1 = -20°$.

(g) In the $\alpha = -90°$ case (propeller operation), a considerable simplification can be made, since there is no variation with ψ and first harmonic flapping is zero. The general method outlined above may still be followed in order to obtain a comparative set of results for this limiting condition.

Some results for a set of calculations with $\alpha = -60°$ are presented as an example. Table 1 shows a comparison of C_T values as computed for cases with zero and with calculated flapping. Differences are within the limits of accuracy of the computations.

In Fig. 3, the variation of thrust moment coefficient about the flapping hinge is shown for these cases. It may be noted by inspection that the calculated flapping reduces the first harmonic variations essentially to zero. In Fig. 4, final rotor characteristics for this operating condition are shown.

TABLE 2

Rotor disc loading = 3.5 lbs. per sq.ft. (in helicopter operation)
Rotor power loading = 9.8 lbs. per shaft hp.
ωR = 612 ft. per sec., σ = 0.04
ρ = 0.00238 slug per cu.ft., $\theta_1 = -20°$

α (Deg.)	Flight Condition	V (M.P.H.)	θ_0 (Deg.)	μ	λ	a_1 (Deg.)	T (%)	η_0
0.0	Hovering	0	27.0	0.0	−0.0665	0.0	100.0	0.72
−20.3	Helicopter high speed	133	28.8	0.30	−0.1130	8.05	100.0	0.77
−30.0	Conversion	125	30.0	0.26	−0.1542	6.51	61.4	0.83
−60.0	Conversion	125	36.8	0.15	−0.2617	4.86	27.3	0.74
−90.0	Conversion complete	125	39.8	0.0	−0.3014	0.0	20.1	0.66

Interpretation of Results for Example Rotor

A summary of results obtained in a complete analysis of the example rotor operated to absorb constant shaft power at a typical helicopter tip speed, including comparative data for helicopter operation, is given in Table 2. It may be seen that longitudinal flapping coefficient a_1 decreases steadily during conversion, while required θ_0 increases, as would be expected with decreasing transverse and increasing normal flow components. Rotor thrust is given in per cent of thrust for helicopter operation. In order to indicate how much of the power input to the rotor is expended usefully during the conversion process, a profile efficiency has been defined as

$$\eta_0 = (T/P)\,[v - V \sin(\alpha + a_1)] \tag{6}$$

or approximately, since a_1 is a small angle,

$$\eta_0 = -(T/P)\,(\lambda + \mu\, a_1)\omega R \tag{6a}$$

This expression represents, to a close approximation, the ratio of the rate of useful work done on the air flowing through the rotor tip path plane to the shaft power input. It reduces to the familiar rotor figure of merit in the case of hovering flight. It will be noted that, throughout nearly the entire conversion range of α, profile efficiency exceeds that for hovering. This indicates that there should be no detrimental effect on performance during the conversion process insofar as rotor characteristics are concerned. In general, the analysis indicates that a conversion process of the type considered will introduce no undesirable rotor behavior or piloting requirements and should therefore be entirely practical.

ROTOR AERODYNAMIC CHARACTERISTICS IN PROPELLER OPERATION

General Considerations

In order to obtain high-forward speeds as an airplane after conversion from lifting rotor to propeller operation, reasonably high-rotor propulsive efficiency is required. It can be shown that operating a typical helicopter rotor as a propeller, with no change in rotational speed or rotor geometry (except for increasing blade pitch to maintain constant power absorption), results in poor propulsive efficiency at air speeds above normal helicopter maximum level flight speeds. This poor performance is a consequence of the low disc loadings that are required in helicopter design to obtain satisfactory low-speed and power-off flight performance. The condition may be explained qualitatively as follows:

The thrust produced by a rotor operating with constant power input is, roughly speaking, inversely proportional to the airflow velocity component normal to the rotor tip-path plane. For a typical rotor operating as a propeller at an air speed of, say, 170 m.p.h., this normal velocity component is about ten times greater than in hovering as a helicopter. Rotor thrust is thus of the order of one-tenth of hovering thrust. In hovering, a representative blade section might operate at $c_l = 0.5$ with a section lift/drag value of 40; accordingly, in high-speed flight the same section would operate at about $c_l = 0.05$ with a lift/drag value of about 5. Had such a rotor been required to operate *only* in the high-forward speed propeller condition, it could have been so designed that a mean blade section would operate near best lift/drag with a consequent large improvement in propulsive efficiency at high speed.

From this explanation it is clear that to improve propulsive efficiency at high speed it is at least necessary to increase the mean blade-section lift coefficient in this operating condition. This is equivalent to increasing rotor power coefficient, which might be done in the following ways:

(a) Increase the power input to the rotor. This is impractical because of the already low power loadings required for adequate performance in helicopter operation.

(b) Use contractable blades to decrease rotor diameter and tip speed during propeller operation. This would be an excellent solution if structural difficulties could be overcome. It has the disadvantage that, in the case of twisted blades, telescoping the blades would decrease overall blade twist in an operating régime where increased twist is desirable.

(c) Decrease rotational speed for propeller operation. This appears to be the only practical solution at present. It requires the use of a variable-speed transmission and requires provision for the increased rotor torque realized when rotor speed is decreased.

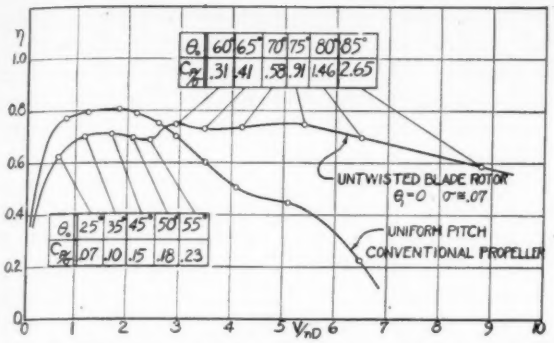

FIG. 5. Envelope propulsive efficiency curves from General Electric Company data. $\alpha = -90°$; $D = 2$ ft.; $b = 2$.

An associated problem is provision of proper blade twist. In helicopter operation, moderate amounts of blade twist have the advantageous effects of reducing hovering induced power losses, reducing peak blade bending moments, and increasing the forward speed at which stall of the retreating blade tip begins to occur. However, it is generally agreed that the region of diminishing returns is reached when more than about 10° total twist from blade root to tip is used. Although never demonstrated experimentally, it has been presumed that excessive blade twist would lead to reduced performance in autorotation due to stalling of the blade root sections and, possibly, to an undesirable blade bending moment distribution.

Optimum total twist for conventional propeller blades is of the order of 45°. The amount of twist used in a particular case depends on the design advance ratio for the propeller: the higher the advance ratio, the less twist required. When a propeller operates with nonoptimum twist distribution, propulsive efficiency suffers because of increased profile and induced losses.

The conflicting blade twist requirements for lifting rotor and propeller operation may be met in two ways: (a) use blades whose twist may be varied, or (b) use a compromise permanent twist distribution. The first alternative would be preferable if a reliable method for varying blade twist were available. At present,

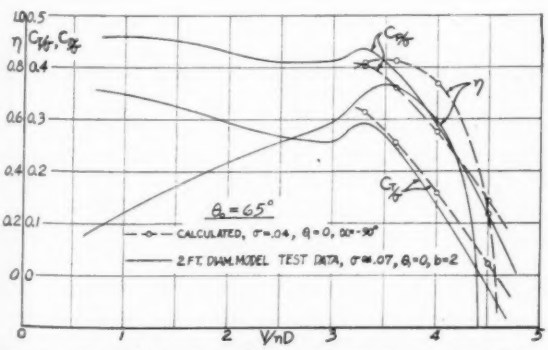

FIG. 6. Comparison of calculated and experimental untwisted-blade propeller characteristics.

it is thought necessary to adopt the second alternative. Accordingly, for the calculations of this paper untapered blades with 20° linear twist from root to tip have been assumed. It may be mentioned in passing that preliminary analyses for such blades in lifting rotor operation have indicated that, compared to equivalent untwisted blades, blade bending moments at high-forward speed are somewhat less severe, and that the initial point of stall on the retreating blade is moved inboard from the tip to about $x = 0.65$ and occurs at a higher forward speed. There is no evidence of impairment of autorotational performance, but the calculations do not account for losses due to blade stall.

Experimental Data

Available test data on rotors operating as propellers are extremely limited, and, except for a few cases, propeller test data cannot be used because of wide differences between conventional propellers and the proposed type of rotor in blade twist, plan form, and solidity.

The General Electric Company has kindly made available unpublished results of extensive model tests made under its auspices. A summary of some of these data is presented in Fig. 5, where an envelope propulsive efficiency curve obtained with a 2-ft. diameter, two-bladed model rotor with untwisted blades operated through a large range of pitch angles is shown. Pitch angles and power coefficients are spotted along this curve to indicate the operating condition. A large spinner with diameter approximately 25 per cent of rotor diameter was used on this rotor, and spinner tare drag was added to observed thrust in calculating propulsive efficiency; therefore, resulting efficiency values are probably somewhat too high, since the inner portions of such untwisted blades normally would be stalled negatively in propeller operation, except at the highest pitch angles. For comparison, a 2-ft. diameter two-bladed model of a conventional propeller of uniform design pitch was tested concurrently, and the envelope propulsive efficiency curve for this model is also shown in Fig. 5. It should be noted that these tests were carried through much higher values of the advance ratio, V/nD, than is normal for propeller operation. For example, in cruising flight the DC-3 airplane operates at about $V/nD = 1.2$. The conventional propeller model shows decided superiority in the low-advance ratio range, while the untwisted-blade rotor model is superior above $V/nD = 3.0$. It is notable that a propulsive efficiency of 0.70 was obtained with the untwisted-blade rotor at 80° pitch, and, for a considerable pitch range below this, somewhat better efficiency is realized. (The low Reynolds Number of the model tests compared to full scale probably resulted in propulsive efficiency values lower than would be obtained in full-scale tests.)

A rapid increase in power coefficient required for operation at envelope efficiency as pitch is increased is

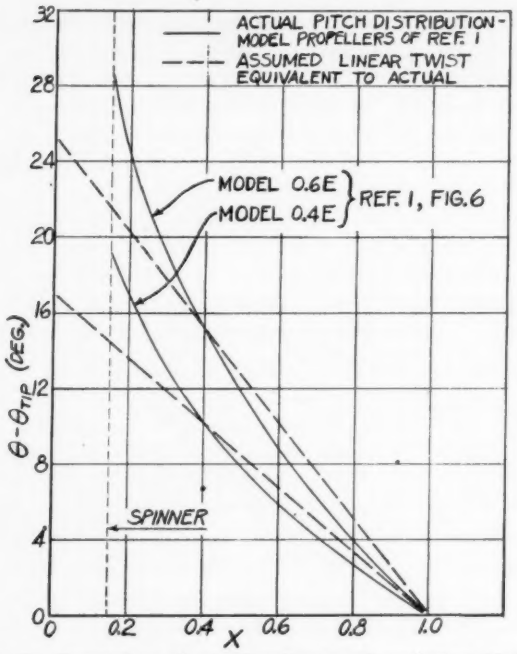

FIG. 7. Comparison of actual and assumed equivalent blade pitch distributions.

apparent. As a consequence, operation with constant power input would require that tip speed for $\theta_0 = 80°$ be only 40 per cent of the tip speed required at $\theta_0 = 35°$. These results indicate that even an untwisted-blade rotor might perform satisfactorily as a propeller under proper operating conditions.

In Fig. 6 test results for the untwisted blade rotor at a particular pitch setting are compared with values calculated by the method described below. The fair agreement indicates that the calculation method provides a reasonably close prediction of magnitude and trend. Part of the discrepancy may be explained by the fact that the rotor assumed in the calculations had lower solidity and blade sections operating at a much higher mean Reynolds Number than the model rotor, which would tend to reduce induced and profile losses for the calculations in comparison to the test data.

A second source of applicable data is found in reference 1, where excellent data are presented from tests of 34-in. diameter model propellers, including several having unusually low amounts of blade twist and roughly constant chord from shank to tip. The twist distributions for two of the model blades are shown in Fig. 7; for purposes of this analysis it has been assumed that test results for propellers using these blades would be closely approximated by untapered blades having an equivalent linear twist distribution given by the dashed lines of the figure. From Fig. 1 of reference 1, the estimated effective value for the solidity of these propellers is $\sigma = 0.120$. This is about triple the solidity desired for the type of rotor under discussion. However, it has been assumed that, for a given operating condition, thrust and torque coefficients vary directly with solidity, and propulsive efficiency is independent of solidity. These assumptions are valid only for conditions where axial and rotational induced velocities are negligibly low, which conditions are approximately fulfilled in the present cases.

In Fig. 8 propulsive efficiency curves are shown for a typical low-solidity rotor operating at several different power coefficients. These curves were interpolated from the test data of reference 1 in accordance with the assumptions stated above. In order to show their physical significance, the Fig. 8 curves have been replotted in Fig. 9 in terms of the operation at various tip speeds of a 19-ft. diameter rotor absorbing 100 shaft hp. The curve for 671 ft. per sec. tip speed shows propeller operation at a tip speed that might be used for a typical modern rotor in helicopter operation. Propeller performance is poor in this condition. When tip speed is reduced, a considerable increase occurs both in peak efficiency and in air speed for peak efficiency. The curve for 230 ft. per sec. tip speed represents acceptable propeller performance for a moderately high-speed airplane.

In Figs. 10, 11, and 12, some of the test curves of reference 1 for constant pitch settings are shown as interpolated for 20° linear blade twist. (The nominal pitch settings of reference 1 have been increased by 3° to account for the mean difference between nominal and zero-lift blade chord lines as indicated by Fig. 3 of

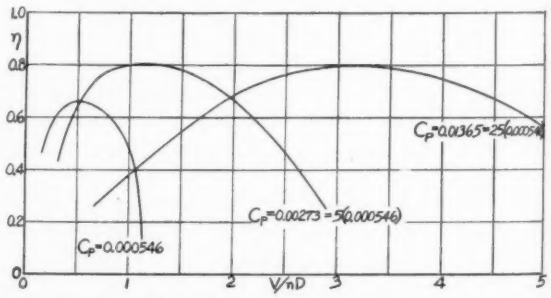

FIG. 8. Propulsive efficiency curves for operation at constant power coefficient, based on model test data. $\sigma = 0.04$; $\theta_1 = -20°$; $\alpha = -90°$.

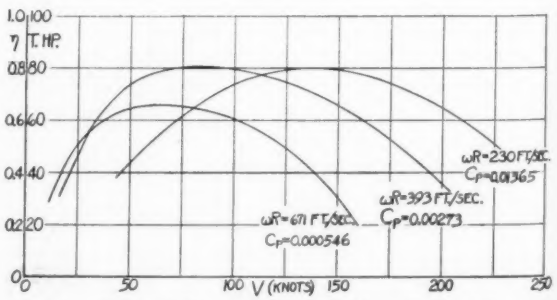

FIG. 9. Effect of tip speed on propulsive efficiency for constant power operation, based on model test data. $\alpha = -90°$; $D = 19$ ft.; $\sigma = 0.04$; $\theta_1 = -20°$; b.hp. = 100; altitude = sea level.

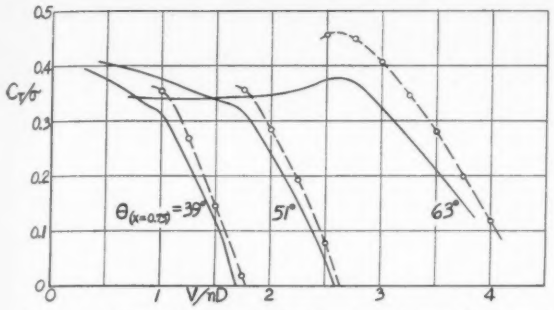

FIG. 10. Comparison of calculated and model test thrust coefficient variation with advance ratio. $\alpha = -90°$. ——Test data, 34 in. diameter, $\sigma = 0.12$, interpolated for $\theta_1 = -20°$. —o— Calculated, $\sigma = 0.04$, $\theta_1 = -20°$.

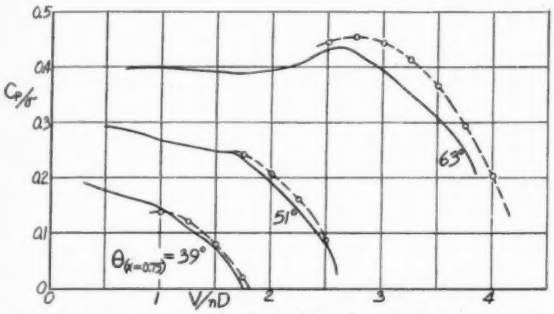

FIG. 11. Comparison of calculated and model test power coefficient variation with advance ratio. $\alpha = -90°$. ——Test data, 34 in. diameter, $\sigma = 0.12$, interpolated for $\theta_1 = -20°$. —o— Calculated, $\sigma = 0.04$, $\theta_1 = -20°$.

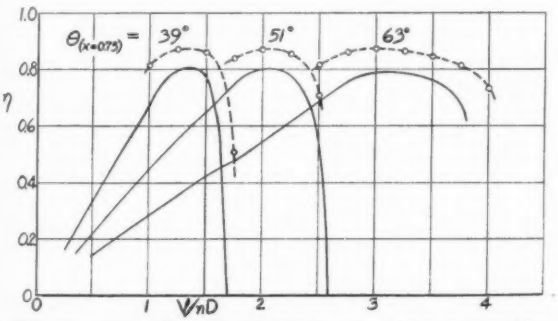

FIG. 12. Comparison of calculated and model test propulsive efficiency variation with advance ratio. $\alpha = -90°$. ——Test data, 34 in. diameter, $\sigma = 0.12$, interpolated for $\theta_1 = -20°$. —o— Calculated, $\sigma = 0.04$, $\theta_1 = -20°$.

reference 1.) These are compared with values calculated by the method described in the next section. Agreement is fair, although differences appear to increase with increasing pitch. The calculations yield peak propulsive efficiencies about 10 per cent too high. As in the case of the General Electric Company data, part of the discrepancies may be explained by the fact that the rotor assumed in the calculations had a much lower solidity and had blade sections operating at a higher mean Reynolds Number than the model propeller. Also, hub drag was not accounted for in the calculations. On the basis of these comparisons, it is probably correct to conclude that the calculation method will give reasonably accurate results for the somewhat unusual operating conditions required for the rotor-propeller.

Calculated Aerodynamic Characteristics

The method of propeller analysis used for the calculations of this paper is an adaptation of the methods of references 2 and 3, which are based on standard vortex theory with Goldstein corrections. In reference 3 a comparison between experiment and calculations by this method is shown, in which excellent agreement was obtained through $V/nD = 6.0$ in spite of blade loadings that varied widely from that on which the Goldstein theory is based. In the present case, blade loadings vary more widely from that of the Goldstein theory than did the loadings of reference 3; however, it is thought that reasonable agreement should still be obtained.

A diagram of the flow condition at a typical blade element is shown in Fig. 13. That part of the induced velocity which is due to profile drag is neglected. ϵ is a small angle.

The fundamental relation of the vortex propeller theory as modified by Goldstein may be written as

$$w = BcWc_l/8\pi rF \sin \phi \tag{7}$$

or,

$$\tan \epsilon = w/W = \sigma c_l/8xF \sin \phi \tag{7a}$$

From the diagram, Fig. 13,

$$W = (\omega r/\cos \phi) - w \tan \phi$$
$$= (\omega r/\cos \phi) - W(\tan \epsilon)(\tan \phi) \tag{8}$$

$$W \sin \phi = \omega r/(\cot \phi + \tan \epsilon) \tag{9}$$

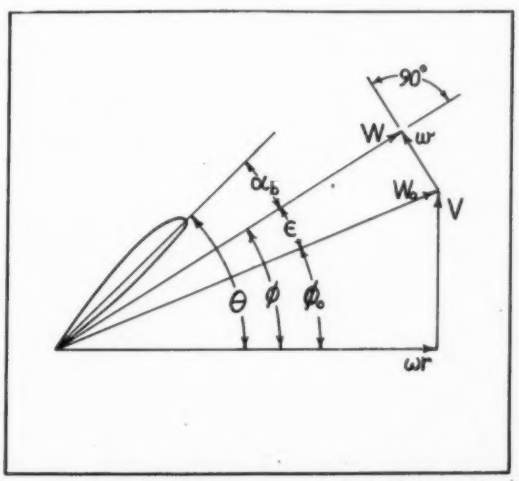

FIG. 13. Schematic diagram of a typical blade section in propeller operation. $\alpha = -90°$.

Then,

$$\frac{dC_T}{dx} = \frac{1}{(\rho/2)\ (\omega R)^2 \pi R^2} R \frac{dT}{dr} = \frac{R}{(\rho/2)\ (\omega R)^2\ \pi R^2} \times (\rho/2) W^2 bc(c_l \cos\phi - c_{d_0} \sin\phi)$$

$$= 8Fx^2\ (\tan\epsilon)\ \frac{\cot\phi - \tan k}{(\cot\phi + \tan\epsilon)^2} \qquad (10)$$

$$\frac{dC_P}{dx} = \frac{1}{(\rho/2)\ (\omega R)^3 \pi R^2} R \frac{dP}{dr} = \frac{R}{(\rho/2)\ (\omega R)^2 \pi R^3} \times (\rho/2)\ W^2 bcr\ (c_l \sin\phi + c_{d_0} \cos\phi)$$

$$= 8Fx^4\ (\tan\epsilon)\ \frac{1 + (\cot\phi)\ (\tan k)}{(\cot\phi + \tan\epsilon)^2} \qquad (11)$$

Using the above expressions, calculations were made for a range of blade radial stations and pitch angles, and a range of section angles of attack at each combination of radial station and pitch angle. Aerodynamic characteristics for the NACA 23018 blade section estimated from data of references 4, 5, and 6 are shown in Fig. 14. The accuracy of the method is not sufficient to justify consideration of Reynolds Number variation with section radius. A sample calculation is shown in Table 3. Results for each radial station were plotted as curves of C_T/σ and C_P/σ versus V/nD for constant θ.

Having a complete set of blade-element characteristics curves for blade stations $x = 0.15$, 0.30, 0.45, 0.60, 0.75, 0.85, and 0.95 and for the operating range of

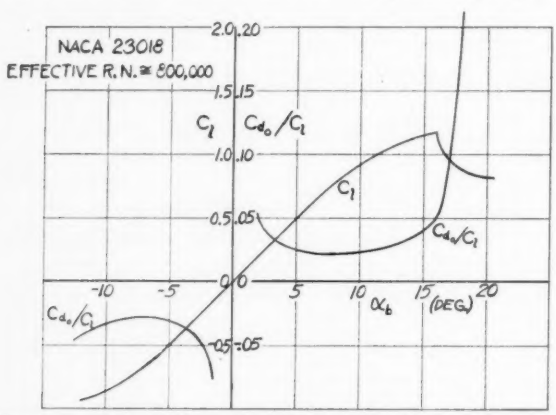

FIG. 14. Blade section characteristics used for propeller performance analysis.

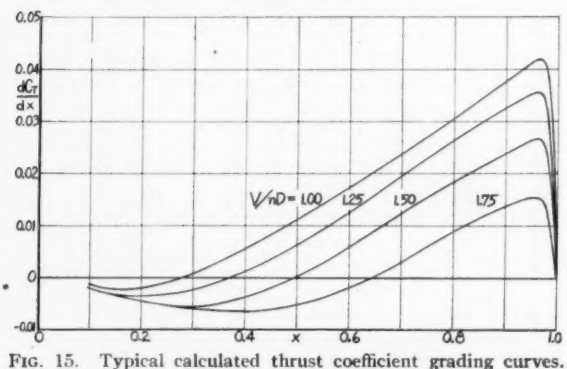

FIG. 15. Typical calculated thrust coefficient grading curves. $\theta_{(x=0.75)} = 39°$; $\theta_1 = -20°$; $\sigma = 0.04$.

TABLE 3
Sample Calculation of Blade Element Characteristics

(1) x	0.60
(2) θ (deg.)	45.0
(3) α_b (deg.) (assumed)	8.0
(4) c_l (Fig. 14)	0.77
(5) tan k (Fig. 14)	0.0230
(6) $\phi = \theta - \alpha_b$ (deg.) = (2) − (3)	37.0
(7) sin ϕ = sin (6)	0.602
(8) $F(b = 3)$ (from reference 2)	0.770
(9) σ	0.040
(10) tan $\epsilon = \sigma c_l/8xF \sin\phi$ = (9) (4)/8(1) (7)	0.01384
(11) ϵ (deg.) = 57.3 (10)	0.79
(12) $\phi_0 = \phi - \epsilon$ (deg.) = (6) − (11)	36.21
(13) $V/nD = \pi x(\tan\phi_0) = \pi$ (1) tan(12)	1.381
(14) cot ϕ = cot (6)	1.327
(15) cot ϕ − tan k = (14) − (5)	1.304
(16) $(\cot\phi + \tan\epsilon)^2 = [(14) + (10)]^2$	1.800
(17) $8Fx^2 \tan\epsilon = 8(8)\ (1)^2\ (10)$	0.01840
(18) dC_T/dx = (17) (15)/(16)	0.01333
(19) $1 + (\cot\phi)\ (\tan k) = 1 + (14)\ (5)$	1.0305
(20) $8Fx^4 \tan\epsilon = 8(8)\ (1)^4\ (10)$	0.01105
(21) dC_P/dx = (20) (19)/(16)	0.00642

section pitch angles, thrust and torque coefficient grading curves were constructed for the desired pitch settings and blade twist distributions at intervals of advance ratio to provide comparisons with the model test data. A typical set of these grading curves is shown in Fig. 15. The areas under the grading curves correspond to the thrust or torque coefficients for their respective operating conditions.

Comparisons of calculated and test results are shown in Figs. 6, 10, 11, and 12. These have been discussed previously.

EFFECT OF GRAVITY ON A LAG-HINGED ROTOR IN PROPELLER OPERATION

Introduction

In the case of a rotor with lag hinges operating as a propeller with rotor axis horizontal, the alternating gravity force on each blade may be expected to produce a blade motion response. The following analysis investigates this blade motion and the resulting forces on the hub.

Assumptions

The following simplifying assumptions are made:

(a) γ is a small angle, and γ^2 terms are negligible compared to γ terms.

(b) For purposes of this analysis, blade aerodynamic forces may be neglected, since, because of symmetry of the operating condition, such forces are essentially constant.

(c) The rotor hub rotates at constant angular velocity.

(d) The effect of lag motion damping may be neglected in considering the limiting case.

Blade Lag Motion

Fig. 16 shows a front view of one blade and rotor hub in propeller operation. The blade lag motion is

analyzed with respect to coordinates rotating with the hub. Centripetal acceleration is then replaced by a centrifugal force given by

$$F_c = (W_b/g)\,\omega^2 R(e_2 + L_1) \tag{12}$$

plus Coriolis terms containing γ which become negligible in Eq. (13) since they are of γ^2 order. The equation for angular motion about the lag hinge is

$$I_2\frac{d^2\gamma}{dt^2} = -F_c L_2 R\,\frac{\gamma e_2 R}{e_2 R + L_2 R} - W_b L_1 R \sin(\psi - \gamma) =$$

$$-W_b\left[\frac{\omega^2 R^2}{g}\,e_2 L_2\,\frac{e_2 + L_1}{e_2 + L_2}\,\gamma + L_1 R(\sin\psi - \gamma\cos\psi)\right] \tag{13}$$

Assume that the blade lag motion is given by

$$\gamma = A_1\cos\psi + B_1\sin\psi + A_2\cos 2\psi + B_2\sin 2\psi \tag{14}$$

Substituting Eq. (14) in Eq. (13) yields

$$0 = K_2A_1 + \cos\psi\,(K_1A_1 + K_2A_2) + \sin\psi\,[K_1B_1 + K_2(B_2 - 2)] + \cos 2\psi\,(K_1A_2 + 3I_2A_2 + K_2A_1) + \sin 2\psi(K_1B_2 + 3I_2B_2 + K_2B_1) + \cos 3\psi\,(K_2A_2 + \ldots) + \sin 3\psi(K_2B_2 + \ldots) \tag{15}$$

Equating coefficients of the constant, $\sin\psi$, $\cos\psi$, and $\sin 2\psi$ terms to zero (since there are only four unknowns, only four of the seven possible simultaneous equations are solved, and these are selected under the assumption that the higher harmonics will prove to be relatively unimportant),

$$A_1 = 0 \text{ (since } K_2 \text{ is not, in general, zero)} \tag{16}$$

$$A_2 = 0 \text{ (since } K_2 \text{ is not, in general, zero)} \tag{17}$$

$$B_1 = (K_2/K_1)\,(2 - B_2) \tag{18}$$

$$B_1 = -B_2(K_1 + 3I_2)/K_2 \tag{19}$$

Solving for B_2,

$$B_2 = 2/[1 - K_1(K_1 + 3I_2)/K_2^2] \tag{20}$$

Motion of Blade Center of Gravity

Referring to Fig. 13, the motion of the blade center of gravity in fixed coordinates is derived as follows:

$$y = e_2R\sin\psi + L_1R\sin(\psi - \gamma)$$
$$\cong R[e_2\sin\psi + L_1(\sin\psi - \gamma\cos\psi)] \tag{21}$$

$$z = e_2R\cos\psi + L_1R\cos(\psi - \gamma)$$
$$\cong R[e_2\cos\psi + L_1(\cos\psi + \gamma\sin\psi) \tag{22}$$

Substituting $\gamma = B_1\sin\psi + B_2\sin 2\psi$ and differentiating twice,

$$\frac{d^2y}{dt^2} = \omega^2R\{\sin\psi[-e_2 - L_1 + (1/2)L_1B_2] + \sin 2\psi(2L_1B_1) + \sin 3\psi\,[(9/2)L_1B_2]\} \tag{23}$$

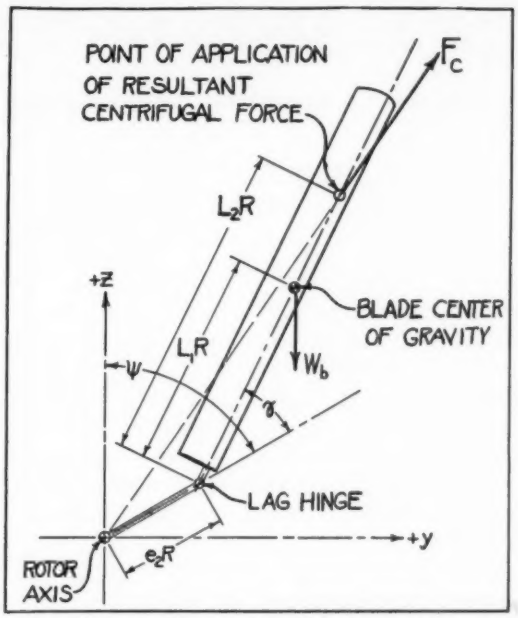

FIG. 16. Schematic diagram of lag-hinged rotor blade in propeller operation.

$$\frac{d^2z}{dt^2} = \omega^2R\{\cos\psi[-e_2 - L_1 - (1/2)L_1B_2] + \cos 2\psi\,[2L_1B_1] + \cos 3\psi[(9/2)L_1B_2]\} \tag{24}$$

Hub Loads Due to Gravity

The equations of linear motion of the blade center of gravity are

$$F_{z_1} - W_b = (W_b/g)(d^2z/dt^2) \tag{25}$$

$$F_{y_1} = (W_b/g)(d^2y/dt^2) \tag{26}$$

where the vertical force exerted by one blade on the hub at the lag hinge is F_{z_1} and the horizontal force is F_{y_1}. Substituting Eqs. (23) and (24).

$$F_{z_1} = W_b\,(1 + (\omega^2R/g)\{\cos\psi[-e_2 - L_1 - (1/2)L_1B_2] + \cos 2\psi(2L_1B_1) + \cos 3\psi[(9/2)L_1B_2]\}) \tag{25a}$$

$$F_{y_1} = (W_b\omega^2R/g)\{\sin\psi[-e_2 - L_1 + (1/2)L_1B_2] + \sin 2\psi(2L_1B_1) + \sin 3\psi[(9/2)L_1B_2]\} \tag{26a}$$

For a three-bladed rotor, the total instantaneous blade reactions on the hub are

$$F_z = F_{z_1} + F_{z_2} + F_{z_3} \tag{27}$$

$$F_y = F_{y_1} + F_{y_2} + F_{y_3} \tag{28}$$

where the value of ψ for each of the three blades may be expressed in terms of ψ for the first blade as

$$\psi_1 = \psi;\quad \psi_2 = \psi + (2\pi/3);\quad \psi_3 = \psi + (4\pi/3)$$

Making these substitutions,

$$F_z = \frac{27}{2}\,\frac{W_b\omega^2L_1R}{g}\,B_2\cos 3\psi + 3W_b \tag{29}$$

$$F_y = \frac{27}{2}\frac{W_b\omega^2 L_1 R}{g} B_2 \sin 3\psi \qquad (30)$$

By an analogous process for the case of a two-bladed rotor,

$$F_z = \frac{4W_b\omega^2 L_1 R}{g} B_1 \cos 2\psi + 2W_b \qquad (31)$$

$$F_y = \frac{4W_b\omega^2 L_1 R}{g} B_1 \sin 2\psi \qquad (32)$$

In the case of a three-bladed rotor, the force transmitted to the hub by the blades in propeller operation (aside from a steady vertical force equal to total blade weight) is a third harmonic vibratory force arising from the second harmonic lag motion. In the case of a two-bladed rotor, the transmitted force is a second harmonic vibratory force arising from the first harmonic lag motion.

Numerical Examples for Typical Rotors

The foregoing analysis has been applied to four typical rotors, selected to represent extremes of size and operating at low rotation speed (found to be more critical in the case of three-bladed rotors) to represent propeller operation. Results are summarized in Table 4. In the case of the three-bladed rotors, the vibratory hub loads are negligibly low compared to total blade weight, while in the case of the two-bladed rotors the vibratory hub loads are dangerously high. These results indicate that a three-bladed rotor with lag hinges should be satisfactory from the standpoint of gravity-induced vibratory hub loads; however, for a two-bladed rotor, a semirigid or rigid-type rotor would be required to avoid objectionable vibratory loads induced by gravity.

TABLE 4

Rotor diameter (ft.)	16.5	16.5	72.0	72.0
Number of blades	3	2	3	2
Weight of one blade (lbs.)	10	15	200	300
Rotor speed (rad. per sec.)	32	32	8.2	8.2
B_1 (rad. times 10^{-3})	7.75	7.75	57.7	57.7
B_2 (rad. times 10^{-6})	−6.50	−6.50	−223.0	−223.0
Vibratory hub load resultant amplitude (lbs.)	0.15	77.2	23.9	2745.

REFERENCES

[1] Reid, E. G., *Studies of Blade Shank Form and Pitch Distribution for Constant-Speed Propellers*, N.A.C.A. T.N. No. 947, January, 1945.

[2] Lock, C. N. H., and Yeatman, D., *Tables for Use in an Improved Method of Airscrew Strip Theory Calculation*, R. & M. 1674, 1934.

[3] Crigler, John L., *Comparison of Calculated and Experimental Propeller Characteristics for Four-, Six-, and Eight-Blade Single-Rotating Propellers*, N.A.C.A. Wartime Report No. L-362, 1944.

[4] Jacobs, E. N., and Abbott, I. A., *Airfoil Section Data Obtained in the N.A.C.A. Variable-Density Tunnel as Affected by Support Interference and Other Corrections*, N.A.C.A. Report No. 669, 1939.

[5] Jacobs, E. N., and Sherman, Albert, *Airfoil Section Characteristics as Affected by Variations of the Reynolds Number*, N.A.C.A. Report No. 586, 1939.

[6] Abbott, I. H., von Doenhoff, A. E., and Stivers, L. S., Jr., *Summary of Airfoil Data*, N.A.C.A. Wartime Report No. L-560, 1945.

[7] Hamlin, C. J., Jr., *Convertoplane Model Flight Tests*, Bell Aircraft Corporation Report No. 30-929-002, 1944.

[8] Lichten, R. L., *Helicopter Performance*, Journal of the Aeronautical Sciences, Vol. 13, No. 7, pp. 353–362, July, 1946.

[9] Barnaby, R. S., Berkowitz, S. M., and Colcord, W. H., *Convertible Aircraft*, Aeronautical Engineering Review, Vol. 8, No. 4, pp. 20–25, April, 1949.

Changes of Address

Since the Post Office Department does not as a rule forward magazines to forwarding addresses it is important that the Institute be notified of changes in address 30 days in advance of publishing date to ensure receipt of every issue of the JOURNAL and REVIEW.

Notices should be sent directly to:

Institute of the Aeronautical Sciences, Inc.
2 East 64th Street, New York 21, New York

Matrix Solution of the n-Section Column

WILLIAM T. THOMSON*
University of Wisconsin

SUMMARY

A procedure is developed for the determination of the critical load of a column of n different sections under any end conditions. When n is a small number, the method leads to simple analytic expressions for the critical load.

NOMENCLATURE

l_i	=	length of ith section
E_iI_i	=	stiffness of ith section
x_i	=	x coordinate at the end of the ith section
y_i	=	deflection at the end of the ith section
y_i'	=	slope at the end of the ith section
β_i	=	$\sqrt{P/E_iI_i}$
E	=	Young's modulus of elasticity
P	=	column load
l	=	total length of column
M_0, M_n	=	moment at ends of the column

DEVELOPMENT OF EQUATIONS

FIG. 1 SHOWS A COLUMN of n sections with arbitrary end conditions. The column is assumed to be long so that failure tends to take place by lateral instability rather than by direct compression.

From the free-body diagram of the ith section shown in Fig. 2, the differential equation for this section becomes:

$$E_iI_i(d^2y/dx^2) = -P(y - y_{i-1}) + M_{i-1} \quad (1)$$

Employing the method of Laplace transformation, the solution for the deflection at i can be written in terms of quantities at $i - 1$ as

$$y_i = y_{i-1} + y_{i-1}' \frac{\sin \beta_i l_i}{\beta_i} + \frac{M_{i-1}}{E_iI_i\beta_i^2}(1 - \cos \beta_i l_i) \quad (2)$$

Differentiating, the slope and moment equations are obtained:

$$y_i' = y_{i-1}' \cos \beta_i l_i + \frac{M_{i-1}}{E_iI_i\beta_i} \sin \beta_i l_i \quad (3)$$

$$M_i = -y_{i-1}'E_iI_i\beta_i \sin \beta_i l_i + M_{i-1} \cos \beta_i l_i \quad (4)$$

Expressed in matrix form, Eqs. (2), (3), and (4) are represented as follows:

$$\begin{bmatrix} y_i \\ y_i' \\ M_i \end{bmatrix} = \begin{bmatrix} 1 & (1/\beta_i) \sin \beta_i l_i & (1/E_iI_i\beta_i^2)(1 - \cos \beta_i l_i) \\ 0 & \cos \beta_i l_i & (1/E_iI_i\beta_i) \sin \beta_i l_i \\ 0 & -E_iI_i\beta_i \sin \beta_i l_i & \cos \beta_i l_i \end{bmatrix} \begin{bmatrix} y_{i-1} \\ y_{i-1}' \\ M_{i-1} \end{bmatrix} \quad (5)$$

It is evident then that by repeated multiplication of the square matrix the quantities at n can be expressed in terms of corresponding quantities at 0 by an equation of the form:

$$\begin{bmatrix} y_n \\ y_n' \\ M_n \end{bmatrix} = \begin{bmatrix} A_{11} & A_{12} & A_{13} \\ 0 & A_{22} & A_{23} \\ 0 & A_{32} & A_{33} \end{bmatrix} \begin{bmatrix} y_0 \\ y_0' \\ M_0 \end{bmatrix} \quad (6)$$

Knowing the end conditions, the equation for the critical load is readily determined from Eq. (6) as follows:

(1) *Pin-ended columns:*

$$y_n = y_0 = M_n = M_0 = 0$$

Therefore,

$$A_{12} = A_{32} = 0 \quad (7)$$

(2) *Fixed-end columns:*

$$y_n = y_0 = y_n' = y_0' = 0$$

Therefore,

$$A_{13} = A_{23} = 0 \quad (8)$$

(3) *End 0 fixed and end n pinned and free:*

$$y_0 = y_0' = M_n = 0$$

Therefore,

$$A_{33} = 0 \quad (9)$$

In interpreting Eqs. (7) to (9), when two of the matrix elements are equated to zero, only roots satisfying both equations represent the true solution.

PROCEDURE FOR COMPUTATION

The matrix elements of Eq. (6) are obtained by multiplying the n square matrices of Eq. (5). When n is a large number, it is simpler to carry out this computation numerically as follows: Choose a value for β_n, and determine

Received April 4, 1949.
* Associate Professor of Mechanics.

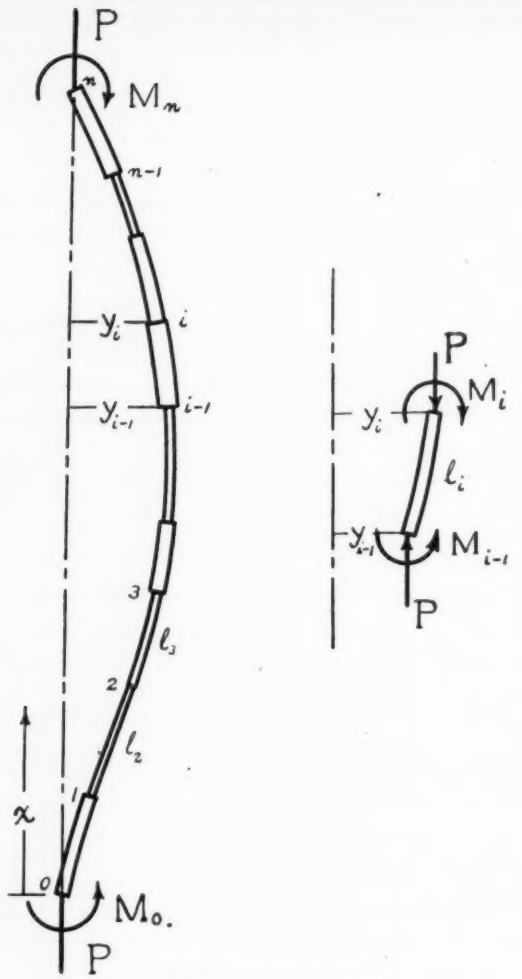

FIG. 1 (*left*) and FIG. 2 (*right*).

$$\beta_{n-1} = \beta_n \sqrt{\frac{E_n I_n}{E_{n-1} I_{n-1}}}, \qquad \beta_{n-2} = \beta_n \sqrt{\frac{E_n I_n}{E_{n-2} I_{n-2}}}$$

etc. Compute the elements of the square matrix of Eq. (5) for each section, and multiply out to obtain the elements of Eq. (6). Plotting Eqs. (7), (8), or (9) as function of β_n, the critical load is determined from the particular values of β_n where the curve goes to zero.

When n is a small number, simple analytical expressions can be obtained for the critical load. Some of these are given in the following section. The case for $n = 1$ is included since these equations are well known.

Analytical Expressions for Small n

The end conditions are designated as (1), (2), and (3) to conform to Eqs. (7), (8), and (9).

For $n = 1.0$: Case (1),

$$\sin \beta l = 0, \quad \beta l = \sqrt{P/EI}\, l = \pi$$

Therefore,

$$P_{cr} = \pi^2 EI/l^2 \tag{10}$$

Case (2),

$$(1 - \cos \beta l) = \sin \beta l = 0, \ \beta l = 2\pi$$

Therefore,

$$P_{cr} = 4\pi^2 EI/l^2 \tag{11}$$

Case (3),

$$\cos \beta l = 0, \quad \beta l = \pi/2$$

Therefore,

$$P_{cr} = \pi^2 EI/4l^2 \tag{12}$$

For $n = 2$: Case (1),

$$\frac{\sin \beta_1 l_1}{\beta_1} + \frac{\sin \beta_2 l_2}{\beta_2} \cos \beta_1 l_1 - (1 - \cos \beta_2 l_2) \frac{\sin \beta_1 l_1}{\beta_1} = 0$$

$$- \frac{\sin \beta_2 l_2}{\beta_2} \cos \beta_1 l_1 - \frac{\sin \beta_1 l_1}{\beta_1} \cos \beta_2 l_2 = 0$$

Therefore,

$$\tan \beta_2 l_2 = -(\beta_2/\beta_1) \tan \beta_1 l_1 \tag{13}$$

Case (2),

$$\left.\begin{aligned} 1 - \cos \beta_1 l_1 \cos \beta_2 l_2 + (\beta_1/\beta_2) \sin \beta_1 l_1 \sin \beta_2 l_2 = 0 \\ \beta_1 \cos \beta_2 l_2 \sin \beta_1 l_1 + \beta_2 \sin \beta_2 l_2 \cos \beta_1 l_1 = 0 \end{aligned}\right\} \tag{14}$$

Case (3),

$$-(\beta_1/\beta_2) \sin \beta_1 l_1 \sin \beta_2 l_2 + \cos \beta_1 l_1 \cos \beta_2 l_2 = 0 \tag{15}$$

For $n = 3$: (Case (1),

$$\frac{\tan \beta_3 l_3}{\beta_3} = -\left\{ \frac{\dfrac{\tan \beta_1 l_1}{\beta_1} + \dfrac{\tan \beta_2 l_2}{\beta_2}}{1 - \dfrac{\beta_2}{\beta_1} \tan \beta_1 l_1 \tan \beta_2 l_2} \right\} \tag{16}$$

Case (3),

$$-(\beta_1/\beta_2) \tan \beta_2 l_2 \tan \beta_1 l_1 + 1 = 0 \tag{17}$$

The correctness of these equations can be easily verified by letting $\beta_1 = \beta_2 = \beta_3 =$ etc. $l_1 = l_2 = l_3 \ldots = l/n$ in which case the results reduce to that of $n = 1$.

Conclusion

A matrix method is developed by which the critical load of an n-section column can be determined for any end conditions. For n a small number the results reduce to simple equations for the critical load.

Bibliography

Thomson, W. T., *Critical Load of Columns of Varying Cross Section*, A.S.M.E. Paper No. 49-A1 presented at Semi-Annual Meeting of A.S.M.E., San Francisco, June, 1949, and to be published in the *Journal of Applied Mechanics*.

A Modification of the Holzer Method for Computing Uncoupled Torsion and Bending Modes

HENRY E. FETTIS*
Air Materiel Command

SUMMARY

The present method is an adaptation of the well-known process devised by Holzer for solving the differential equations of beam vibrations. Several versions of this method are now in common use; the original form is described in references 1 and 2 and is usually employed in computing the torsional modes of vibration of a bar carrying a series of concentrated discs. Similar processes were devised by Myklestad[5] and Bellin[6] for bending modes, and recently an extension of the above principle to the computation of coupled modes has been published.[4] All of the above methods have in common the feature that a value of the frequency is assumed and a deflection computed which satisfies all but one of the required end conditions. Although the same principle forms the basis for the following method, the system of numerical integration employed makes the method better suited to configurations with continuous mass and stiffness distributions. The process is set up in such a manner as to be easily adapted to routine calculation by a semiskilled computer and the correctness of the results may be verified at each station. All of the features that make the Holzer method practical are retained, and some new techniques not in common practice are introduced.

(I) FORMULATION OF THE METHOD

(I) *Torsional Modes of Vibration*

THE DIFFERENTIAL EQUATION to be solved is:

$$(d/dx)GJ(d\theta/dx) = -I\omega^2\theta \qquad (1)$$

where θ is the angular deflection in radians in a normal mode of vibration, ω is the frequency in radians per second, GJ is the torsional stiffness in pound feet^2, I is the mass moment of inertia per unit span about the torsion axis in pound seconds^2, and x is the spanwise coordinate in feet measured positive to the right along the torsion axis.

Eq. (1) may be written in integrated form as two simultaneous equations:

$$\left.\begin{aligned} GJ_{n+1}\theta_{n+1}' - GJ_n\theta_n' &= -\omega^2\int_{X_n}^{X_{n+1}} I\theta\,dx \\ \theta_{n+1} - \theta_n &= \int_{X_n}^{X_{n+1}} \theta'dx \end{aligned}\right\} \qquad (2)$$

in which subscripts indicate the value of the variables at any two points x_n and x_{n+1} on the span $(x_n < x_{n+1})$ and primes denote differentiation with respect to x. If the interval

$$\Delta x_n = x_{n+1} - x_n$$

is small, the integrals may be approximated by the trapezoidal rule, and Eqs. (2) become

$$\left.\begin{aligned} GJ_{n+1}\theta_{n+1}' - GJ_n\theta_n' &= -\omega^2\left(\frac{\Delta x_n}{2}\right)\times \\ &\qquad (I_{n+1}\theta_{n+1} + I_n\theta_n) \qquad (3a) \\ \theta_{n+1} - \theta_n &= \left(\frac{\Delta x_n}{2}\right)(\theta_{n+1}' + \theta_n') \qquad (3b) \end{aligned}\right\}$$

θ_{n+1}' may now be eliminated between Eqs. (3a) and (3b), giving a simple linear relation between the deflection at any point (or "station") and the deflection and slope at a preceding point:

$$\theta_{n+1}\left[GJ_{n+1} + \omega^2\left(\frac{\Delta x_n}{2}\right)^2 I_{n+1}\right] =$$
$$\theta_n\left[GJ_{n+1} - \omega^2\left(\frac{\Delta x_n}{2}\right)^2 I_n\right] + (GJ_{n+1} + GJ_n)\times$$
$$\theta_n'\left(\frac{\Delta x_n}{2}\right) \qquad (4a)$$

The slope at the advance point may then be found by rewriting Eq. (3b) in the form:

$$\theta_{n+1}' = (2/\Delta x_n)(\theta_{n+1} - \theta_n) - \theta_n' \qquad (4b)$$

Eqs. (4a) and (4b) may be employed to compute a normal mode of vibration according to the usual Holzer scheme by assuming a value for the frequency ω and starting the solution at one end of the beam where either the deflection or slope or a linear relation between them is known. These initial values are determined by the end conditions; from physical considerations, the following end conditions will apply:

At a free end carrying no concentrated mass,

$$GJ(\theta') = 0 \qquad (5)$$

At a fixed end,

$$\theta = 0 \qquad (6)$$

At a free end carrying a concentrated item of mass moment of inertia $\bar{I}$,†

$$GJ(\theta') = -\omega^2\bar{I}\theta \qquad (7)$$

Received March 11, 1949.

* Mathematician, Dynamics Branch, Aircraft Laboratory.

† The bar over the letter I is here employed to distinguish between a concentrated moment of inertia and a distributed inertia as in Eq. (1).

and sign being plus or minus according to whether the end is the right or left one.*

(2) *Bending Modes*

In this case the differential equation is:

$$(d^2/dx^2)EI(d^2h/dx^2) = \mu\omega^2 h \tag{8}$$

in which h is the deflection in feet, μ is the mass per unit length in pound feet^{-2} seconds^2, EI is the bending stiffness in pound feet^2, and ω is the frequency in seconds^{-1}. Eq. (8) may be written in integrated form as four simultaneous equations:

$$\begin{cases} F_{n+1} - F_n = \omega^2 \int_{X_n}^{X_{n+1}} \mu h \, dx & (9a) \\ M_{n+1} - M_n = \int_{X_n}^{X_{n+1}} F \, dx & (9b) \\ p_{n+1} - p_n = \int_{X_n}^{X_{n+1}} (M/EI) dx & (9c) \\ h_{n+1} - h_n = \int_{X_n}^{X_{n+1}} p \, dx & (9d) \end{cases}$$

which, when the integrals are approximated by the trapezoidal rule and the quantities F_{n+1}, M_{n+1}, and p_{n+1} eliminated, give the following relation between the deflection, h_{n+1}, at any station and the deflection h_n, slope p_n, shear F_n, and bending moment M_n at the preceding station:

$$h_{n+1}\left[EI_{n+1} - \omega^2\left(\frac{\Delta x_n}{2}\right)^4 \mu_{n+1}\right] = h_n\left[EI_{n+1} + \omega^2\left(\frac{\Delta x_n}{2}\right)^4 \mu_n\right] + 2p_n\left(\frac{\Delta x_n}{2}\right)EI_{n+1} + \frac{M_n}{EI_n}\left(\frac{\Delta x_n}{2}\right)^2 [EI_{n+1} + EI_n] + 2F_n\left(\frac{\Delta x_n}{2}\right)^3 \tag{10a}$$

Advance values of p, M, and F are then found by rearranging Eqs. (9b), (9c), (9d):

$$\begin{cases} p_{n+1}\left(\frac{\Delta x_n}{2}\right) = [h_{n+1} - h_n] - p_n\left(\frac{\Delta x_n}{2}\right) & (10b) \\ \frac{M_{n+1}}{EI_{n+1}}\left(\frac{\Delta x_n}{2}\right)^2 = [p_{n+1} - p_n]\left(\frac{\Delta x_n}{2}\right) - \frac{M_n}{EI_n} & (10c) \\ F_{n+1}\left(\frac{\Delta x_n}{2}\right)^3 = [M_{n+1} - M_n]\left(\frac{\Delta x_n}{2}\right)^2 - F_n\left(\frac{\Delta x_n}{2}\right)^3 & (10d) \end{cases}$$

From these equations, the four quantities h, p, F, and M may be computed when their values at a preceding station are known. To start the solution, use is made of the boundary conditions at one end appropriate to the physical conditions of the problem. End conditions applying in conventional cases are as follows:

* This sign convention holds as long as x is measured positive to the right.

At a free end carrying no concentrated mass,

$$\begin{cases} EIh'' = 0 & (11a) \\ (EIh'')' = 0 & (11b) \end{cases}$$

At a clamped (built-in) end,

$$\begin{cases} h = 0 & (12a) \\ h' = 0 & (12b) \end{cases}$$

At a simply supported (hinged) end, with no concentrated moment,

$$\begin{cases} h = 0 & (13a) \\ (EIh'') = 0 & (13b) \end{cases}$$

At a free end carrying a concentrated item of mass $\bar{m}$ and mass moment of inertia about a chordwise axis (rotary or bending inertia) equal to $\bar{I}$,

$$\begin{cases} \pm(EIh'') = -\omega^2 \bar{I} h' & (14a) \\ \pm(EIh'')' = \omega^2 \bar{m} h & (14b) \end{cases}$$

the sign being plus or minus according to whether the end is the left or right one.†

At a hinged end with a concentrated item of rotary inertia $\bar{I}$,

$$\begin{cases} h = 0 & (15a) \\ \pm(EIh'') = -\omega^2 \bar{I} h' & (15b) \end{cases}$$

The problem in the bending case is complicated by the fact that two of the four variables must be made arbitrary at the start of the process. Thus, each successive value of the deflection slope, moment, and shear must be written as a linear combination of the two arbitrary initial values.

Details of the two above processes are worked out and exemplified in Section (III).

(II) Application to Aircraft Wings: Advantage over Other Commonly Used Methods

The modes of vibration of aircraft wings may evidently be approximated by the modes of a free-free beam carrying a concentrated load at the center. It is simpler, however, to consider only the semiwing from the centerline outward and to divide the problem into the two cases of vibrations that are symmetric with respect to the aircraft plane of symmetry and vibrations that are symmetric with respect to the centerline. The first type are commonly referred to as "symmetric" and the latter as "antisymmetric" modes of vibration.

The end conditions summarized in Section (1) are applicable to the present problem with only slight modifications. Thus, at the wing tip, conditions (5) or (7) apply for torsional modes, while Eq. (11) or Eq. (14) is used in the bending case. At the airplane centerline, condition (6) holds if the torsion is antisymmetric, and condition (7) holds if the mode is symmetric torsion. In the latter case, $\bar{I}$ is to be interpreted as half the moment of inertia of the fuselage in pitch. For antisymmetric bending, the appropriate conditions are

† See footnote * on this page.

(15) with $\bar{I}$ replaced by half the moment inertia of the fuselage in roll, while for symmetric modes the conditions become

$$\begin{cases} h' = 0 & (16a) \\ (EIh'')' = -\bar{m}\omega^2 h & (16b) \end{cases}$$

where $\bar{m}$ is half the mass of the fuselage.

One of the principal advantages of the Holzer method lies in the fact that higher modes may be computed without reference to the lower ones and that, by choosing the point $x = 0$ at the wing tip, both the symmetric and antisymmetric cases may be handled simultaneously, since the two cases are distinguished only by the boundary conditions at the center. Other methods require separate treatment in the two instances, and little or none of the information obtained from one can be used in the other.

An additional advantage gained by the present treatment of the problem lies in the fact that discontinuities in the basic parameters which frequently occur, due to structural changes, cutouts, or large concentrated masses at inboard points, are more easily accounted for provided the stations are so selected that they coincide with any discontinuities that may exist. Consider, for example, the case where the torsional rigidity changes suddenly at some point, x_k. At the point, GJ is two-valued, having the value $(GJ_k)_L$ when approached from the left or outboard side and the value $(GJ_k)_R$ when approached from the right or inboard side. Since the torque across this section must remain continuous, it follows that (θ') must also make a finite jump at the point. The slope on the left side is found from the usual equations, viz.,

$$(\theta_k')_L\left(\frac{\Delta x_{k-1}}{2}\right) = [\theta_k - \theta_{k-1}] - (\theta_{k-1}')\left(\frac{\Delta x_{k-1}}{2}\right) \tag{17}$$

whereas the slope on the right will be determined from the condition of continuity of torque—namely,

$$(GJ_k)_L(\theta_k')_L = (GJ_k)_R(\theta_k')_R \tag{18}$$

The angular displacement remains continuous at the point, and so the advance value of θ is given by

$$\theta_{k+1}\left[GJ_{k+1} + \omega^2\left(\frac{\Delta x_k}{2}\right)^2 I_{k+1}\right] = \theta_k\left[GJ_{k+1} - \omega^2\left(\frac{\Delta x_k}{2}\right)^2 I_k\right] + [(GJ_k)_R + GJ_{k+1}](\theta_k')_R\left(\frac{\Delta x_k}{2}\right) \tag{19}$$

A similar situation occurs when a concentrated mass is located at an inboard point. In this case, the torque, and therefore the slope, is discontinuous and the slopes on either side of the point are related by the equation

$$GJ_k[(\theta_k')_L - (\theta_k')_R] = \bar{I}\omega^2\theta_k \tag{20}$$

where $\bar{I}$ is the mass moment of inertia of the concentrated item. Eq. (7) may be regarded as a special case of Eq. (20), since then either $(\theta_k')_L$ or $(\theta_k')_R$ is zero, depending on whether the end is the left or right one.

In the event that the distributed inertia of the wing is discontinuous, a different value of I must be used when computing the displacement at the discontinuity than is used when proceeding from this point to the next one. However, no discontinuity in either angular displacement or slope will result in this case (cf. Example 1, Section IV).

Analogous situations to the above in the bending case may be disposed of in a similar manner. Thus the presence of a concentrated item of mass $\bar{m}$ and rotary inertia $\bar{I}$ produces a discontinuity in both shear and bending moment, such that

$$\begin{cases} (F_k)_L - (F_k)_R = -\bar{m}\omega^2 h_k \\ (M_k)_L - (M_k)_R = \bar{I}\omega^2 p_k \end{cases} \tag{21}$$

with the slope, p, and displacement, h, remaining continuous. Eqs. (21) include Eqs. (14) as a special case where either F_L and M_L or F_R and M_R are zero.

The present scheme is also useful when the effect of the variation of the mass or inertia of some concentrated item is desired. Since the mass (or inertia) of such items enters linearly into the equations, either by virtue of the end conditions or the conditions of continuity, it follows that the deflections, slopes, etc., at all points inboard of the concentrated item will be linear functions of the mass or inertia. Introduction of this additional variable into the problem permits the end conditions at the centerline to be satisfied for any assumed frequency. Thus, in the torsion case, the end condition at the center may be satisfied by proper choice of the inertia of some concentrated item, while in the bending case the two conditions at the center will result in two simultaneous equations involving the mass and the arbitrary tip slope. As a special case, the centerline condition for symmetric torsion may be satisfied by proper choice of the inertia at the center. Similarly, for bending modes, the mass or inertia at the center may be employed as an auxiliary variable. For certain frequencies, negative or infinite masses may result. The negative values may be interpreted as effective masses due to flexibility [cf. Eqs. (25), (31)], while infinite values indicate a node at the point of attachment of the mass.

(III) Tabular Form for Routine Computations

(I) *Symmetric and Antisymmetric Torsion*

(*a*) *Tabular Form.*—See Table 1.

(*b*) *Outline of Procedure.*—Columns (7) and (10) are first computed from the basic data listed in columns (2) and (3). Columns (5) and (8) are then computed for an assumed value of the frequency, ω.

TABLE 1

Tabular Form for Torsional Computations

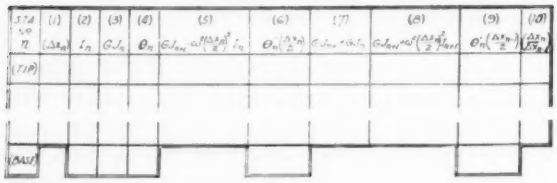

TABLE 2

Tabular Form for Bending Computations

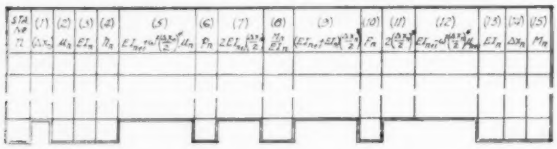

The initial value in column (6) is obtained from the boundary condition at the free end—namely,

$$(GJ_0)(\theta_0') = -\bar{I}_t\omega^2\theta_0 \tag{22}$$

where $\bar{I}_t$ is the mass moment of inertia about the torsion axis of the concentrated item at the tip.

The initial value in column (4) [and therefore θ_0 in Eq. (22)] is arbitrary and may be taken as unity.

Succeeding values for columns (4), (9), and (6) are obtained from the expressions:

$$\left.\begin{aligned}(4)_{n+1} &= [(4)_n \times (5)_n + (6)_n \times (7)_n]/(8)_n \\ (9)_{n+1} &= [(4)_{n+1} - (4)_n] - (6)_n \\ (6)_{n+1} &= (9)_{n+1} \times (10)_{n+1}\end{aligned}\right\} \tag{23}$$

continuing until the deflection and slope at the centerline (base) have been found. At the base, the correctness of the assumed frequency is determined from the condition

$$\theta_b = 0 \tag{24a}$$

for antisymmetric modes, and the condition

$$\bar{I}_b\omega^2\theta_b = (GJ_b)(\theta_b') \tag{24b}$$

for symmetric modes. If one or the other of these conditions is not satisfied, the process is repeated using a new assumed frequency. After several trials, a plot of the base values, Eqs. (24a) and (24b), as a function of the assumed frequency indicates the location of the correct frequency (or frequencies). In the symmetric case, Eq. (24b) may be solved for $\bar{I}_b$, and the resulting value may be plotted as a function of the assumed frequency. The latter method enables one to obtain solutions corresponding to various loading conditions of the aircraft.

The tip inertia may also be used as an auxiliary variable. In this case, the initial value of column (6) is written as a factor times the inertia $\bar{I}_t$ of the tip item. Each succeeding value of θ and θ' then becomes a constant plus a second constant times $\bar{I}_t$. At the base, the equation for either the symmetric or antisymmetric mode may be solved for $\bar{I}_t$. Thus, any assumed frequency determines a unique value for the tip inertia in each mode, with the possible exception of those frequencies that cause the coefficient of $\bar{I}_t$ to vanish. Such a condition could be interpreted as corresponding to a fixed tip and would thus be of little interest in the present problem of aircraft wing vibration. However, in other cases of torsional vibration, this condition may also have practical significance.

The negative inertias that will result for a certain range of frequencies have meaning if flexibility of the tip item is allowed. In this case, the effective inertia acting at the tip may be shown to be

$$\bar{I}_t/[1 - (\omega/\omega_t)^2] \tag{25}$$

in which ω_t is the natural frequency of the item on its restraining spring.[3] The quantity defined by quantity (25) will evidently be negative if

$$\omega_t < \omega$$

that is, provided the spring is sufficiently weak.

In a manner similar to the one described above, the inertia of a concentrated item located at an inboard station may be used as an auxiliary variable.

(2) *Symmetric and Antisymmetric Bending*

(*a*) *Tabular Form.*—See Table 2.

(*b*) *Outline of Procedure.*—Columns (7), (9), (11), (13), and (14) are first computed from the basic data listed in columns (1), (2), and (3). Columns (5) and (12) are then computed for an assumed value of the frequency, ω.

The initial values in columns (8), (10), and (15) are obtained by making use of the boundary conditions at the tip—namely,

$$M_0 = -\bar{I}_t\omega^2 p_0, \quad F_0 = \bar{m}_t\omega^2 h_0$$

where $\bar{m}_t$ is the mass and $\bar{I}_t$ is the mass moment of inertia in bending of the tip item. The initial values in columns (4) and (6) are arbitrary, and one of them (usually h_0) may be set equal to unity. Each succeeding entry in columns (4), (6), (8), (10), and (15) thus consists of two parts: one depending on the initial displacement at the tip and the other on the initial tip angle. These successive entries are found by making use of Eqs. (10), viz.,

$$\left.\begin{aligned}(4)_{n+1} &= [(4)_n \times (5)_n + (6)_n \times (7)_n + (8)_n \times (9)_n + (10)_n \times (11)_n]/(12)_n \\ (6)_{n+1} &= (14)_{n+1} \times [(4)_{n+1} - (4)_n] - (6)_n \\ (8)_{n+1} &= (14)_{n+1} \times [(6)_{n+1} - (6)_n] - (8)_n \\ (15)_{n+1} &= (8)_{n+1} \times (13)_{n+1} \\ (10)_{n+1} &= (14)_{n+1} \times [(15)_{n+1} - (15)_n] - (10)_n\end{aligned}\right\} \tag{26}$$

($n = 0, 1, 2, \ldots$). At the base, the deflection, slope, moment, and shear are thus obtained in terms of the arbitrary tip deflection and arbitrary tip slope. The boundary conditions at the base may then be applied to determine the correctness of the assumed frequency. For symmetric bending, p_0 is determined in such a way as to give zero slope at the base, and the quantity

$$F_b + \bar{m}_b\omega^2 h_b \tag{27}$$

is evaluated. If the value of (27) is zero, the assumed frequency was the correct symmetric frequency. Since p_0 is known, the deflections at each station may be evaluated to give the corresponding mode shape. Similarly, for antisymmetric bending, p_0 is so determined that the deflection is zero at the base, and the quantity

$$M_b - \bar{I}_b\omega^2 p_b \tag{28}$$

is evaluated. If (28) is zero, the assumed frequency was the correct antisymmetric frequency, and the corresponding mode shape may then be evaluated. If neither (27) nor (28) is zero, the process is repeated with a new assumed value of the frequency. The correct frequency corresponding to each case may then be found graphically by plotting the values obtained for (27) and (28) as functions of the frequency. An alternative method is to determine the quantities $\bar{m}_b$ or $\bar{I}_b$ so as to make (27) or (28) zero. This method is useful when the mass at the base is subject to variation due to different loading conditions of the aircraft, etc.

The mass of a concentrated item at a point other than at the center may be introduced as a variable in the same manner as in the torsion case if rotary inertia is neglected. In this instance, all entries in columns (4), (6), (10), and (15) at points inboard of the item will contain an additional term due to the concentrated mass. The mass and the tip angle then become two unknowns that may be simultaneously determined so as to satisfy the boundary conditions at the center.

The torsional and bending computations are both greatly simplified if the stations are so selected that (Δx) is constant. For then, in the torsion case, column (9) becomes identical to (6), and column (10) is identically unity. In the bending case, column (6) may be replaced by $p_n(\Delta x/2)$; (7), by $2EI_{n+1}$; (8), by $(M_n/EI_n)(\Delta x/2)^2$; (9), by $(EI_{n+1} + EI_n)$; (10), by $F_n(\Delta x/2)^3$; and (15), by $M_n(\Delta x/2)^2$. Column (11) becomes identically 2 at all stations and may thus be dispensed with, while column (14) will no longer be needed.

The insertion of two additional columns in the torsion calculations and one additional column in the bending provides a positive check at each station on the correctness of the results. To check the torsion case, a column is added in which the torque is evaluated by means of the expression

$$T_n = (GJ_n)\theta_n'$$

TABLE 3

Tabular Arrangement of Torsional Stiffness and Mass Moment of Inertia Data

STA. NO.	$(LB.FT.^2)\times10^7$		$LB.SEC^2$		FT.	
n	GJ_n	GJ_{n+1}	I_n	I_{n+1}	Δx_n	
0	.278	.406	2.04	3.36	2.66667	WING TIP
1	.406	.545	3.36	4.56		
2	.545	.736	4.56	7.56		
3	.736	1.026	7.56	11.04		
4	1.026	1.472	6.72	10.80		
5	1.472	2.268	10.80	19.44		
6	2.268	—	19.44	—		AIRPLANE CENTERLINE
CONCENTRATED INERTIA AT CENTERLINE:			4200 LB.FT.SEC.^{2}		—	

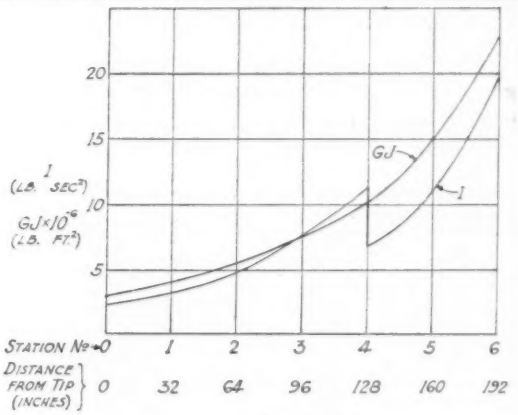

FIGURE 1

FIG. 1. Spanwise distribution of mass moment of inertia and torsional stiffness.

and a second where the torque is evaluated from

$$T_n = T_{n-1} + \omega^2(\Delta x_n/2)(I_{n-1}\theta_{n-1} + I_n\theta_n) \tag{29a}$$

For the bending calculations, one column is added in which the shear is obtained from the relation*

$$F_n = F_{n-1} + \omega^2(\Delta x_n/2)(\mu_{n-1}h_{n-1} + \mu_n h_n) \tag{29b}$$

In this way, any errors may be detected and corrected before proceeding further with the computation.

(IV) NUMERICAL EXAMPLES

(1) *Torsional Frequencies and Modes with Variable Tip Load*

The semiwing is divided into six sections of equal width, $\Delta x = 32$ in., the points of division being numbered from 0 to 6, with the point $x = 0$ at the wing tip

* If (Δx) is constant, this may be written in the form

$$F_n\left(\frac{\Delta x}{2}\right)^3 = F_{n-1}\left(\frac{\Delta x}{2}\right)^3 + \omega^2\left(\frac{\Delta x}{2}\right)^4(\mu_{n-1}h_{n-1} + \mu_n h_n)$$

TABLE 4

Sample Calculation for Torsional Modes with Variable Tip Inertia; $\omega^2(\Delta x/2)^2 = 10 \times 10^3$

$\theta_{n+1} =$ (4) × + (5) × (6) ÷ (7)

n	(4) θ_n	(5) $GJ_{n+1}/-\omega^2\left(\frac{\Delta x}{2}\right)^2 I_n$	(6) $\theta_n'\left(\frac{\Delta x}{2}\right)$	(7) $GJ_{n+1}+GJ_n$	(8) $GJ_{n+1}+\omega^2\left(\frac{\Delta x}{2}\right)^2 I_{n+1}$
0	$\frac{1.0000}{0}$	.40396	$\frac{0}{-.00270\,\bar{I}_t}$	.684	.40936
1	$\frac{.99681}{-.00451\,\bar{I}_t}$	.54164	$\frac{-.01319}{-.00181\,\bar{I}_t}$	.951	.54956
2	$\frac{.94376}{-.00758\,\bar{I}_t}$	.73144	$\frac{-.02386}{-.00126\,\bar{I}_t}$	1.281	.74356
3	$\frac{.83317}{-.00963\,\bar{I}_t}$	1.01844	$\frac{-.03273}{-.00079\,\bar{I}_t}$	1.762	1.03704
4	$\frac{.82154}{-.01080\,\bar{I}_t}$	1.46528	$\frac{-.03890}{-.00038\,\bar{I}_t}$	2.498	1.48280
5	$\frac{.74630}{-.01131\,\bar{I}_t}$	2.25720	$\frac{-.03934}{-.00013\,\bar{I}_t}$	3.740	2.28744
6	$\frac{.67702}{-.01137\,\bar{I}_t}$		$\frac{-.03294}{+.00007\,\bar{I}_t}$		

TABLE 5

Calculation of Tip Inertia Necessary to Satisfy Centerline Conditions for Various Frequencies; Antisymmetric and Symmetric Torsion

ω	$\omega^2\left(\frac{\Delta x}{2}\right)^2\times10^3$	$\omega^2\left(\frac{\Delta x}{2}\right)^2\Delta_n\times10^3$	θ_b	$\theta_b'\left(\frac{\Delta x}{2}\right)$	$\frac{[GJ_b(\frac{\Delta x}{2})^2\theta_b']}{-\omega^2(\frac{\Delta x}{2})^2 I_b}\times10^7$	$(I_t)_a$	$(I_t)_s$
37.5	2.5	1.05	$.90677 - .003328\,\bar{I}_t$	$-.00977 - .000055\,\bar{I}_t$	$-.98164 + .003328\,\bar{I}_t$	272.5	295.
53.	5.0	2.10	$.83400 - .00625\,\bar{I}_t$	$-.01752 - .00006\,\bar{I}_t$	$-1.80436 + .01294\,\bar{I}_t$	133.5	135.4
75.	10.0	4.20	$.67702 - .01137\,\bar{I}_t$	$-.03264 + .00007\,\bar{I}_t$	$-2.94306 + .04797\,\bar{I}_t$	59.6	61.4
106.	20.0	8.40	$.32323 - .01812\,\bar{I}_t$	$-.05335 + .00735\,\bar{I}_t$	$-2.87641 + .15444\,\bar{I}_t$	17.84	18.6
150.	40.0	16.80	$.02295 - .02145\,\bar{I}_t$	$-.06367 + .00295\,\bar{I}_t$	$-.57803 + .36928\,\bar{I}_t$	1.07	1.57
212.	80.0	33.60	$-.35972 - .00518\,\bar{I}_t$	$-.01992 + .00634\,\bar{I}_t$	$12.02631 + .13503\,\bar{I}_t$	-69.45	-61.66
225	90.0	37.80	$-.38550 + .00100\,\bar{I}_t$	$-.00518 + .00740\,\bar{I}_t$	$18.55624 - .01543\,\bar{I}_t$	385.5	943.4
237.2	100.0	42.00	$-.40471 + .00741\,\bar{I}_t$	$.01171 + .00757\,\bar{I}_t$	$17.03322 - .28833\,\bar{I}_t$	54.62	52.08
252.8	120.0	50.40	$-.40503 + .01934\,\bar{I}_t$	$.04465 + .00614\,\bar{I}_t$	$20.55151 - .95617\,\bar{I}_t$	20.95	21.49
335.4	200.0	84.00	$-.15632 + .05610\,\bar{I}_t$	$.12526 - .00436\,\bar{I}_t$	$13.50954 - 4.51558\,\bar{I}_t$	2.92	2.99
351.8	220.0	92.40	$-.07603 + .05610\,\bar{I}_t$	$.12869 - .00842\,\bar{I}_t$	$7.44820 - 5.20309\,\bar{I}_t$	1.36	1.42
362.4	240.0	100.80	$.00146 + .05646\,\bar{I}_t$	$.12584 - .01260\,\bar{I}_t$	$.23325 - 5.72926\,\bar{I}_t$	-.026	.041

The tabulated values of I and GJ, listed in Table 3, are taken from Fig. 1. Since I is discontinuous at station 4, $I_n(n = 4)$ is taken as 6.72, while $I_{n+1}(n = 3)$ must be taken as 11.04 in Eq. (4a). Column (7) of Table 3 may now be written down and columns (5) and (8) computed for an assumed value of $\omega = 75$ sec.$^{-1}$ or $\omega^2(\Delta x/2)^2 = 10^4$. The initial entry in column (4) is 1, and that in column (6) is found from the relation

$$(\theta_0')\left(\frac{\Delta x}{2}\right) = -\frac{\bar{I}_t\omega^2(\Delta x/2)^2}{GJ_0(\Delta x/2)} = -0.00270\bar{I}_t$$

resulting from the boundary condition at the tip. The complete table may now be constructed by filling in columns (4) and (6) with the aid of Eqs. (23) (cf. Table 4). The boundary conditions at the base may now be applied. For antisymmetric torsion, the condition

$$\theta_b = 0$$

gives

$$(I_t)_a = 59.62 \text{ lb. ft. sec.}^2$$

For symmetric torsion, the condition

$$GJ_b(\theta_b') = I_b\omega^2\theta_b$$

results in

$$(I_t)_s = 61.4 \text{ lb. ft. sec.}^2$$

By repeating the above process for other values of ω, Table 5 may be constructed.

Fig. 2 shows $(\bar{I}_t)_a$ plotted as a function of ω. The asymptote, corresponding to zero amplitude at the tip, may be located by interpolating for the point where the coefficient of $\bar{I}_t$ vanishes. This point also marks the transition from the first mode to the second. From Table 5, it can be seen that, except for large values, the difference between $(I_t)_a$ and $(I_t)_s$ is negligible.

The antisymmetric mode shapes corresponding to various values of $(I_t)_a$, obtained by resubstituting into the expressions for the deflections the appropriate values of this parameter, are shown in Fig. 3. To obtain the mode shape for the case when $\bar{I}_t \to \infty$, it must be recalled that the tip deflection, while taken as unity for convenience, is actually arbitrary. Thus, all subsequent deflections contain this arbitrary quantity θ_0 as a factor. By allowing $\bar{I}_t$ to become infinite and θ_0 to approach zero in such a way that the torque $\omega^2\bar{I}_t\theta_0$ remains finite, it is seen that only the coefficients of $\bar{I}_t$ remain. These coefficients give the required mode shape. The symmetric mode shapes differ only slightly from the antisymmetric and are therefore not shown.

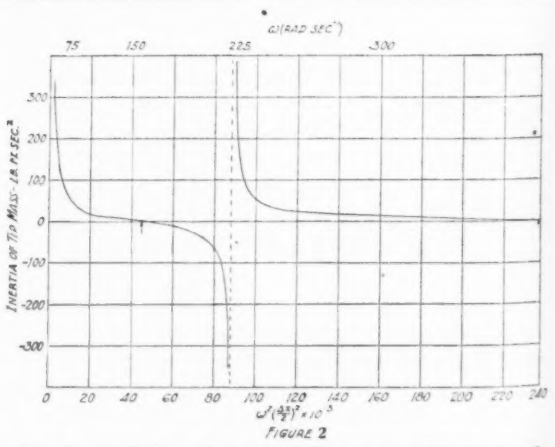

FIG. 2. Variation of torsional frequency with tip inertia. (Difference between symmetric and antisymmetric cases is negligible.)

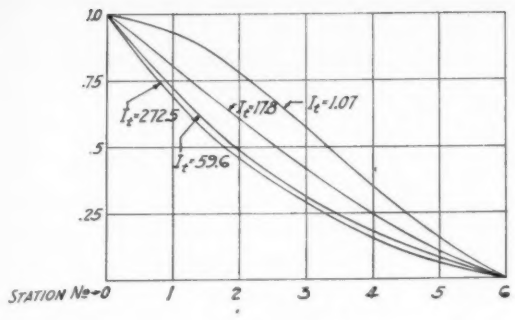

FIGURE 3a

FIG. 3a. Variation of the first antisymmetric torsional mode shape with tip inertia. (I_t is in lb. ft. sec.^{2}.)

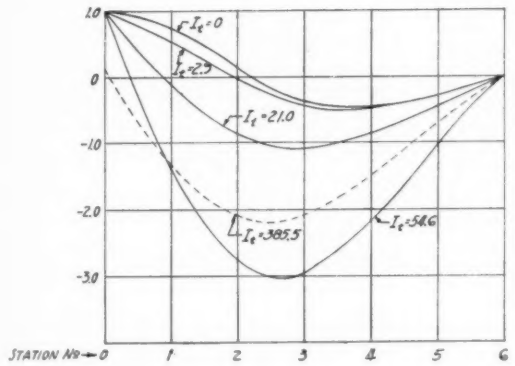

FIGURE 3b

FIG. 3b. Variation of the second antisymmetric torsional mode shape with tip inertia.

(2) *Bending Frequencies and Modes with Fixed Tip Load and Variable Load at the Center*

The mass and bending stiffness distribution for this example is shown in Fig. 4. Ten equal divisions of width $\Delta x = 1.9667$ ft. are used, the basic data being arranged in Table 6 in a manner similar to the data of the previous example.

Columns (7), (9), and (13) of Table 7 are independent of the value of the frequency and may, therefore, be filled in at once, while columns (5) and (12) may be filled in for an assumed value. In the example, the quantity $(\omega^2/g)(\Delta x/2)^4$ is used in place of the frequency itself, since Δx is constant and μ is given in weight rather than in mass units. Table 7 is constructed with $(\omega^2/g)(\Delta x/2)^4 = 0.3 \times 10^3$. The initial entry in column (4) is unity and that in column (6) is α, where $\alpha = p_0(\Delta x/2)$ and p_0 is the arbitrary slope at the tip. Rotary inertia of the tip mass is neglected, and so the initial entries in columns (8) and (15) are zero. The initial value in column (10) is obtained from Eq. (25b), which is rewritten as

$$F_0\left(\frac{\Delta x}{2}\right)^3 = \bar{m}_t\omega^2\left(\frac{\Delta x}{2}\right)^4\left(\frac{2}{\Delta x}\right)$$

whence,

$$F_0(\Delta x/2)^3 = 0.36183 \times 10^6$$

upon making use of the fact that $\omega^2/g\,(\Delta x/2)^4 = 0.3 \times 10^3$, $m_t g = 1.186 \times 10^3$ and $(\Delta x/2) = 0.98333$. The table is then completed, using Eqs. (26) to compute the successive values in columns (4), (6), (8), (10), and (15). Each entry in these columns consists of two parts: one depending on the initial tip amplitude and the other on the initial tip angle.

The values at the base in columns (4), (6), (10), and (15) are now used to determine the correctness of the assumed frequency. In the symmetric case, the condition that the slope at the center be zero gives

TABLE 6

Tabular Arrangement of Bending Stiffness and Weight Distribution

STA. Nº	(LB. FT.^{2})$\times 10^6$		(LB. FT.$^{-1}$)$\times 10^3$		FT.
n	EI_n	EI_{n+1}	$g(\mu_n)$	$g(\mu_{n+1})$	Δx_n
0	1.0	1.5	.010	.025	1.96667
1	1.5	2.0	.025	.050	↓
2	2.0	3.0	.050	.077	
3	3.0	5.0	.077	.105	
4	5.0	9.0	.105	.135	
5	9.0	17.0	.135	.165	
6	17.0	28.0	.165	.200	
7	28.0	40.0	.200	.240	
8	40.0	48.0	.240	.280	
9	48.0	52.0	.280	.340	
10	52.0	——	.340	——	↓
CONCENTRATED WEIGHT AT TIP:			1.186×10^{3}LB.		——

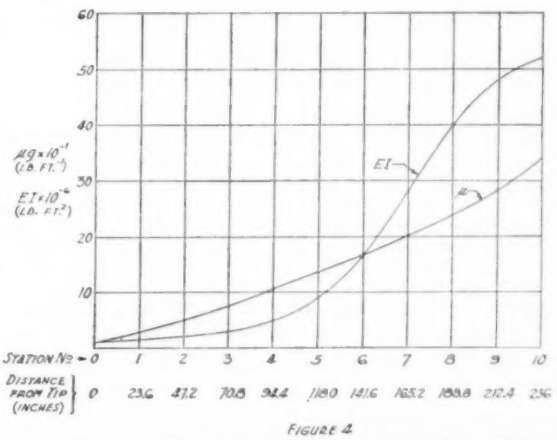

FIGURE 4

FIG. 4. Spanwise distribution of mass and bending stiffness.

TABLE 7

Sample Calculation for Bending Modes; $(\omega^2/g)(\Delta x/2)^4 = 0.3 \times 10^3$. (*Base Values Obtained by Including Rotary Inertia of Tip Weight.)

$h_{n+1} =$ (4) X (5) + (6) X (7) + (8) X (9) +2X (10) ÷ (12) (13) (15)

STA. №	DEFLECTION	×10⁻⁶	SLOPE	×10⁻⁶		×10⁻⁶	SHEAR ×10⁻⁶	×10⁻⁶	×10⁻⁶	MOMENT ×10⁻⁶	CHECK COLUMNS	
n	h_n	$EI_{n+1}+\omega^2(\frac{\Delta x}{2})^4\mu_n$	$P_n(\frac{\Delta x}{2})$	$2EI_{n+1}$	$\frac{M_n}{EI_n}(\frac{\Delta x}{2})^2$	$EI_{n+1}+EI_n$	$F_n(\frac{\Delta x}{2})^3$	$EI_{n+1}-\omega^2(\frac{\Delta x}{2})^4\mu_{n+1}$	EI_n	$M_n(\frac{\Delta x}{2})^2$	$\omega^2\mu_n(\frac{\Delta x}{2})^4$	$F_n(\frac{\Delta x}{2})^3$
0	1.00000 / 0	1.503	0 / α	3	0 / 0	2.5	.36183 / 0	1.4925	1	0 / 0	.003	.36183 / 0
1	1.49190 / 2.01005α	2.0075	.49190 / 1.01005α	4	.49190 / .01005α	3.5	.37602 / .01508	1.985	1.5	.73785 / .01508α	.0025	.37602 / .01508α
2	3.74624 / 4.10111α	3.015	1.76244 / 1.08101α	6	.77864 / .06091α	5	.44341 / .09166α	2.9769	2	1.55728 / .12182α	.015	.44340 / .09167α
3	8.95212 / 6.49628α	5.0231	3.44344 / 1.31410α	10	.90236 / .17224α	8	.70639 / .30324α	4.9685	3	2.70708 / .51672α	.0231	.70639 / .30325α
4	17.71832 / 9.61205α	9.0315	5.32276 / 1.80161α	18	.97696 / .31521α	14	1.47133 / .75609α	8.9595	5	4.88490 / 1.57605α	.0315	.47131 / .75609α
5	30.40937 / 13.97012α	17.0405	7.36829 / 2.55646α	34	1.06857 / .43964α	26	3.26100 / 1.62462α	16.9505	9	9.61713 / 3.95676α	.0405	3.26102 / 1.62466α
6	47.37427 / 20.03819α	28.0495	9.59661 / 3.51161α	56	1.15975 / .51551α	45	6.83762 / 3.18229α	27.94	17	19.71575 / 8.76367α	.0495	6.83762 / 3.18231α
7	69.15171 / 28.21310α	40.06	12.18083 / 4.66330α	80	1.42447 / .63618α	68	13.33179 / 5.86708α	39.928	28	39.88510 / 17.81304α	.060	13.33175 / 5.86700α
8	96.87967 / 39.02713α	48.072	15.54713 / 6.15073α	96	1.94183 / .85125α	88	24.45625 / 10.36988α	47.916	40	77.67320 / 34.05000α	.072	24.45619 / 10.36976α
9	132.93091 / 53.47341α	52.084	20.50441 / 8.29555α	104	3.01515 / 1.29357α	100	42.59775 / 17.67148α	51.898	48	144.72772 / 62.09136α	.084	42.59772 / 17.67148α
10	181.94750 / 73.46229α		28.51248 / 11.69333α		4.99322 / 2.10421α		72.32249 / 29.65608α		52	259.64744 / 109.41892α	.102	72.32257 / 29.65640α
10*	181.94750 / -31.70064α		28.51248 / -4.81087α		4.99322 / -.85945α		72.32249 / -12.73164α		52	259.64744 / -44.69158α	.102	72.32257 / -12.73182α

$$\alpha = -2.43835$$

The second condition at this point—namely,

$$F_b = -m_b\omega^2 h_b$$

gives

$$m_b g = -12.3 \text{ lbs.}$$

In the antisymmetric case, the value of α which gives zero displacement at the center is

$$\alpha = -2.47675$$

whence, from the second centerline condition,

$$M_b = \bar{I}_b\omega^2 p_b$$

it is found that

$$\bar{I}_b g = 80.17 \times 10^3 \text{ lb. ft.}^2$$

Repeating the process for other assumed frequencies, the variation of the symmetric frequency with mass at the base and of the antisymmetric frequency with the inertia at the base may be found. A convenient method of presenting these results graphically is as follows:

For each assumed value of the frequency, the quantity

$$F_b(\Delta x/2)^3/h_b$$

is evaluated for symmetric modes, and the quantity

$$M_b(\Delta x/2)^2/p_b(\Delta x/2)$$

for antisymmetric (Tables 8 and 9). These ratios are plotted as functions of $(\omega^2/g)(\Delta x/2)^4$ on an x-y coordinate system. In the symmetric case, the above graph is intersected by a family of lines through the origin whose equation is given by

$$y = [\bar{m}_b g/(\Delta x/2)]x$$

The points of intersection give the desired frequencies corresponding to varying values of $\bar{m}_b g$. Similarly, the antisymmetric curves are cut by a series of lines defined by the equation

$$y = [\bar{I}_b g/(\Delta x/2)^3]x$$

In Figs. 5 and 6, the lines corresponding to the values $\bar{m}_b g = 3 \times 10^3, 5 \times 10^3$ are shown. The radius of gyration of the fuselage is taken to be 1.5 ft. so that $\bar{I}_b = 2.25\,\bar{m}_b$.

TABLE 8

Calculations for Construction of Bending Frequency Diagram; Symmetric Modes

$\frac{\omega^2}{g}\left(\frac{\Delta x}{2}\right)^4 \times 10^{-3}$	ω	$B_1\left(\frac{\Delta x}{2}\right)^3$	α	h_b	$F_b\left(\frac{\Delta x}{2}\right)^3$	$-\frac{F_b}{h_b}\left(\frac{\Delta x}{2}\right)^3$
.005	13.1	.14673 +1.12415 α	-.13052	-.02673	.00658	.246
.006	14.4	.17748 +1.14233 α	-.15442	-.20142	.005296	.0263
.025	23.3	.82835 +1.63808 α	-.50546	-2.154	-.11570	-.0537
.050	41.5	1.89762 +2.31817 α	-.81858	-2.8241	-.36175	-.1281
.200	83.0	14.03571 +7.35249 α	-1.90897	.52247	-.78354	1.500
.220	87.0	16.48389 +8.15421 α	-2.02152	1.0343	-.68004	.6575
.250	92.8	20.56461 +9.41896 α	-2.18332	1.75622	-.46717	.266
.300	101.6	28.51240 +11.69333 α	-2.43835	2.82072	.01059	-.0038
.500	131.2	76.82828 +23.07201 α	-3.32992	5.44521	2.82281	-.518

TABLE 9

Calculations for Construction of Bending Frequency Diagram; Antisymmetric Modes

$\frac{\omega^2}{g}\left(\frac{\Delta x}{2}\right)^4 \times 10^{-3}$	ω	h_b	α	$B_b\left(\frac{\Delta x}{2}\right)$	$M_b\left(\frac{\Delta x}{2}\right)^2$	$\frac{M_b}{B_b}\left(\frac{\Delta x}{2}\right)$
.025	29.3	9.79591 +23.64166 α	-.41435	.14932	.25627	1.716
.040	37.1	15.56282 +25.97227 α	-.60106	.21323	.02232	.105
.050	41.5	19.62112 +27.41971 α	-.71558	.23809	-.25406	-1.067
.250	92.8	133.29355 +62.99458 α	-2.21120	-.26259	-9.63498	36.7
.300	101.6	181.9475 +73.4623 α	-2.47675	-.44898	-11.35587	25.3
.500	131.2	412.86302 +122.35063 α	-3.37442	-1.02658	-13.68043	13.33
.700	150	756.9292 +183.631 α	-4.12201	-1.28725	-10.04121	7.80
.900	176	1238.8053 +259.0228 α	-4.78261	-1.28458	-2.54831	1.984

From the figures and the data of Tables 8 and 9, it can be seen that, for $\bar{m}_b g = 5{,}000$ lbs., the first and second symmetric frequencies correspond to values of $(\omega^2/g)(\Delta x/2)^4 \times 10^{-3} = 0.006$ and 0.21, while the first two antisymmetric frequencies correspond to $(\omega^2/g)(\Delta x/2)^4 \times 10^{-3} = 0.037$ and 0.7. The symmetric frequencies and the first antisymmetric frequency are only slightly affected when $\bar{m}_b g$ is reduced to 3,000 lbs., while the value determining the second antisymmetric frequency is increased to 0.79. The actual frequencies are summarized as follows:

For $\bar{m}_b g = 5{,}000$ lbs.,

$$\omega_{s_1} = 14.2 \text{ sec.}^{-1}, \quad \omega_{s_2} = 84.9 \text{ sec.}^{-1}$$
$$\omega_{a_1} = 35.6 \text{ sec.}^{-1}, \quad \omega_{a_2} = 150 \text{ sec.}^{-1}$$

For $\bar{m}_b g = 3{,}000$ lbs.,

$$\omega_{s_1} = 14.9 \text{ sec.}^{-1}, \quad \omega_{s_2} = 87.3 \text{ sec.}^{-1}$$
$$\omega_{a_1} = 36.1 \text{ sec.}^{-1}, \quad \omega_{a_2} = 165 \text{ sec.}^{-1}$$

The above information may also be employed to show the effect of variable flexibility of the fuselage, such as would be encountered if the measured frequencies were obtained with the aircraft on partially inflated tires or air bags. Consider the symmetric case, and let ω_b be defined as the natural vertical frequency of the semifuselage itself on the flexible support. This quantity may be determined experimentally by measuring the frequency of the entire aircraft on the support, thus

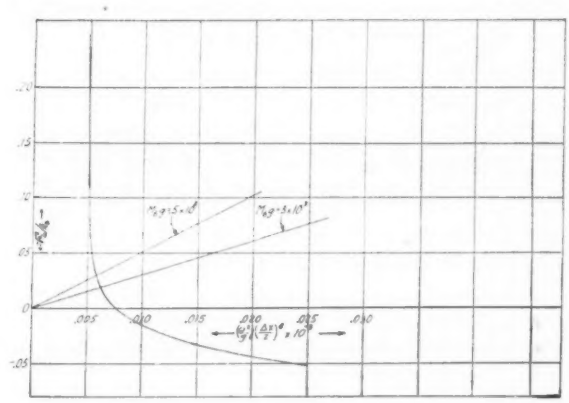

FIGURE 5a

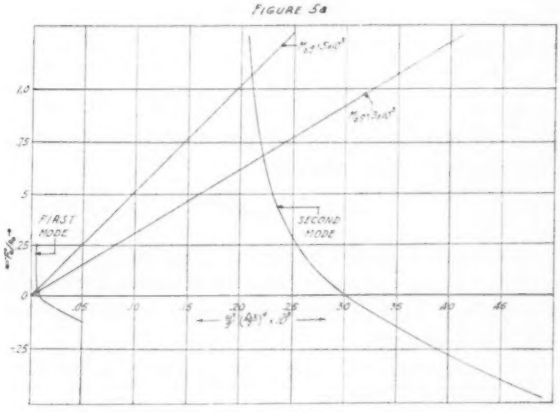

FIGURE 5b

FIG. 5. Location of the first and second symmetric bending frequencies for two values of $\bar{m}_b$. (5a) First mode. (5b) First and second modes.

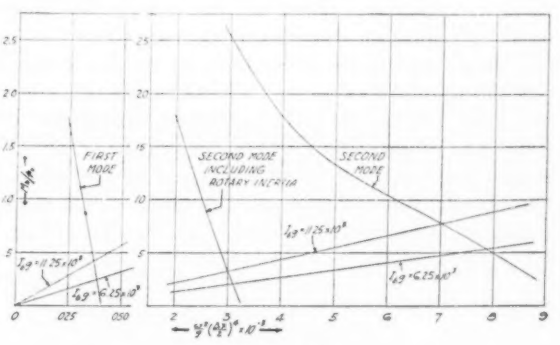

FIGURE 6

FIG. 6. Location of the first and second antisymmetric bending frequencies for two values of $\bar{I}_b$.

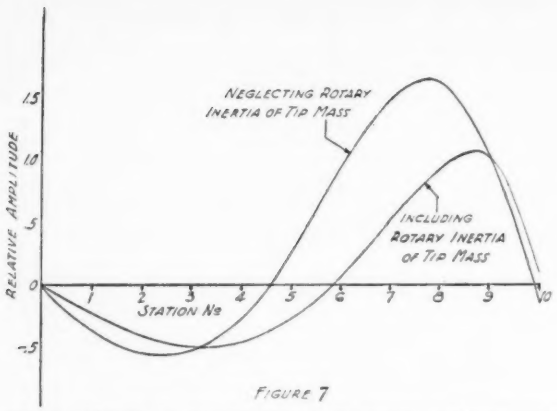

FIGURE 7

FIG. 7. Change in the shape of the second antisymmetric bending mode due to rotary inertia of the tip mass.

determining the stiffness K_b. The required frequency may then be found from the relation

$$\omega_b^2 = K_b/\bar{m}_b$$

The shear at the centerline must in this case be equal to the quantity

$$\bar{m}_b\ddot{h}_b + K_b h_b$$

or, making use of Eq. (29),

$$F_b = \omega^2 h_b \bar{m}_b[1 - (\omega_b/\omega)^2]$$

Thus, the actual mass at the base may be replaced by an "effective" mass equal to

$$\bar{m}_b[1 - (\omega_b/\omega)^2]$$

Since each assumed frequency ω for the system determines a corresponding value for the mass at the base the result is equivalent to a fixed mass at the base with variable flexibility.

The antisymmetric case may evidently be handled in an analogous manner.

(V) Rotary Inertia Effects

In general, the rotary inertia of elements of the wing itself is negligible. However particularly in higher modes of vibration, the inertia of concentrated items may have appreciable effect both on the mode shape and the resulting frequency. To illustrate this effect, the previous example was recomputed, taking into account the rotary inertia of the tip weight. Only the second entry in each space is affected by the change. The initial entry in column (15) (Table 7) is determined from the equation

$$M_t = -\bar{I}_t\omega^2 p_t$$

or,

$$M_t\left(\frac{\Delta x}{2}\right)^2 = I_t g\left[\frac{\omega^2}{g}\left(\frac{\Delta x}{2}\right)^4\right]\left[p_t\left(\frac{\Delta x}{2}\right)\right]\left(\frac{2}{\Delta x}\right)^3$$

The radius of gyration of the tip weight about the bending axis is 1.225 ft., whence,

$$M_t\left(\frac{\Delta x}{2}\right)^2 = -1.779\left[\frac{\omega^2}{g}\left(\frac{\Delta x}{2}\right)^4\right]\alpha \times 10^3$$

The final values are shown in the last line of Table 7.

Carrying out the correction for a second frequency corresponding to

$$(\omega^2/g)(\Delta x/2)^4 = 0.2 \times 10^3$$

determines the second curve indicated in Fig. 6. It can be seen that, for $\bar{I}_b g = 11.25$, the corresponding value of

$$[(\omega^2/g)(\Delta x/2)^4] \times 10^{-3}$$

is decreased from 0.7 to 0.3, a reduction of 35 per cent in the frequency itself. It may also be noted that the inertia of the fuselage is less effective when the inertia of the tip mass is considered. In the symmetric case, there is also considerable reduction in the frequency of the second mode, although it is not so great as in the antisymmetric.

The change in the shape of the second antisymmetric mode is shown in Fig. 7. Unlike the case when the rotary inertia was neglected, it is possible to obtain a mode shape with zero amplitude at the tip without an infinitely large tip mass. For this reason the deflections were "normalized" to unity at the second inboard station rather than at the tip station.

References

[1] Den Hartog, J. P., *Mechanical Vibrations*, 2nd Ed., Art 41; McGraw-Hill Book Company, Inc., New York, 1946.

[2] Timoshenko, S., *Vibration Problems in Engineering*, 2nd Ed., Art. 43; D. VanNostrand & Company, New York, 1937.

[3] Myklestad, N. O., *Vibration Analysis*, McGraw-Hill Book Company, Inc., New York, 1944.

[4] Targoff, W. P., *The Associated Matrices of Bending and Coupled Bending-Torsion Vibrations*, Journal of the Aeronautical Sciences, Vol. 14, No. 10, p. 579, October, 1947.

[5] Myklestad, N. O., *A New Method of Calculating Natural Modes of Uncoupled Bending Vibration of Airplane Wings and Other Types of Beams*, Journal of the Aeronautical Sciences, Vol. 11, pp. 153–162, April, 1944.

[6] Bellin, A. I., *Determination of the Natural Frequencies of the Bending Vibrations of Beams*, Journal of Applied Mechanics, Vol. 14, No. 1, pp. A-1–A-6, March, 1947.

[7] Hussmann, A. W., *Calculation of Torsional Vibrations in Engines*, Lecture presented at the 20th National Conference, A.S.M.E., Oil and Gas Division, St. Louis, May, 1948.

Readers' Forum

BRIEF REPORTS of investigations in the aeronautical sciences and discussions of papers published in the JOURNAL *will be presented in this special department. The publication will be completed 6 to 8 weeks after receipt of the material. No proof will be sent to the authors. The Editorial Committee does not hold itself responsible for the opinions expressed by the correspondents. Contributions should not exceed 800 words in length.*

A Note on the Velocity of Sound

Morris Morduchow
Polytechnic Institute of Brooklyn, Brooklyn, N.Y.
June 25, 1949

THE PURPOSE of this note is to show that the well-known differential expression $a^2 = dp/d\rho$ for the velocity of sound cannot, as is sometimes attempted, be rigorously derived from the steady one-dimensional differential equations of nonviscous flow. It is also the purpose to show that these equations can, nevertheless, be used to derive the expression $a^2 = \gamma p/\rho$ without the rejection of any small-order terms.

The basic differential equations for one-dimensional flow referred to above and representing, respectively, conservation of mass, momentum, and energy are:

$$\rho\, du + u\, d\rho = 0 \tag{1}$$

$$\rho u\, du + dp = 0 \tag{2}$$

$$u\, du + c_p\, dT = 0 \tag{3}$$

where u, p, ρ, and T denote velocity, pressure, density, and temperature, while c_p is the specific heat at constant pressure. The general solution of Eqs. (1), (2), and (3) and the ideal gas law $p = \rho RT$ is the "trivial" solution u = constant, p = constant, ρ = constant, T = constant. One may, however, assume a discontinuity present, separating two regions in each of which u, p, ρ, and T are constant, but with different values for the two regions. The derivative $dp/d\rho$ is then zero everywhere except at the discontinuity where its value is indeterminate.

If the increments in u, p, and ρ are considered as finite though small but not as differentials, Eqs. (1), (2), and (3) are still valid, and it is possible by the above means to arrive at the result $u^2 = \Delta p/\Delta\rho$. It would, however, be incorrect now to let $\Delta p \to 0$, to write $a^2 = \lim\ (\Delta p/\Delta\rho) = dp/d\rho$, and to interpret $dp/d\rho$ as a derivative, since in the limit of the equations of motion reduce to the differential forms (1), (2), and (3), and the false implication would have been made that the derivative $dp/d\rho$ is determinate at the discontinuity.

It may be interesting to observe that attempts to derive formulas by ignoring the indeterminateness of the derivative at the discontinuity will lead automatically to mathematical inconsistencies. For example, suppose that from Eqs. (1) and (2), one writes

$$u^2 = dp/d\rho \tag{4}$$

while from Eqs. (2) and (3) and the gas law one obtains

$$p = k\rho^\gamma \tag{5}$$

where k is an arbitrary constant and γ is the ratio c_p/c_v of specific heats. Then considering (incorrectly) Eq. (4) as a derivative, it would follow from Eqs. (4) and (5) that

$$u^2 = \gamma p/\rho \tag{6}$$

If, however, to be consistent, expression (6) is now considered as differentiable for substitution into Eq. (4), giving

$$u\, du = (1/2)\gamma d(k/\rho)$$

substitution into Eq. (2) would lead to

$$p = c\rho^{\gamma/(\gamma+2)} \tag{7}$$

where c is an arbitrary constant. The change of state [Eq. (7)] evidently contradicts Eq. (5).

In spite of such inherent inconsistencies contained in treating Eqs. (1), (2), and (3) as if derivatives such as $dp/d\rho$ existed, the above type of derivation of expressions (4)–(6) is sometimes seen in the literature. An elegant way of rigorously deriving Eq. (6) from the (physically correct) differential equations [Eqs. (1), (2), and (3)] is to integrate these equations. Thus, these equations become:

$$\rho_1 u_1 = \rho_2 u_2 \tag{1a}$$

$$\rho_1 u_1^2 + p_1 = \rho_2 u_2^2 + p_2 \tag{2a}$$

$$(u_1^2/2) + c_p T = (u_2^2/2) + c_p T_2 \tag{3a}$$

where the subscripts 1 and 2 refer to values at two different points in the field. From Eq. (1a), (2a), and (3a) and the gas law, it is found that the pressure ratio p_2/p_1 must have either a value of identically unity ("trivial" solution) or a value (Rankine-Hugoniot) of

$$\frac{p_2}{p_1} = \frac{2}{\gamma+1}\left(\frac{\rho_1 u_1^2}{p_1}\right) - \frac{\gamma-1}{\gamma+1} \tag{8}$$

Eq. (8) represents a wave of finite discontinuity ("shock wave"). Defining a sound wave now as an infinitesimally weak shock wave—i.e., as one for which $p_2/p_1 \to 1$—it follows from Eq. (8) that for a sound wave

$$\rho_1 u_1^2/p_1 \to \gamma \quad \text{or} \quad u_1^2 \to \gamma p_1/\rho_1$$

Thus expression (6) for the velocity of sound is derived in a neat rigorous manner from the straightforward differential equations of motion, without the rejection of any terms in these equations. The differential expression (4), however, cannot be so derived. A proper derivation of Eq. (4), based on the equations of *unsteady* flow, is given, for example, in reference 1.

REFERENCE

[1] Lamb, H., *Hydrodynamics*, 6th Rev. Ed., pp. 476–477, London, 1932; reprinted by Dover Publications, New York, N.Y., 1945.

Lift and Drag of Rectangular Wings of Finite Aspect Ratio in Accelerated, Transonic Flight

C. S. Gardner and H. F. Ludloff
New York University, University Heights, New York, N.Y.
July 8, 1949

IN A PAPER PRESENTED at the I.A.S. Seventeenth Annual Meeting in January, 1949 (Preprint No. 186), the authors investigated the influence of acceleration on lift and drag of a two-dimensional airfoil moving at supersonic or transonic speed. In particular, it was shown how the aerodynamic characteristics remain finite and vary continuously when the flight speed $U + bt$ passes through the sound speed a. The purpose of the present note is to indicate how the method and results can be extended to wings of finite aspect ratio. In the latter case, the applicability of the linearized theory in the transonic range is more legitimate than in the case of infinite aspect ratios.

The drag can be derived by use of retarded potentials, which can be brought into the form of Possio solutions:

$$\varphi = \int_R \int \frac{\sigma(\xi, \tau)}{\sqrt{(t-\tau)^2 - (1/a^2)(x-\xi)^2}}\, d\xi d\tau$$

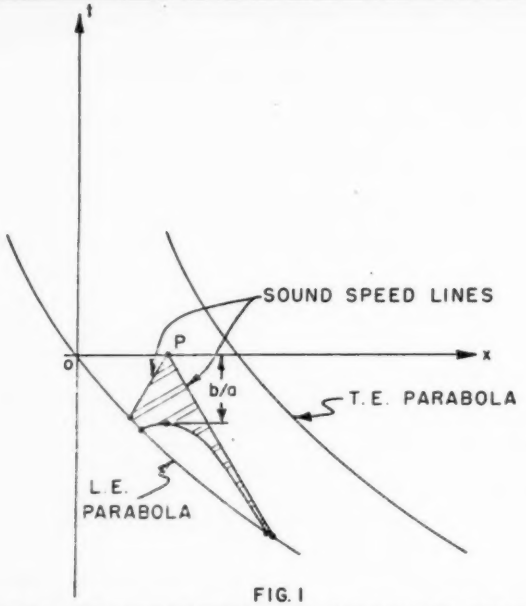

FIG. 1
AREA OF INTEGRATION FOR AIRFOIL OF SPAN b

where σ is given by

$$\sigma(\xi, \tau) = -(1/\pi)\varphi_y = -(1/\pi)f'[\xi + U\tau + (1/2)b\tau^2]$$

$f(x)$ being the airfoil profile form.

One can show that, for rectangular wings of finite aspect ratio, the domain of integration in the $x - t$-plane, R, is given by the shaded area in Fig. 1, which is bounded by the two sound speed lines, passing through any point P on the airfoil surface, by the parabolic path of the leading edge and by a hyperbola whose vertex is at a distance b/a (b = span length of wing) from P. (See Fig. 1.)

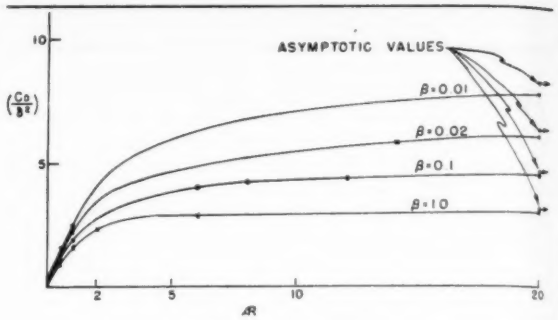

FIG. 3
C_D vs AR—WEDGE AT M=1

In Fig. 2, the analytical results have been plotted in a graph representing C_D vs. M for different A.R.'s, at an acceleration parameter $\beta = -(2bl)/a^2 = 0.02$ (1 chord length), which is representative of accelerations occurring in rocket motion.

The maximum of C_D (and C_L), at $M = 1$, becomes less and less pronounced, as the aspect ratio decreases. (See Fig. 2.) This is further elucidated by Fig. 3, representing C_D vs. A.R. at $M = 1$, for different β-values; it is seen that $C_D \to 0$ for A.R. $\to 0$, so long as $\beta \neq 0$. For $\beta = 0$, C_D becomes logarithmically infinite for all finite A.R. $\neq 0$.

As these results are obtained by a linearized approximation, they may be considered valid as long as the pressure disturbance produced by the airfoil is small compared to the dynamic pressure at the leading edge—in other words, as long as $C_p \ll 1$ or, if we average the pressure distribution over the chord length, $\bar{C}_p \ll 1$. Taking a thin supersonic airfoil of 5 per cent thickness ratio, we have, at $M = 1$, for $\beta = 0.02$

$\bar{C}_p \sim 0.25$ for A.R. ∞
0.2 for A.R. 7
0.14 for A.R. 2

Therefore, the above results might be considered as reasonably valid, even at $M = 1$; the smaller the A.R. is, the better becomes the approximation.

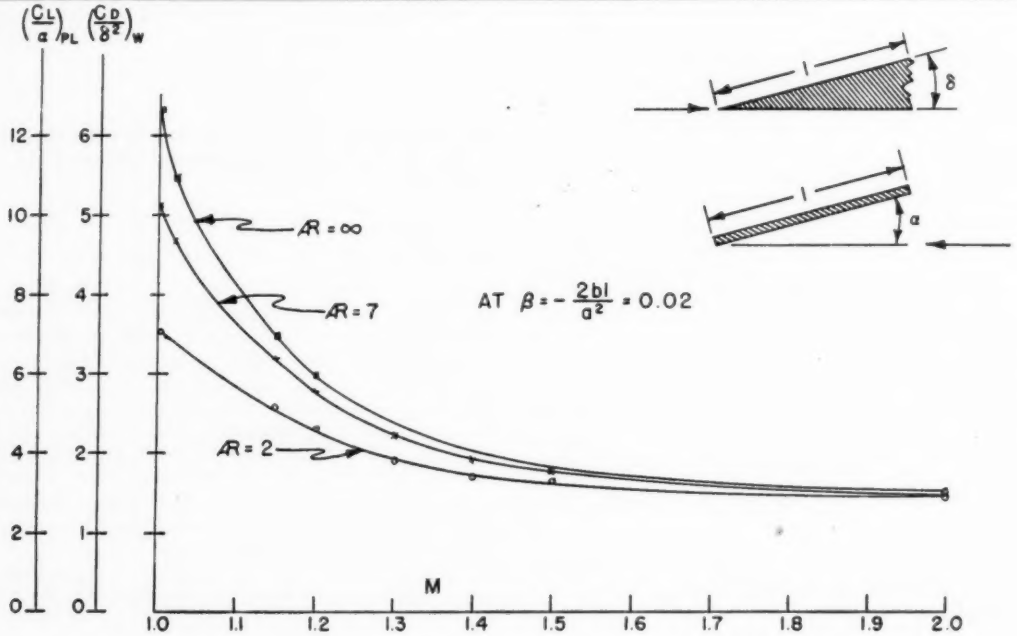

FIG. 2
C_D vs M—WEDGE C_L vs M—FLAT PLATE

Effect of Disposable Load on Range of Turbojet Airplanes

W. F. Savage
Assistant Professor, Department of Mechanical Engineering, University of Kentucky, Lexington, Ky.
August 1, 1949

IN CONSTANT ALTITUDE CRUISING FLIGHT of turbojet-propelled military aircraft, analytical equations can be derived for the range and average operating speed when a bomb or cargo load is dropped at the midpoint of the flight.

As outlined by Ashkenas,[1] a formula can be derived for the maximum range of turbojet aircraft. By considering flight at constant $C_L^{1/2}/C_D$, which would be possible for most aircraft at altitudes equal to, and below, combat ceiling, the formula for the maximum range of an airplane for a ferry mission would be:

$$R(\text{miles}) = 39.6\,\frac{C_L^{1/2}}{C_D}\,\frac{1}{(\sigma S)^{1/2}}\,\frac{1}{c}\,(W_i^{1/2} - W_f^{1/2})$$

where S is the wing area, σ is the altitude density ratio, c is the thrust specific fuel consumption, W_i is the take-off gross weight, and W_f is the landing gross weight. The thrust specific fuel consumption is assumed essentially constant, and the entire weight difference between the take-off and landing gross weights is considered due to fuel only.

The above equation is used to develop the range expression for the condition where a bomb or cargo load is dropped at the range midpoint. If W_x is the gross weight of the airplane before dropping bombs or cargo and if W_y is the gross weight of the airplane after the drop, the maximum range equation can be written as:

$$R(\text{miles}) = 2(39.6)\,\frac{C_L^{1/2}}{C_D}\,\frac{1}{(\sigma S)^{1/2}}\,\frac{1}{c}\,(W_i^{1/2} - W_x^{1/2})$$

or

$$R(\text{miles}) = 2(39.6)\,\frac{C_L^{1/2}}{C_D}\,\frac{1}{(\sigma S)^{1/2}}\,\frac{1}{c}\,(W_y^{1/2} - W_f^{1/2})$$

since the outgoing range leg is equal to the return range leg. The substitution that $W_x = W_y + W_D$ can also be made, where W_D is the cargo or bomb weight and expressions for W_x and W_y can be written in terms of W_i, W_f, and W_D.

$$W_x = [(N^2 + W_D)/2N]^2, \quad W_y = [(N^2 - W_D)/2N]^2$$

where $N = W_i^{1/2} + W_f^{1/2}$.

Since the take-off gross weight is the sum of the disposable weight, the landing weight and the fuel weight, or $(W_i = W_D + W_f + W_F)$, the disposable weight can be eliminated from the range equation by inclusion of the fuel weight, W_F. Thus,

$$W_x = \left[\frac{N^2 + (W_i - W_f - W_F)}{2N}\right]^2,$$

$$W_y = \left[\frac{N^2 - (W_i - W_f - W_F)}{2N}\right]^2$$

If the equation for either W_x or W_y is substituted in the range equation with bombs or cargo dropped, the resulting equation can be simplified by introducing the fuel weight-take-off weight ratio, K_F; the landing weight-take-off weight ratio, K; and the take-off wing loading, m. The final range equation for the condition where bombs or cargo are dropped at the range midpoint will be obtained.

$$R(\text{miles}) = 39.6\,\frac{C_L^{1/2}}{C_D}\left(\frac{m}{\sigma}\right)^{1/2}\frac{1}{c}\left(\frac{K_F}{1 + K^{1/2}}\right)$$

This equation does not consider any expenditure of fuel for warm-up, take-off, or climb, but this can be easily allowed for by considering W_i as the gross weight when cruise begins at altitude. It will be noted in the above equation that the disposable load does not appear, but the equation is only applicable to the condition where the disposable load is dropped at the range midpoint and the fuel load is based on such an operation.

The average operating speed for the condition where a disposable load is dropped at the range midpoint can be written as:

$$V_{\text{avg.}} = 4V_i\,\frac{[K_F/(1 + K^{1/2})]}{\ln\left[\frac{1}{K}\left(\frac{2K^{1/2} + K + K_F}{2K^{1/2} + 2 - K_F}\right)^2\right]}$$

where V_i is the initial cruising speed at take-off gross weight.

For the case of constant speed cruising flight, the range formula for the condition where a disposable load is dropped at the range midpoint can be derived.

$$R(\text{miles}) = 2\,\frac{V}{c}\,\frac{C_L}{C_D}\ln\frac{W_i}{W_x}$$

or

$$R(\text{miles}) = 2\,\frac{V}{c}\,\frac{C_L}{C_D}\ln\frac{W_y}{W_f}$$

Since $W_y = W_x - W_D$, it is possible to solve for W_x in terms of W_i, W_f, and W_D. Thus,

$$W_x = (W_D + \sqrt{W_D^2 + 4W_fW_i})/2$$

and

$$R(\text{miles}) = 2\,\frac{V}{c}\,\frac{C_L}{C_D}\ln\frac{2W_i}{W_D + \sqrt{W_D^2 + 4W_fW_i}}$$

In the constant speed condition, the lift and drag coefficients will vary as the gross weight changes but it has been found by the author that the use of an average value of these coefficients based on landing and take-off gross weights is sufficiently accurate for most range calculations for constant speed cruise.

REFERENCE

[1] Ashkenas, I., *Range Performance of Turbojet Airplanes*, Journal of the Aeronautical Sciences, Vol. 15, No. 2, pp. 97–101, February, 1948.

An Empirical Study of Low Aspect Ratio Lifting Surface with Particular Regard to Planing Craft

N. Scholz
Dr.-Ing., Institute of Fluid Mechanics, Technical University, Braunschweig, Germany
August 1, 1949

IN AN ARTICLE by F. W. S. Locke, Jr. (Journal of the Aeronautical Sciences, Vol. 16, No. 3, p. 184, March, 1949), the author attempts to solve the problem of the lifting surface of small aspect ratio purely empirically, using given measurements. But when giving empirical formulas, one should not overlook the theoretical results obtained with great difficulty. One should respect them in the structure of the empirical equations.

The theory of the lifting surface has been developed as a linear theory, and, within the scope of its validity, it agrees well with experimental results. Compared with a theory of higher order, it gives at least the lift and pitching moment slope for zero incidence. It does not contain the influence of the finite wing thickness on the total lift. In setting up an empirical equation for the lift slope the following points should, therefore, be taken into consideration:

(1) For $\alpha \to 0$, the formula should reduce to the linear lifting surface theory.

(2) It should be set up for the flat plate (infinitely thin). The finite thickness and the shape of the profile should then be accounted for by means of an additional factor.

The lift coefficient should therefore be developed in powers of $\sin\alpha$, but one needs only consider the first two terms. For an extremely thin flat plate, one obtains, then:

$$C_L = K_1 \sin \alpha + K_2 \sin^2 \alpha \qquad (1)$$

K_1 and K_2 are dependent on the aspect ratio, as well as on the plan form of the lifting surface. Their limiting values are:

$$\Lambda \to 0: \quad K_1 = 0; \quad K_2 = 2$$
$$\Lambda \to \infty: \quad K_1 = 2\pi; \quad K_2 = 0$$

K_1 can be obtained from the linear theory of the lifting surface for every aspect ratio and plan form. For an elliptical plan form, the following formula can be given as I have shown in a recent paper:[1]

$$K_1 = 2\pi\Lambda/(2 + \sqrt{\Lambda^2 + 4}) \qquad (2)$$

For $\Lambda \to 0$, there is:

$$K_1 = (\pi/2)\Lambda \qquad (3)$$

Eq. (3) is valid for all plan forms, as has also been given by Jones.[2] With good approximation it can be used for aspect ratios $\Lambda \leq 1$. Bollay[3] calculated the value of $K_2 = 2$ for $\Lambda \to 0$. This result is in good agreement with measurements. For aspect ratios $\Lambda > 3$, the curves $C_L(\alpha)$ are always linear, and therefore $K_2 = 0$ for $\Lambda > 3$.

It is well known from measurements at large aspect ratios that the influence of the finite thickness of the wing and the profile shape on the lift is extremely small as long as the thickness ratio remains within normal limits. For aspect ratios $\Lambda < 3$, such an influence is, however, present, as has been shown by different measurements. Compared with flat plates, the lift slope of airfoils for $\alpha = 0$ is smaller. The influence of the finite thickness would have to be accounted for by means of a correction factor for the constants K_1 and K_2.

However, there are still other influences on the lift. The flow around the wing tips is of great importance. This flow, on the other hand, is mainly dependent on the shape of the side edges and on the wing plan form and profile. As the situation is not at all clear, only extensive systematic pressure distribution measurements may solve this problem. That there is such an influence is, however, clearly shown by the measurements published by Winter[4] and Zimmermann.[5] However, not enough reliable measurements have been made to consider these effects in our lift formula.

REFERENCES

[1] Scholz, N., *Beiträge zur Theorie der tragenden Fläche*, Doctor-thesis of the Techn. University of Braunschweig, 1949. (Shortly to be published in the Ingenieur-Archiv.)

[2] Jones, R. T., *Properties of Low Aspect Ratio Pointed Wings at the Speed and Above the Speed of Sound*, N.A.C.A. T.M. No. 1032, 1946.

[3] Bollay, W., *A Non Linear Wing Theory and Its Application to Rectangular Wings of Small Aspect Ratio*, Zeitschr. f. angew. Math. u. Mech., Bd. 19, 1940, S.21.

[4] Winter, H., *Flow Phenomena on Airfoils and Plates of Short Span*, N.A.C.A. T.M. No. 798, 1936.

[5] Zimmermann, H., *Characteristics of Clark Y Airfoils of Small Aspect Ratio*, N.A.C.A. Report No. 431, 1932.

Base Pressures at Supersonic Velocities

Ingénieur Général Gabeaud
Centre d'Essais de Mécanique des Fluides, Paris, France

July 9, 1949

IN THE MARCH, 1949, ISSUE, the JOURNAL OF THE AERONAUTICAL SCIENCES published, under the title "Base Pressures at Supersonic Velocities," a well-documented paper of Freeman K. Hill and Ralph A. Alpher. I read on page 159, that "there has not been published any satisfactory theory to predict the values of the base pressure. However, in 1932, von Kármán and Moore developed a semiempirical formula that gave the base pressure coefficients as

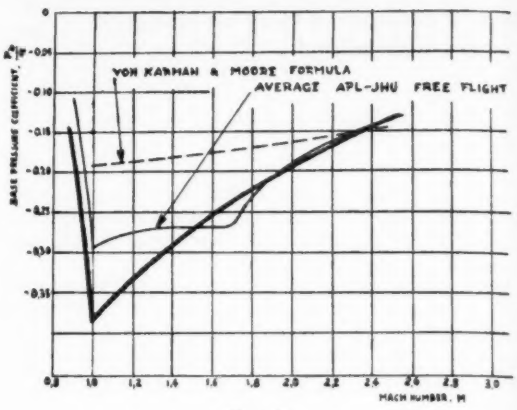

FIG. 1.

$$p/p_0 = \{1 - [(\gamma - 1)/2]\lambda M^2\}^{\gamma/(\gamma-1)}$$

where p is the absolute value of the pressure at the base, p_0 is free stream static pressure, γ is the ratio of specific heats, and λ is an arbitrary constant to which on the basis of low subsonic measurements von Kármán and Moore assigned the value 0.2."

I wish to point out, for what use it may have, that I published in 1931 a turbulence theory of residual resistance.[1] This theory is, moreover, known to Dr. von Kármán, who referred to it in the paper he presented October 2, 1935, at the Volta Congress;[2] at the same conference (p. 281) Margoulis pointed out that I had subsequently made an "improvement" in my theory. Returning to this subject, in 1936[3] I gave new developments and presented a curve giving unit base pressure as a function of speed. If the law of variation of pressure coefficient as a function of Mach Number is inferred from it, there is obtained the curve represented by a heavy line on Fig. 1, where I have reproduced the two curves (free flight and von Kármán and Moore formula) taken from Fig. 10 of Hill and Alpher's paper. It may be maintained that my theoretical curve of 1936, when superimposed on the average experimental curve of free flight, presents a significant correlation, notably in the region $(0.9 < M < 1.7)$ where disagreement is particularly obvious between the free-flight results and those of the semiempirical formula of von Kármán and Moore.

I wish to add that, since 1936, I have again added refinements to my theoretical outline; the results, not published, coincide still further with those of free flight.

REFERENCES

[1] *Comptes-rendus de l'Academic des Sciences*, Vol. 192, p. 1630, 1931.

[2] Reale Accademia d'Italia, Fondazione Alessandro Volta, *Convegno di Scienze Fisiche, Matematiche e Naturali, 1935. Le Alte Velocita in Aviazione*, pp. 270, 271, 281; Rome, 1936.

[3] "Recherches sur la résistance de l'Air," (*Memorial de l'Artillerie Française*, Tome XV, 4ème fascicule de 1936, pp. 1290–1300).

Propeller Flutter

M. J. Turner* and James B. Duke
Supervisor of Dynamic Analysis, Chance Vought Aircraft Division, United Aircraft Corporation; and Analytical Engineer, Vibration Group, Hamilton Standard Propellers Division, United Aircraft Corporation, respectively.

July 21, 1949

THE AUTHORS would like to clarify the simplifications made in the body of their paper[1] regarding the mode shapes to be employed in a propeller flutter analysis. It is to be recalled that

* Presently employed as Vibration Engineer at the Boeing Airplane Company.

the normal modes there derived were based on a clamped root section in the hub. The emphasis to be placed on appropriate displacement forms in a propeller flutter study stems from a wide background of experience in attempting to represent the vibratory characteristics of a complex beam by as few normal modes as possible. Small errors in this representation have large effects on the important energy forms and often produce results that are subject to question.

In generalizing the analysis presented in the paper, it is desirable to consider the entire vibrating system of the propeller and its power plant. Because the blade is twisted, the normally uncoupled axial and torsional motions of the propeller shaft result in coupled modes in the blade itself. The resulting "system modes" can be classified in the following manner.

Class I—Torquewise angular displacements of the propeller hub are accompanied by linear axial motions due to blade twist. A simplification of this class forms the basis on which the original derivations were made.

Class II—Whirling modes that result when work is done on the propeller by the rotating forces within the engine. Because of blade twist, angular motions of the shaft axis are coupled with lateral motions of this axis so that the centerline describes a hyperboloid of revolution.

Class III—Reactionless modes that result from certain phase relations between blades at multiples of propeller rotational speeds. At the center of rotation these result in complete cancellation of vibratory reactions.

Extensive subdivision can be made in each of these classes for particular conditions. An exact treatment of any type of system modes would be accomplished by combining the engine and propeller components of the system through an impedance concept in order to make engine and propeller motions and reactions conformable at the blade root. Since this treatment would require the consideration of mathematical complexities not directly associated with the essential features of propeller flutter, it was not included in the paper.

Reference

[1] Turner, M. J., and Duke, James B., *Propeller Flutter*, Journal of the Aeronautical Sciences, Vol. 16, No. 6, pp. 323–336, June, 1949.

Compressibility Correction for Axially Symmetric Bodies

E. V. Laitone
Associate Professor, University of California, Berkeley, Calif. Also Consulting Aerodynamics Engineer, Hughes Aircraft Company
July 18, 1949

EQ. (14) OF REFERENCE 1 presents an integral that is nonexistent and therefore cannot be considered proof that there is no compressibility correction on an axially symmetric body.

The correct expression for the surface pressure coefficient on a symmetrical body of revolution with a local cross-sectional area of $S(x)$ and a total length L is given in reference 2 for linearized subsonic flow as

$$C_p = \frac{1}{2\pi}\int_0^L \frac{S^{(1)}(\xi)(\xi - x)\,d\xi}{[(\xi - x)^2 + \beta^2 r^2]^{3/2}} - [r^{(1)}]^2 \qquad (1)$$

or

$$C_p = 1 - \frac{1}{\pi}\left\{\left[\frac{1 - \frac{2x}{L}}{1 - \frac{x}{L}}\right]\frac{S^{(1)}}{2x} - \left[1 + \log\frac{\frac{r}{L}}{2\sqrt{\frac{x}{L}\left(1 - \frac{x}{L}\right)}} + \log\beta\right]S^{(2)} + \frac{L}{4}\left[1 - \frac{2x}{L}\right]S^{(3)} + \frac{L^2}{24}\left[1 - \frac{2x}{L} + \frac{2x^2}{L^2}\right]S^{(4)} + \ldots\right\} - [r^{(1)}]^2 + O(r^3) \qquad (2)$$

where $\beta = \sqrt{1 - M^2}$ and $r^{(1)} = dr/dx$.

This shows that the compressibility effects depend on the actual location on a given body, as well as the shape of the body as defined by the second derivative of the cross-sectional area. For example, at the midpoint of *any* symmetrical body of revolution

$$\left(\frac{C_p}{C_{p_{M=0}}}\right)_{x = L/2} = 1 + \left(\log\beta \Big/ \left\{1 + \log\frac{r}{L} - \left[\frac{L^2}{48}\frac{S^{(4)}}{S^{(2)}} + \ldots.\right]\right\}\right) \qquad (3)$$

As seen in Fig. 2 of reference 2, the compressibility effects are negligible for a prolate spheroid less than 5 per cent thick provided the Mach Number remains less than 0.8.

References

[1] Dorrance, W. H., *On the Compressibility Correction Factor for Axially Symmetric Bodies*, Readers' Forum, Journal of the Aeronautical Sciences, Vol. 16, No. 7, pp. 443–444, July, 1949.

[2] Laitone, E. V., *The Subsonic Axial Flow About a Body of Revolution*, Quarterly of Applied Mathematics, Vol. 5, No. 2, pp. 227–231, July, 1947.

Erratum

W. E. Strohmeyer and D. R. Gero
North American Aviation, Inc., Los Angeles, Calif., and Goodyear Aircraft Corporation, Akron, Ohio, respectively
September 13, 1949

THE FOLLOWING ERROR appeared in our Readers' Forum item "An Approach to Supersonic Airfoil Theory" (JOURNAL OF THE AERONAUTICAL SCIENCES, Vol. 16, No. 8, pp. 506–507, August, 1949).

The first equation in the right-hand column at the top of page 507 should read:

$$\Delta \text{ P.E.} = \left(P_0 + \frac{\Delta P}{2}\right)\Delta v; \quad \Delta v = U\,dt$$

Services of the Libraries of the Institute of the Aeronautical Sciences

The services of the Libraries are available to all members of the Institute, to Corporate Members, to advertisers in the AERONAUTICAL ENGINEERING REVIEW and AERONAUTICAL ENGINEERING CATALOG, and, under usual library limitations, to the public. Four specialized services are available.

The Paul Kollsman Lending Library

This lending library service makes available, *without charge*, the latest and more important aeronautical books.

Members may request the loan of any aeronautical or technical book they wish to borrow. Through an exchange agreement with the Engineering Societies Library, any book on general engineering may be borrowed from its great collection of over 160,000 volumes.

A photostating service is available at usual library rates.

Applications for membership in the library and further information will be sent on request.

The W. A. M. Burden Reference Library

This reference library contains over 12,000 aeronautical books, magazines, pamphlets, and reports gathered from world-wide sources and is one of the most complete aeronautical libraries in the world. Material from this library is not available for loan but may be used for reference purposes.

The Pacific Aeronautical Library

7660 Beverly Boulevard
Los Angeles 36, California

Established in cooperation with the aircraft companies the library serves. The leading aircraft companies in or near Los Angeles participate in its support and operation.

This service library for aeronautical research is available to the public for reading privileges. Source material includes aerodynamic and structural research reports, as well as books on drafting, production methods, history, and allied sciences. It furnishes books, periodicals, and pamphlet material to the participating aircraft companies to supplement their engineering libraries.

Technical Information Service

This service has experienced personnel under the supervision of trained aeronautical engineers to compile any information desired. The services range from listing specialized reference books to the preparation of exhaustive bibliographies, digesting of reports, and general surveys of any aeronautical subject. Some of the available services are:

Bibliographies on any aeronautical subject.
Reports on any aeronautical subject.
Digests of aeronautical books, papers, periodicals, and references.
Translations.
Engineering investigations of special aeronautical subjects.
Biographies of individuals engaged in aeronautics.
Photostats of any aeronautical or general engineering material.
Microfilms made on special order.
Photographs made from the Institute's photographic collection.
Drawings and tracings made.

In addition to the services mentioned any commission which comes within the scope of the Service will be accepted. Special arrangements may be made for work requiring several weeks or months.

Translators are available for accurate transcriptions of all foreign language data. Translations are carefully edited by trained engineers.

Reproductions of any material in the collections of the Institute may be ordered at standard photostat rates.

INSTITUTE OF THE AERONAUTICAL SCIENCES, INC.
2 EAST 64th STREET, NEW YORK 21, N.Y.